DEPARTMENT OF MECHANICAL ENGINEERING

UNIVERSITY COLLEGE LONDON

Pore-scale study on porous media flows with chemical reaction using lattice Boltzmann method

by

Timan Lei

Supervised by

Prof. Kai H. Luo

Prof. Stavroula Balabani

This dissertation is submitted for the degree of

Doctor of Philosophy

University College London, U.K., Thursday 17th June, 2021

Declaration

I, Timan Lei, declare that this dissertation is my own work and has not been submitted for any other degrees or qualifications. The contents are original and contain no outcome of other works, except as specified in the text.

Timan Lei

June 2021

Acknowledgements

Pursuing the PhD degree at UCL Mechanical Engineering has been a challenging experience for me. I think it was my luck to have Prof. Luo as my supervisor. It would not have been possible to make even a small step of progress without his insightful guidance and continuous support. Throughout my doctoral research, more than three years, he has always been available for discussion and advice. His illuminating suggestions and meticulous comments on my work, as well as his motivation and immense knowledge have been of enormous help to me. When I faced difficulties or felt frustrated, Prof. Luo has been an unfailing source of encouragement, assistance, and reassurance. Working with Prof. Luo has been a fabulous and invaluable experience for me and I could not have asked for a better supervisor. I am extremely proud and honoured to be his student. I hope I could pass on all the research values and insights he has given to me.

I would like to extend my gratitude to my parents and sister for their unconditional love and support during my doctoral studies at UCL. I thank all my friends and colleagues who have always been there for me. Finally, I owe thanks to the financial support from the scholarship under the China Scholarship Council (Grant No. 201706160161). This dissertation was also supported by the UK Engineering and Physical Sciences Research Council under the project "UK Consortium on Mesoscale Engineering Sciences (UKCOMES)" (Grant Nos. EP/L00030X/1, EP/R029598/1, EP/S012559/1, and EP/P022243/1).

Abstract

Porous media flows with chemical reaction are common in nature and widely exist in many scientific and industrial applications. However, due to the complexity of coupled mechanisms, numerical modelling and comprehensive understanding of such flows face significant challenges. Therefore, this thesis develops novel lattice Boltzmann (LB) models to undertake pore-scale simulations of porous media flows with chemical reaction. These models, with new reaction source terms and boundary schemes, can describe both homogeneous reaction between two fluids and heterogeneous reaction (dissolution or combustion) at the fluid-solid interface. Unlike previous studies, current models recast heat and mass transfer equations to correctly consider the thermal expansion effects and the conjugate heat transfer and species conservation conditions. Separate LB equations are also developed to include different species properties.

Density fingering with homogeneous reaction is studied at the pore scale. By changing species contributions to density, diffusion coefficients, initial concentrations, and medium heterogeneities, results obtained demonstrate that reaction can enhance, suppress, or trigger fingering. Then, pore-scale simulations of viscous fingering with dissolution reaction are performed. Effects of fluid diffusion, chemical dissolution, and viscosity contrast are extensively assessed. Results illustrate four fingering regimes as stable, unstable, reactive stable, and reactive unstable. Finally, pore-scale coke combustion in porous media is studied. General combustion dynamics are correctly produced, verifying the superior performance of the present LB model over previous ones. A parametric study demonstrates

that the inlet air temperature and the driving force are influential factors and should be constrained within certain ranges for stable combustion fronts.

These pore-scale findings provide valuable insights, like temperature fluctuations at the fluid-solid interface, porous structure evolutions, exact reaction and diffusion rates, and medium heterogeneity effects, which are more precise and explicit than macroscopic results. Furthermore, detailed fingering and combustion dynamics under diverse conditions are helpful in scientific and industrial fields.

Impact Statement

This thesis develops new lattice Boltzmann (LB) models for simulating porous media flows with chemical reaction in Chapter 2. The modelling and simulation communities will benefit from both the LB models proposed and the simulation data obtained. In addition, the present pore-scale simulations are relevant to research communities working on porous media flows, homogeneous and heterogeneous reactions, interface instability, and combustion. Chapters 3-4 investigate dissolution-driven density fingering in porous media at the pore scale. The results obtained capture various fingering dynamics under the effects of homogeneous reaction and differential diffusion. These findings help to reveal fundamental mechanisms behind existing macroscopic data. Chapters 5-6 explore porous media flows with heterogeneous reaction at the fluid-solid interface, including dissolution reaction and coke combustion. Characteristics of such heterogeneous reactions are directly captured: temperature fluctuation at the fluid-solid interface, geometrical evolution, species consumption, and reaction area distribution. Coke combustion dynamics are evaluated under various operation conditions. Moreover, by introducing viscosity contrast, different viscous fingering scenarios caused by dissolution reaction are identified. These pore-scale results provide valuable insights that are more precise and explicit than macroscopic findings.

In the meantime, this research has the potential to benefit the nation from the perspective of energy supply. As the global energy demand increases rapidly, extensive efforts have been devoted to the production of heavy oils. In-situ combustion (ISC) is an efficient but

high-risk technique for heavy oil recovery. To reduce potential safety risks and improve the production efficiency, a stable coke combustion front during the ISC process is necessary and thus calls for a deep understanding of coke combustion. The present pore-scale simulations of coke combustion in porous media contribute to advancing the knowledge base. Furthermore, the assessments of operational conditions and medium structures are helpful in providing designing and optimizing guidance for heavy oil recovery using the ISC process.

Moreover, this thesis contributes to technologies for mitigating the global climate change that is associated with the growing carbon dioxide (CO_2) emission to atmosphere. Recently, limiting the anthropogenic CO_2 emission is gaining considerable interest. A promising solution is to capture CO_2 from power plants and inject it into porous underground reservoirs for long-term sequestration. After injection, the supercritical CO_2 is less viscous and the CO_2-rich brine is denser than the displaced fresh brine, thereby introducing interface instabilities, like density fingering and viscous fingering. Meanwhile, the injected CO_2 acidifies brine and then reacts with chemical solutes in the host brine or dissolves carbonate minerals. Such homogeneous and heterogeneous reactions affect the displacement stability by modifying fluid properties or medium structures. Therefore, a successful CO_2 sequestration process requires pre-estimations of the post-injection displacement between the supercritical CO_2 and the brine in porous reservoirs. To achieve this goal, the present pore-scale study on porous media flows with homogeneous or heterogeneous reaction as well as density or viscosity contrast is thus important.

Table of contents

List of figures

List of tables

CHAPTER 1

Introduction

1.1 Background

With the increase in energy demand all over the world, renewable energy supplies are developing at a fast pace. Due to the low initial base of these supplies however, traditional fossil fuels will remain the leading energy sources for meeting the global energy needs in the coming decades [1]. As one of the typical fossil fuels, oil is forecast to face a certain decrease in demand but continue to hold the highest share in the energy market by 2040 [2]. The World Energy Outlook 2020 also predicts that, without a large shift in policies, it will be too early to foresee a rapid decline in the global oil demand [3]. Based on these predictions, the exploration of oil resources will keep playing a vital role in satisfying the global energy demand. In the past decades, enormous attempts have been made to produce conventional light oils, thereby causing a severe decline in the availability of these oil resources [4]. Fortunately, after the production of light oils, vast heavy or extra-heavy oils are left untapped in reservoirs. Although these heavy oils are hard to produce, they have great potential to facilitate fulfilling the energy demand all over the world [1, 4, 5]. It is thus critical to develop effective and economic techniques to extract heavy oils left behind by light oil recoveries from reservoirs.

To date, extensive efforts have been devoted to the extraction of heavy oils and thus various enhanced oil recovery approaches have been proposed [6, 7]. As an effective

thermal recovery method, the in-situ combustion (ISC) process may achieve recovery factors up to 70% and has received considerable attention [4, 8]. In such a process, solid coke produced by thermal cracking of crude oil is usually covered with solid minerals and serves as the main hydrocarbon fuel. Thus, hot air is injected to react with solid coke at the combustion front in porous oil reservoirs [1, 9]. This heterogeneous reaction releases heat to help increase oil temperature and decrease oil viscosity [10]. Consequently, driven by the propagation of the coke combustion front, heavy oils with improved mobility can be efficiently drained towards production wells [11]. In practical applications however, operation conditions of the ISC process are difficult to control and inappropriate conditions usually introduce unstable combustion fronts and harmful impacts [12]. For example, there are always occasions that the combustion temperature overshoots the maximum value of a given reservoir. The high burning temperature is undesirable as it brings in severe coking, flow passage block, and safety risks [13]. In addition, the injected air sometimes exceeds the required amount and causes oxygen (O_2) breakthrough, which subsequently leads to poor O_2 utilization, low combustion efficiency, and even premature termination of the ISC process [14, 15]. Meanwhile, low temperature and insufficient air injection should be avoided as they introduce undesirable combustion dynamics, like residual coke, incomplete combustion, and slow front propagation [10]. These failures are largely caused by the inadequate understanding of the ISC process [16]. Therefore, to achieve a successful ISC process with a stable combustion front and a high propagation velocity, it is necessary to study coke combustion in porous media and assess the operation conditions.

Together with the continuous use of fossil fuels, the carbon dioxide (CO_2) emission to the atmosphere grows rapidly, which is intimately associated with global climate change

[2]. Thereby, considerable efforts have been directed towards limiting the anthropogenic CO_2 emission. A promising solution is to capture CO_2 from power plants and inject it into geological reservoirs for long-term sequestration [17–20]. After injection, the supercritical CO_2 is less viscous than the displaced host brine and thus fluid mobility decreases in the flow direction, which induces viscous fingering instability at the interface between the two miscible fluids [21]. Meanwhile, the injected CO_2 acidifies the subsurface brine and dissolves carbonate minerals. This mineral dissolution, as a typical form of heterogeneous chemical reaction, consumes CO_2 and modifies local porosity (mobility), thus introducing variations in fingering dynamics [22–24]. On the other hand, the injected CO_2 is less dense than the host brine. So, CO_2 first rises up to spread above the host brine but below the caprock. Then, CO_2 gradually dissolves down into the brine and increases fluid density. This dissolution process finally gives rise to a buoyantly unstable stratification of the denser CO_2-rich brine on top of the less dense host brine, which, in the gravity field, triggers density fingering at the miscible fluid interface [25]. Furthermore, homogeneous chemical reactions frequently occur between dissolved CO_2 and reactants in the host brine, thereby modifying fluid concentration, salinity, and density [26, 27]. As a result, different unstable density distributions and density fingering dynamics can be introduced. These two types of interface instabilities (i.e., viscous fingering and density fingering) accompanied by convection can drive efficient mass transport and thus promote the mixing and trapping of CO_2 in the host brine [28]. Nevertheless, fingering forms channelling of the injected CO_2 fluid and creates potential CO_2 leakage pathways [29, 30]. Due to the mentioned double-edged impacts, understanding the two complex interface instabilities as well as

effects of homogeneous or heterogeneous chemical reactions is thus crucial to achieving a successful CO_2 sequestration process with high efficiency and security [28].

The above introduction indicates the necessity of studying the transport of fluid flows in porous media (porous media flows). Such flows are frequently encountered in natural processes and scientific and industrial applications, ranging from movement of underground water [31–33], geological sequestration of CO_2 [34, 35], enhanced oil recovery [36], to name a few. Thus, a fundamental understanding of the mechanisms behind porous media flows will make contributions to the development of science and technology. However, the dynamics of porous media flows are complex and determined by the coupled unsteady fluid flow, heat and mass transfer, and porous structure. This situation becomes even more complicated with effects of physical (gravity or viscosity contrast) and chemical (homogeneous reaction between fluids, heterogeneous dissolution reaction, and heterogeneous coke combustion) processes. Therefore, this thesis will develop numerical models to simulate porous media flows with chemical reaction. The results obtained are expected to reveal mechanisms behind such complex flows, thereby advancing the knowledge base of scientific fields and providing reliable guidance for engineering applications.

1.2 Scales of porous media flows

For the above porous media flows, solid matrices are fixed and fluids flow through pore spaces. Descriptions of the physical and chemical processes involved are multiscale in nature. As illustrated in Fig. 1.1, porous media flows are usually associated with two length scales: the representative elementary volume (REV) scale and the pore scale [37, 38].

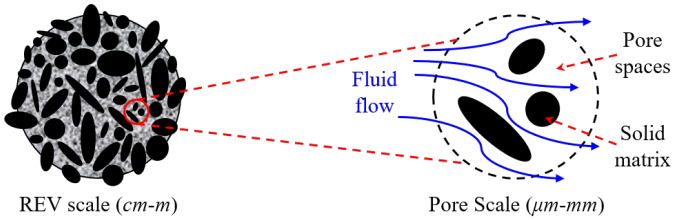

Figure 1.1 Schematics of the porous medium at the REV scale and the pore scale.

At the REV scale, a control volume REV, containing some pores, is selected as the smallest unit of the porous medium [37]. Throughout the REV, the geometric parameters and fluid properties are assumed to be constant. Thereby, the porous medium is treated as a continuum and statistical quantities are defined as the volume-averaged values of the corresponding microscopic parameters over the REV [39]. With such a continuum treatment, fluid flow, heat and mass transfer, and chemical reaction are described by volume-averaged conservation equations [40, 41]. Consequently, chemical reactions are represented by source terms in conservation equations; interactions between the fluid phase and solid matrices are realized by empirical force terms; and geological evolutions are tracked by variations in local porosity [42, 43].

On the other hand, the pore scale is much smaller than the REV sale and thus the above continuum treatment is no longer applicable. At the pore scale, a porous medium is described by discrete elements (e.g., solid matrices and void pores) and fluid mechanisms are tracked in micro pores directly. Fluid motion and mass transport in pore spaces satisfy the Navier-Stokes (NS) equations and the convection-diffusion (CD) equation, respectively; heat transfer in both pore spaces and solid matrices obeys the energy conservation equation; and interactions between the fluid phase and solid matrices are implemented by boundary conditions [37, 44]. In addition, the heterogeneous chemical reaction between the fluid and solid phases is described by reactive boundary conditions at the fluid-solid interface [45–

47], while the homogeneous chemical reaction between two miscible fluids is represented by additional source terms in the CD equation [48, 49]. Thereby, at the pore scale, detailed descriptions of the fluid flow and solute distributions in pores, heat transfer in the whole domain, porous structure evolutions, and chemical reactions can be obtained. These pore-scale details contribute to understanding the physical and chemical mechanisms behind porous media flows and therefore developing macroscopic models [38].

To model REV-scale porous media flows, some numerical solvers have been developed, like the finite-volume method [50, 51], the finite-difference method [52], and the finite-element method [53, 54]. However, due to complex porous structures at the pore scale, these conventional methods cannot easily handle discontinuous variables at the fluid-solid interface, thus limiting their applications in modelling pore-scale porous media flows [45]. Over the past three decades, the lattice Boltzmann (LB) method, based on the kinetic theory, has been developed and become a powerful alternative to conventional numerical solvers for porous media flows. This is attributed to its attractive advantages, like simple implementation, high parallelism, and ability to handle complex physics and boundary conditions [38, 55]. Consequently, LB models have been developed for simulating fluid transport in porous media. At the REV scale, an LB model was proposed for studying incompressible flows in porous media with either constant or variable porosities [56]. Porous media flows with phase change were also studied via a newly built LB model [57, 58]. For this problem, LB models with multiple-relaxation-time (MRT) collision operators were then developed to improve the numerical stability [59–61]. In addition, the LB method has been applied for modelling porous media flows at the pore scale. The media permeability of three-dimensional porous structures were calculated based on

LB simulations [62]. Porous media flows with either heterogeneous dissolution of solid matrices or homogeneous reaction between two miscible fluids have been modelled by LB models [45, 63, 64]. Therefore, as concluded in a review [65], the LB method is one of the most powerful numerical methods for simulating porous media flows.

Obviously, due to different treatments of porous media at the two length scales (pore and REV scales), porous media flows are tracked by separate governing equations. As a result, at the two scales, different numerical approaches are required and different mechanisms are captured. It should be emphasized that, studies at the REV scale are able to enrich the knowledge base of porous media flows. At this scale however, pore-scale details are simplified and ignored; media structures and fluid properties are averaged; and empirical and effective correlations are required [66]. These continuum treatments depend on pore-scale information and will become uncertain without a prior pore-scale knowledge base [10, 67]. In contrast, pore-scale investigations directly describe physical and chemical details of porous media flows in void pores. These pore-scale insights can be upscaled to the REV scale via volume-averaged techniques and then provide useful information for developing REV-scale models. Therefore, this thesis will develop LB models to simulate porous media flows at the pore scale, with effects of both homogeneous and heterogeneous chemical reactions being considered.

1.3 Literature review

The main issues addressed in this thesis are: (1) Dissolution-driven density fingering with homogeneous chemical reaction $A + B \rightarrow C$ in porous media. (2) Miscible viscous fingering with heterogeneous dissolution reaction in porous media. (3) Coke combustion

during the ISC process for heavy oil recovery. Existing investigations on these three types of porous media flows are then reviewed and discussed in the following subsections.

1.3.1 Dissolution-driven density fingering with homogeneous reaction

In a porous medium with a partially miscible top boundary, species A dissolves from above into the host fluid below and no mass transports in the reverse direction. Meanwhile, dissolved A reacts with another reactant B in the host fluid following the $A + B \rightarrow C$ scheme. All the species A, B, and C are in dissolved forms and contribute to changing the fluid density. Thus, with the dissolution of A and the homogeneous reaction $A + B \rightarrow C$, buoyantly unstable stratifications may be introduced to trigger density fingering in the gravity field [28, 68]. Such an interface instability, also known as dissolution-driven density fingering is at the heart of geological CO_2 sequestration and has been receiving increasing attention [34, 69].

Until recently, some experiments have been designed and carried out in small reactors or Hele-Shaw cells to study dissolution-driven density fingering with homogeneous chemical reaction. Budroni *et al.* [70] studied fingering dynamics at the miscible interface between the dissolved ester and alkaline hydroxides. In their experiments, chemical reaction between the two solutions was found to delay the onset and growth of density fingering and even introduce buoyantly stable stratifications. In parallel, experimental efforts were devoted to exploring dynamics of dissolution-driven density fingering at the interface between CO_2 and alkaline solutions. By changing chemical species in alkaline solutions, reaction types and intensities were adjusted and thereby both the well-developed and the suppressed density fingering were captured [71, 72]. Thomas *et al.* [73] and Cherezov *et al.* [74] experimentally demonstrated that reactions between dissolved CO_2 and alkaline

hydroxides accelerated fingering development, with the promotion strength depending on the initial reactant concentrations. Experiments in systems containing either ester-alkaline or CO_2-alkaline solutions were also performed and compared. Observed interface instabilities suggested that, determined by chemical contents, dissolution-driven density fingering was either reinforced or refrained by chemical reaction [75].

The above experimental observations have confirmed that homogeneous reactions between two miscible solutions can modify fluid density and then stabilize or destabilize dissolution-driven density fingering. During these experiments, chemical solutions were transparent, thus requiring pH color indicators to visualize the propagation of density fingering. This treatment, however, may not always capture the whole extent of the fingering development and the convection dynamics [74, 76]. What's more, considering the impact of reaction on fingering dynamics is intimately related to the applied chemical reactants [75], it is thus uneconomic and time-consuming to cover all reaction types and fingering scenarios by merely experiments. For such considerations, researchers conducted theoretical analyses to predict dissolution-driven density fingering with homogeneous reaction $A + B \rightarrow C$ in porous media with partially miscible top boundaries. Kim *et al.* [77–79] applied the linear stability theory to investigate fingering development, showing that reaction could enhance, suppress, and initiate the development of density fingering. A series of theoretical investigations were then carried out to analyze the effects of the homogeneous reaction $A + B \rightarrow C$ on density fingering dynamics [80–82]. These theoretical works predicted eight types of density profiles in the early linear stage of fingering development, with each profile potentially representing a unique type of density fingering scenario.

Theoretical analyses were proven to be capable of predicting more reaction-related density fingering phenomena and thus filling limitations in experimental observations. However, these predictions were based on fingering dynamics in the early linear development stage and completely ignored the non-linear fingering growth during the late period. Moreover, theoretical analyses could not provide development details of density fingering, although they predicted possible fingering types under effects of chemical reaction [28]. For these reasons, numerical simulations have been conducted under the guidance of existing theoretical predictions, to model dissolution-driven density fingering with homogeneous reaction $A + B \rightarrow C$ in porous media. By employing linear analysis results as initial conditions, Kim *et al.* [77, 78] numerically demonstrated different density fingering dynamics. Numerical simulations were then carried out to reproduce the promoting and the suppressing impacts of reaction as well as to test the influence of initial reactant concentrations, which qualitatively verified both experimental observations and theoretical predictions [75]. By adjusting contributions to the fluid density of species A, B, and C, the controlling effects of chemical reaction on density fingering were numerically investigated [83]. In the meantime, Loodts *et al.* [28] numerically showed that the reaction $A + B \rightarrow C$ could accelerate, inhibit, or introduce the development of density fingering, which matched well with their theoretical predictions [81]. Through their simulations, spatial and temporal fingering dynamics were illustrated and differences between numerical and theoretical results were pointed out, especially when fingering developed into the non-linear late stage.

Seen from the above experimental, theoretical, and numerical results, homogeneous reaction is able to change fluid density and thus stabilize, destabilize, and trigger the development of density fingering in porous media. These findings are helpful for understanding

density fingering dynamics in the context of chemical reaction. Nevertheless, they all assumed that the chemical species A, B, and C diffused equally. It has been reported that, in order to correctly interpret experimental observations, effects of different diffusion coefficients among the three chemical solutes should be included [71, 73]. Furthermore, during the geological sequestration of CO_2, chemical species are likely to diffuse at different rates in the host brine [84]. It is thus necessary to consider a more general case with three chemical species diffusing at different coefficients.

Two types of density fingering introduced by differential diffusion have been reported under non-reactive conditions [85, 86]. On one hand, when a less dense fluid containing a slow diffusing solute overlies a denser host fluid with a fast diffusing solute, a species accumulation zone is formed in the top layer while a depletion area is generated below. This is known as the double-diffusive (DD) mechanism. The accumulation and depletion areas constitute a locally unstable stratification and gives rise to the development of density fingering. On the other hand, the diffusive-layer convection (DLC) mechanism appears in the reverse situation, with the solute in the top layer diffusing faster than the one in the host fluid below. This situation brings in an accumulation zone locating below a depletion region. The accumulation zone forms an unstable stratification with the host fluid below, hence triggering the appearance of density fingering.

Until now, existing but limited studies have been conducted to investigate the effects of these two differential diffusion mechanisms (DD and DLC) on the development of density fingering in porous media, with the homogeneous reaction $A + B \rightarrow C$ being considered. For example, Trevelyan *et al.* [87] theoretically predicted, for a miscible interface between two reactive solutions, that the inclusion of differential diffusion yielded up to sixty-two

types of density profiles. Similarly, by changing density contributions and diffusion rates of the three chemical solutes, Loodts *et al.* [82] theoretically identified eight different density profiles in a porous medium with a partially miscible top boundary. Apart from these theoretical works, numerical simulations were performed to study density fingering with effects of differential diffusion. Based on the assumption that the dissolution of A from the top boundary could increase the host fluid density, four types of fingering scenarios were identified and the early-stage density profiles showed similar tendencies as theoretical predictions [84, 88]. To explain experimental observations, density fingering evolutions were modelled in cases with different diffusion rates, concentrations, and density contributions of the three chemical solutes [89, 90]. Numerical results verified the DD mechanism was able to accelerate, inhibit, and induce the development of density fingering.

On the basis of existing works, numerical simulation was proven to be a powerful approach for studying dissolution-driven density fingering with homogeneous reaction $A + B \rightarrow C$ in porous media at the pore scale. Numerical findings have improved the knowledge base of such a problem and thus are important to both scientific areas and industrial applications (like the geological sequestration of CO_2). However, some limitations in previous simulations should be noted. First, the medium heterogeneity is not considered. In non-reactive situations, the permeability anisotropy could obviously influence fingering dynamics [91], which should be extended to reactive cases. Second, pore-scale simulations are still missing. Owing to the complex porous structures, previous numerical studies were mainly conducted at the REV scale, where continuum assumptions were applied and volume-averaged uncertainties were introduced [38]. Third, effects of differential diffusion on density fingering are not comprehensively explored. Although theoretical

analyses have predicted eight potential fingering scenarios [82], existing simulations were performed under the assumption that fluid density increased with the dissolution of A, leaving the situations with species A decreasing fluid density unexplored [84]. Therefore, dissolution-driven density fingering with homogeneous reaction $A + B \rightarrow C$ in porous media needs further investigations at the pore scale, in which effects of reaction, medium heterogeneity, and differential diffusion should be discussed.

1.3.2 Miscible viscous fingering with heterogeneous dissolution reaction

In geological sequestration of CO_2, viscous fingering phenomena usually occur as the less viscous CO_2 is injected to displace the more viscous host brine in porous storage sites. It indicates that a successful CO_2 sequestration process requires pre-estimations of the displacement stability between the miscible CO_2 and brine. Note that, dissolved CO_2 can acidify brine and dissolve solid minerals, which subsequently affects viscous fingering dynamics. Therefore, a better understanding of miscible viscous fingering with heterogeneous dissolution reaction in porous media is of great importance [26, 92].

Viscous fingering arises when a high-mobility fluid displaces a low-mobility one, forming the finger-shaped penetration of the displacing fluid into the displaced one [93]. This unstable displacement pattern has been extensively analyzed in the existing literature. One of the pioneering works was conducted by Saffman and Taylor, who identified fingering phenomena in immiscible displacement [94]. Researchers subsequently extended these ideas to study miscible viscous fingering and summarize different stages in the full life cycle of viscous fingering (i.e., fingering initiation, growth, interaction, and decay) [29, 95]. To be connected with industrial applications, viscous fingering dynamics were investigated in the presence of a magnetic field [96] and nanoparticles [97]. Effects of

medium heterogeneity were studied and showed intensified fingering in high-permeability porous layers [98–100]. In addition to these non-reactive studies, efforts were devoted to modelling fingering dynamics in miscible displacement between two reactive fluids. Chemical reactions were numerically shown to cause viscous fingering and new fingering phenomena (i.e., droplet and tip splitting) [49, 101]. Fingering behaviors were also investigated with adsorption reaction on porous matrices, suggesting adsorption could be a useful strategy to manipulate viscous fingering [102, 103]. Recent attentions were turned to classifying different fingering patterns in parameter spaces, which were determined by relative strengths of convection, diffusion, and chemical reaction [104, 105]. These classifications could play guiding roles in practical applications as they revealed possible measures for controlling viscous fingering, like choosing suitable reactants [104].

In the above studies, the fluid mobility contrast, acting as the determination of viscous fingering, comes from differences between fluid viscosities. On the other hand, the mobility gradient can develop in porous media as dissolution reaction occurs on porous matrices. Explicitly, the reaction consumes chemical solutes in the displacing fluid and dissolves solid matrices, which ultimately increases porosity (or fluid mobility) behind the moving fluid interface [22]. Such mineral dissolutions make a fluid in a high-mobility area displace another fluid in a low-mobility zone, thereby triggering fingering phenomena (also known as infiltration instability) [92, 106]. This has long been observed in acid dissolution experiments. Fredd and Fogler were one of the first to experimentally identify different fingering channels under various injection and dissolution rates [107]. They suggested the existence of optimal conditions that produced channels with the minimum pore volumes for fluid to break through. The development of fingering induced by chemical

dissolutions was then observed to be enhanced by the medium heterogeneity and the brine PH [108]. In parallel, numerical models were developed to simulate dissolution reaction in porous media. With these simulations, key factors influencing the fingering dynamics were evaluated [109]; parameter diagrams for classifying fingering patterns were created [110]; and experimental observations were validated and explained [111].

These existing studies have enriched the knowledge of miscible fingering instability induced by viscosity contrast or dissolution reaction in porous media. However, they were carried out at macroscopic scales, thus obtaining effective transport and reactive parameters via empirical correlations or volume-averaged techniques. In this way, uncertainties would be introduced if without pore-scale information [10]. Moreover, for a porous medium, the determination of its permeability is complex and not a simple function of porosity [112]. For these reasons, pore-scale simulations of miscible displacement were performed. A random network model was proposed to describe the formation of fingering with chemical dissolution in porous media [113]. The finite difference and the random walks methods were combined to model reactive transport with solid structure evolutions at the pore scale. Results identified different dissolution instabilities based on the relative magnitudes of convection, diffusion, and dissolution [114, 115]. Nevertheless, these conventional methods cannot easily handle porous media with complicated or variable structures under dissolution reactions [45].

Over the past three decades, LB models have been developed for simulating either viscous fingering or dissolution reaction in porous media at the pore scale. On one hand, Liu *et al.* [66] developed an LB model to quantify fluid mixing in both homogeneous and heterogeneous porous media, showing that viscous fingering introduced velocity disorders

and enhanced fluid mixing. Such promoting effects of viscous fingering were proved to be suppressed by chemical reactions that could sharpen fingering interfaces [48]. For miscible viscous fingering, temperature variations and nanoparticles were found to play imperative roles as they modified fluid viscosity [116]. On the other hand, Kang *et al.* [45] proposed a pore-scale LB model to study dissolution reactions, with porous structure evolutions being tracked by the volume of pixel scheme. Their results qualitatively verified experimental results in [107] and suggested the reliability of the LB method for modelling chemical dissolution in porous media at the pore scale. After this first step, they further predicted different dissolution patterns and porosity-permeability relationships under varying flow and dissolution conditions [117]. They also extended to model multi-component systems that were associated with geological CO_2 sequestration [46, 118]. Pore-scale LB models were recently applied to investigate dissolution reactions in porous media coupled with precipitation reaction [112] or binary minerals [119].

The above studies have provided detailed insights into fingering dynamics introduced by viscosity contrast or dissolution reaction in porous media. Nevertheless, no pore-scale study has been devoted to investigating fingering dynamics considering the coexistence of viscosity contrast and chemical dissolution. In applications like long-term CO_2 sequestration, these two factors usually take place simultaneously and have significant effects on the viscous fingering instability. Although existing simulations have modelled fingering with both viscosity contrast and adsorption reaction, they applied REV-scale assumptions and ignored the dissolution of solid matrices [102, 103]. It is hence necessary to perform pore-scale simulations of miscible displacement in porous media, focusing on viscous fingering dynamics in the presence of both viscosity contrast and dissolution reaction.

1.3.3 Coke combustion during the ISC process for heavy oil recovery

In-situ combustion (ISC) for heavy oil recovery is a high-risk process and thus calls for a deep understanding of the coke combustion front. The solid coke combustion during the ISC process, as a typical type of heterogeneous chemical reaction, involves unsteady fluid flow, combustion kinetics, reactive air-coke interface, and conjugate heat transfer (i.e., the continuity of both temperature and normal heat flux) between the air and the solid phases. Simultaneously, fluid density varies with local temperature and porous structure evolves as coke burns out. To investigate such a complex process, experiments are difficult to conduct and numerical simulations turn out to be effective approaches.

An upscaling method was proposed to study coke combustion in porous media at the field scale. Modelled results indicated that heat conduction was able to stabilize the coke combustion front [120]. Through numerical simulations, it was suggested that coke combustion could be simplified as a one-step reaction using the $C + O_2 \rightarrow CO_2$ scheme [121]. Influencing factors on coke combustion were numerically investigated [122, 123]. Findings obtained emphasized positive effects of the vapor-liquid equilibrium phase behavior on coke combustion rates [122]. To improve the oil production efficiency, they also suggested the beneficial role of increasing air injection rate, medium permeability, and O_2 content [123]. Even though these simulations have advanced the understanding of coke combustion in porous media, they were carried out at macroscopic scales. Consequently, in these numerical studies, volume-averaged techniques, effective parameters, and empirical correlations were applied. The accuracy of these continuum treatments requires pore-scale details [10, 67]. Thus, models to simulate coke combustion and provide pore-scale information are desirable.

As a powerful solver for porous media flows, LB models have been proposed to simulate the physical and chemical processes involved in coke combustion at the pore scale. First, for resolving the reactive fluid-solid interface, a new LB model was reported and the nonequilibrium concentration distribution functions at the interface were determined by the dot product of velocity and concentration gradient [45, 47]. A general bounce-back scheme was then developed to implement reactive boundary conditions at both stable and moving solid-fluid interfaces [124]. The interface concentration gradient in this scheme was further modified to be calculated by moments of nonequilibrium distribution functions [125]. Besides these reactive boundary schemes, the LB method was proven to be capable of capturing conjugate heat transfer between two phases, without involving conventional extrapolations or iterations [37]. Wang *et al.* [126, 127] proposed a half-lattice division scheme for matching solid-fluid conjugate heat transfer conditions automatically. Nevertheless, this method was limited to cases in steady states or with unified heat capacitance across phases. An additional source term was therefore introduced into the LB equations to model general conjugate heat transfer conditions [128]. This conjugate treatment was employed to investigate methane hydrate dissolution as well [129].

Regarding applications of the LB method in the combustion field, several attempts have been made over the past two decades. Yamamoto *et al.* [130, 131] were one of the first to apply an LB model to study combustion and catalytic reaction in porous structures. More recently, an LB model was employed for char-pellet combustion, incorporating the sodium release and ash inhibition effects on O_2 diffusion [132]. However, thermal expansion effects have not been included in these studies, mainly due to the weak compressibility of the classical iso-thermal LB models used by them. To solve this issue, Lin and Luo

[133, 134] developed discrete Boltzmann models for fully coupled flow and combustion simulations with density variation. They successfully applied these models to both subsonic and supersonic combustion, as well as premixed, nonpremixed, and partially premixed nonequilibrium multicomponent reactive flows. Another LB model was established based on the low Mach number approximation, to investigate low-speed reactive flows with significant density changes caused by the reaction heat release [135, 136]. Inspired by such a simplified approach, further works have been conducted to correctly account for thermal compressibility in LB simulations, by modifying equilibrium density distribution functions based on a thermal Hermite expansion [137, 138], or combining a low Mach number approximation and finite different schemes [139, 140].

On the basis of these existing investigations, Xu *et al.* [10] built a single-relaxation-time (SRT) LB model for coke combustion in porous media at the pore scale. They considered the fluid flow, heat and mass transfer, surface reaction, and geometrical evolution simultaneously. Their pore-scale simulations successfully distinguished different mechanisms for coke combustion, but nevertheless contained four limitations. First, a constant fluid density is used, without including thermal expansion effects. Second, the reactive coke-fluid interface is resolved by an iterative scheme, which is hard to implement and computationally demanding. Then, the use of SRT LB models in porous media may introduce inaccurate boundary conditions and the viscosity-dependent permeability, which has been widely pointed out [62]. Finally, effects of porous structure (e.g., porosity, random coke distribution, matrix structure, etc.) on coke combustion are not explored, but these factors vary obviously among different underground sites. To overcome these shortcomings, a new LB model is required for simulating coke combustion in porous media at the pore scale.

Two critical perspectives need to be realized by this new LB model: including thermal expansion effects; implementing conjugate heat transfer and species conservation at the coke-fluid interface without iterative calculations.

1.4 Main research tasks

In accordance with the aforementioned literature review, the main research tasks of this thesis are listed from the following three aspects.

(1) To provide new insights into the dissolution-driven density fingering with homogeneous reaction $A + B \rightarrow C$ in porous media at the pore scale, the following tasks are expected to be fulfilled:

- Developing an MRT LB model to simulate dissolution-driven density fingering with reaction $A + B \rightarrow C$ in porous media at the pore scale. Constructing different homogeneous and heterogeneous media.
- Classifying fingering phenomena into different groups based on contributions to fluid density and diffusion coefficients of three chemical solutes.
- Quantifying fingering characteristics, including distributions of species concentration and fluid density, fingering extension depth, reaction rate, and storage of species A in the host fluid.
- Analysing effects of the medium heterogeneity, chemical reaction, and differential diffusion on density fingering dynamics.
- Investigating fingering scenarios, fingering properties, and storage behaviors of species A, under two types of differential diffusion effects.

(2) To advance the knowledge base of miscible viscous fingering with heterogeneous dissolution reaction in porous media at the pore scale, the following goals are forecast to be achieved:

- Proposing another MRT LB model for pore-scale studies of miscible viscous fingering in porous media. Developing a boundary scheme for solving dissolution reaction at the fluid-solid interface.
- Identifying different viscous fingering dynamics by changing relative strengths of dissolution reaction, fluid diffusion, and viscosity contrast.
- Quantifying viscous fingering properties, like fingering length, dissolution rate, and displacing efficiency, under different parameters.
- For every fixed dissolution rate in a certain range, summarizing stable and unstable cases in a phase plane spanned by viscosity ratio and Peclet number.

(3) To obtain an improved understanding of solid coke combustion in porous media at the pore scale, the tasks are planned as follows:

- Building a third MRT LB model for pore-scale simulations of coke combustion, in which thermal expansion effects are included and the reactive air-coke interface is implemented without iterative calculations.
- Comparing with existing LB models for coke combustion to demonstrate advantages of the proposed new LB model.
- Investigating the general coke combustion dynamics in a homogeneous porous medium, with heat and mass transfer, combustion front properties, and porous medium structure evolution being clarified at the pore scale.

– Quantifying coke combustion characteristics under different operation conditions, like inlet air temperature, driving force, and porous structure.

CHAPTER 2

Lattice Boltzmann method for porous media flows with chemical reaction

The LB method, as a mesoscopic approach, is developed on the basis of the lattice gas automata model [38, 141]. In this method, LB equations are built to describe evolutions of particle distribution functions, the statistical behaviors of which are then defined to describe the macroscopic fluid properties. The LB equation has been verified to be a discrete scheme of the Boltzmann equation with discrete velocities [142, 143]. Using the Chapman-Enskog expansion analysis, macroscopic equations can be correctly derived from LB equations with appropriately defined collision operators [38, 144]. The standard LB equation uses the Bhatnagar-Gross-Krook collision operator (or the SRT collision operator) [145]. This simplicity makes the SRT LB model be frequently applied and developed for simulating fluid dynamics. Nevertheless, some investigations demonstrate SRT LB models usually suffer from numerical instability and low calculation accuracy, especially for fluid flows in porous media [146, 147]. To solve this limitation, another popular LB model with an MRT collision operator is proposed [147–149]. This model has been proven to be superior to the SRT LB model from two perspectives [147]. First, collision operators can be adjusted individually to achieve a numerically stable state. Second, for pore-scale simulations of porous media flows, MRT LB models can correctly capture the no-slip velocity condition at the fluid-solid boundary and thus avoid the unphysical dependence of permeability on viscosity. Therefore, this thesis will develop MRT LB models for simulating porous media flows with chemical reaction at the pore scale.

Considering this thesis focuses on reactive fluid flows in two-dimensional (2D) porous media, the most popular two-dimensional nine-velocity (D2Q9) scheme is applied and D2Q9 MRT LB models are developed. The corresponding discrete velocities $\boldsymbol{e}_i$ and weight coefficients w_i are defined as [38],

$$\begin{cases} \boldsymbol{e}_i = e\,(0,\ 0)\,, & w_i = \frac{4}{9}, \qquad i = 0, \\ \boldsymbol{e}_i = e\left(\cos\frac{(i-1)\pi}{2},\ \sin\frac{(i-1)\pi}{2}\right), & w_i = \frac{1}{9}, \qquad i = 1-4, \\ \boldsymbol{e}_i = \sqrt{2}e\left(\cos\frac{(2i-1)\pi}{4},\ \sin\frac{(2i-1)\pi}{4}\right), & w_i = \frac{1}{36}, \qquad i = 5-8. \end{cases} \tag{2.1}$$

Here $e = \delta_x/\delta_t$ is the lattice speed, with δ_x and δ_t denoting the lattice spacing and the time step, respectively. In addition, the transformation matrix $\boldsymbol{M}$ corresponding to the D2Q9 scheme is set as [38],

$$\boldsymbol{M} = \begin{pmatrix} 1 & 1 & 1 & 1 & 1 & 1 & 1 & 1 & 1 \\ -4 & -1 & -1 & -1 & -1 & 2 & 2 & 2 & 2 \\ 4 & -2 & -2 & -2 & -2 & 1 & 1 & 1 & 1 \\ 0 & 1 & 0 & -1 & 0 & 1 & -1 & -1 & 1 \\ 0 & -2 & 0 & 2 & 0 & 1 & -1 & -1 & 1 \\ 0 & 0 & 1 & 0 & -1 & 1 & 1 & -1 & -1 \\ 0 & 0 & -2 & 0 & 2 & 1 & 1 & -1 & -1 \\ 0 & 1 & -1 & 1 & -1 & 0 & 0 & 0 & 0 \\ 0 & 0 & 0 & 0 & 0 & 1 & -1 & 1 & -1 \end{pmatrix}. \tag{2.2}$$

This matrix maps the distribution functions from the physical space $\boldsymbol{\psi} = (\psi_0,\ \psi_1,\ \psi_2,\ ...,\ \psi_8)^{\mathrm{T}}$ into the moment space as [38],

$$\hat{\boldsymbol{\psi}} = \boldsymbol{M} \cdot \boldsymbol{\psi}. \tag{2.3}$$

Note that, for all the proposed D2Q9 MRT LB models in this thesis, these three equations (2.1)-(2.3) are applicable and the parameter e is given as the velocity unit, i.e., $e = 1$.

2.1 MRT LB model for flows with homogeneous reaction

The dissolution-driven density fingering between two reactive solutions (labeled as 1 and 2) is considered in porous media at the pore scale. In such porous media flows, species A from fluid 1 dissolves into the host fluid 2 and reacts with another solute B following the $A+B \rightarrow C$ scheme. The product C of this homogeneous reaction is in the dissolved form. Thus, the fluid motion and species concentration evolutions in pore spaces are described by the incompressible NS equations and the convection-diffusion-reaction (CDR) equations,

$$\nabla \cdot \boldsymbol{u} = 0, \tag{2.4}$$

$$\rho_0 \left(\partial_t \boldsymbol{u} + \boldsymbol{u} \cdot \nabla \boldsymbol{u}\right) = -\nabla p + \nabla \cdot \left(\nu \rho_0 \nabla \boldsymbol{u}\right) + \boldsymbol{F}, \tag{2.5}$$

$$\partial_t C_A + \boldsymbol{u} \cdot \nabla C_A = D_A \nabla^2 C_A - F_{ro}, \tag{2.6}$$

$$\partial_t C_B + \boldsymbol{u} \cdot \nabla C_B = D_B \nabla^2 C_B - F_{ro}, \tag{2.7}$$

$$\partial_t C_C + \boldsymbol{u} \cdot \nabla C_C = D_C \nabla^2 C_C + F_{ro}, \tag{2.8}$$

where $\boldsymbol{u} = (u,\ v)$, ρ_0, p, and ν are the fluid velocity, density, pressure, and kinematic viscosity respectively. t is the time, F_{ro} is the reaction rate of the homogeneous reaction $A+B \rightarrow C$, and $\boldsymbol{F} = (F_x,\ F_y)$ is the body force term. C_r and D_r are the concentration and diffusion coefficient of species r ($r = A,\ B,\ C$), respectively.

2.1.1 Model development

To solve the above governing equations (2.4)-(2.8), an MRT LB model is developed. The present model consists of four sets of LB equations, with one for the NS equations (2.4)-(2.5) and three for the CDR equations (2.6)-(2.8). Since LB equations for concentration evolutions of species A, B, and C are of the same pattern, only those for species A are

introduced. The evolution equations of the MRT LB model are [38],

$$\begin{aligned} f_i(\boldsymbol{x}+\boldsymbol{e}_i\delta_t,\, t+\delta_t) - f_i(\boldsymbol{x},\, t) = &-\left(\boldsymbol{M}^{-1}\boldsymbol{S}\boldsymbol{M}\right)_{ij}\left[f_j(\boldsymbol{x},\, t) - f_j^{eq}(\boldsymbol{x},\, t)\right] \\ &+ \delta_t\left(\boldsymbol{M}^{-1}(\boldsymbol{I}-0.5\boldsymbol{S})\boldsymbol{M}\right)_{ij}\overline{F}_j, \end{aligned} \tag{2.9}$$

$$\begin{aligned} g_{A,i}(\boldsymbol{x}+\boldsymbol{e}_i\delta_t,\, t+\delta_t) - g_{A,i}(\boldsymbol{x},\, t) = &-\left(\boldsymbol{M}^{-1}\boldsymbol{S}_A\boldsymbol{M}\right)_{ij}\left[g_{A,j}(\boldsymbol{x},\, t) - g_{A,j}^{eq}(\boldsymbol{x},\, t)\right] \\ &+ \delta_t\overline{F}_{A,i} + 0.5\delta_t^2\partial_t\overline{F}_{A,i}, \end{aligned} \tag{2.10}$$

for $i,\ j = 0,\ 1,\ ...,\ 8$, where $f_i(\boldsymbol{x},\ t)$ and $g_{A,i}(\boldsymbol{x},t)$ are distribution functions for the hydrodynamics and the concentration of A, respectively. To recover the incompressible NS equations correctly, the equilibrium distribution functions f_i^{eq} and $g_{A,i}^{eq}$ are given as [38],

$$f^{eq} = w_i\left[\rho_p + \rho_0\left(\frac{\boldsymbol{e}_i\cdot\boldsymbol{u}}{c_s^2} + \frac{(\boldsymbol{e}_i\cdot\boldsymbol{u})^2}{2c_s^4} - \frac{\boldsymbol{u}^2}{2c_s^2}\right)\right], \tag{2.11}$$

$$g_{A,i}^{eq} = w_i C_A\left[1 + \frac{\boldsymbol{e}_i\cdot\boldsymbol{u}}{c_s^2} + \frac{(\boldsymbol{e}_i\cdot\boldsymbol{u})^2}{2c_s^4} - \frac{\boldsymbol{u}^2}{2c_s^2}\right]. \tag{2.12}$$

Here ρ_p is a variable related to the fluid pressure as, $p = c_s^2\rho_p$, with $c_s = e/\sqrt{3}$ being the lattice sound velocity. To avoid discrete lattice effects in the LB model, distribution functions for the force term and the reaction source term are [38, 48, 150],

$$\overline{F}_i = w_i\left[\frac{\boldsymbol{e}_i\cdot\boldsymbol{F}}{c_s^2} + \frac{(\boldsymbol{e}_i\cdot\boldsymbol{u})(\boldsymbol{e}_i\cdot\boldsymbol{F})}{c_s^4} - \frac{\boldsymbol{u}\cdot\boldsymbol{F}}{c_s^2}\right], \tag{2.13}$$

$$\overline{F}_{A,i} = w_i(-F_{ro})\left(1 + \frac{\boldsymbol{e}_i\cdot\boldsymbol{u}}{c_s^2}\frac{\tau_A - 0.5}{\tau_A}\right). \tag{2.14}$$

The time derivative of $\overline{F}_{A,i}$ in Eq. (2.10) is treated by the backward-difference scheme [37],

$$\frac{\partial\overline{F}_{A,i}}{\partial t} = \frac{\overline{F}_{A,i}(\boldsymbol{x},\, t) - \overline{F}_{A,i}(\boldsymbol{x},\, t-\delta_t)}{\delta_t}. \tag{2.15}$$

Based on the transformation in Eq.(2.3), evolution equations (2.9)-(2.10) are implemented in the moment space as,

$$\hat{\boldsymbol{f}}(\boldsymbol{x}+\boldsymbol{e}_i\delta_t,\, t+\delta_t) = \hat{\boldsymbol{f}}(\boldsymbol{x},\, t) - \boldsymbol{S}\left[\hat{\boldsymbol{f}}(\boldsymbol{x},\, t) - \hat{\boldsymbol{f}}^{eq}(\boldsymbol{x},\, t)\right] + \delta_t(\boldsymbol{I}-0.5\boldsymbol{S})\hat{\boldsymbol{F}}, \tag{2.16}$$

$$\hat{\boldsymbol{g}}_A\left(\boldsymbol{x}+\boldsymbol{e}_i\delta_t,\, t+\delta_t\right)=\hat{\boldsymbol{g}}_A\left(\boldsymbol{x},\, t\right)-\boldsymbol{S}_A\left[\hat{\boldsymbol{g}}_A\left(\boldsymbol{x},\, t\right)-\hat{\boldsymbol{g}}_A^{eq}\left(\boldsymbol{x},\, t\right)\right]+\delta_t\hat{\boldsymbol{F}}_A+0.5\delta_t^2\partial_t\hat{\boldsymbol{F}}_A, \quad (2.17)$$

where $\boldsymbol{S}$ and $\boldsymbol{S}_A$ are diagonal relaxation matrices of relaxation rates s_i and $s_{A,i}$ in the moment space, respectively. In the following simulations, the relaxation rates are chosen as used in Refs. [62, 151]. The equilibrium moments $\hat{\boldsymbol{f}}^{eq}$ and $\hat{\boldsymbol{g}}_A^{eq}$ are defined by,

$$\hat{\boldsymbol{f}}^{eq}=\left(\rho_p,\, -2\rho_p+3\rho_0\boldsymbol{u}^2,\, \rho_p-3\rho_0\boldsymbol{u}^2,\, \rho_0 u,\, -\rho_0 u,\, \rho_0 v,\, -\rho_0 v,\, \rho_0\left(u^2-v^2\right),\, \rho_0 uv\right), \quad (2.18)$$

$$\hat{\boldsymbol{g}}_A^{eq}=C_A\left(1,\, -2+3\boldsymbol{u}^2,\, 1-3\boldsymbol{u}^2,\, u,\, -u,\, v,\, -v,\, u^2-v^2,\, uv\right), \quad (2.19)$$

and moments of the force term and the reaction source term are expressed as,

$$\hat{\boldsymbol{F}}=\left(0,\, 6\boldsymbol{u}\cdot\boldsymbol{F},\, -6\boldsymbol{u}\cdot\boldsymbol{F},\, F_x,\, -F_x,\, F_y,\, -F_y,\, 2\left(uF_x-vF_y\right),\, uF_y+vF_x\right), \quad (2.20)$$

$$\hat{\boldsymbol{F}}_A=\left(-F_{ro}\right)\left(1,-2,1,\left(1-0.5s_{A,3}\right)u,-\left(1-0.5s_{A,4}\right)u,\left(1-0.5s_{A,5}\right)v,-\left(1-0.5s_{A,6}\right)v,0,0\right). \quad (2.21)$$

Finally, the macroscopic variables are obtained from the distribution functions as,

$$\rho_p=\sum_i f_i,\quad \rho_0\boldsymbol{u}=\sum_i \boldsymbol{e}_i f_i+0.5\delta_t\boldsymbol{F},\quad C_A=\sum_i g_{A,i}. \quad (2.22)$$

Through the Chapman-Enskog analysis on the present LB equations, the governing equations (2.4)-(2.8) can be recovered with the relaxation times τ and τ_A being,

$$\nu=c_s^2\left(\tau-\frac{1}{2}\right)\delta_t,\qquad D_A=c_s^2\left(\tau_A-\frac{1}{2}\right)\delta_t. \quad (2.23)$$

Note that, the proposed model in this section includes separate LB equations for solving species evolutions. Thus, it is capable of considering species with different properties, like initial concentration, diffusion rate, and contribution to fluid density.

2.1.2 Model validation

To demonstrate the reliability of the present MRT LB model for simulating porous media flows with homogeneous reaction and density instability, validation simulations are carried out in this subsection. Two widely-accepted benchmark problems are adopted: the miscible density fingering in a single pore and the unsteady advection-diffusion-reaction problem.

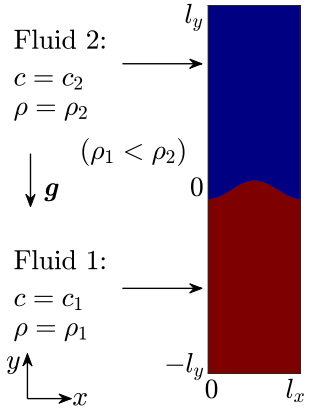

Figure 2.1 Validation test of density fingering in a single pore: Computational domain and initial conditions.

The proposed MRT LB model is firstly validated by simulating the development of density fingering at the interface between two miscible fluids in a single pore. As sketched in Fig. 2.1, the computational domain is $0 \leq x \leq l_x = 1$ and $-l_y \leq y \leq l_y = 2$. Initially, a dense fluid 2 at concentration $c = c_2 = 0$ and density $\rho = \rho_2$ occupies the region $0 \leq y \leq l_y$, and another less dense fluid 1 at concentration $c = c_1 = 1$ and density $\rho = \rho_1$ fills in the rest domain. These two fluids are assumed to be isothermal, incompressible, and non-reactive. The initial interface between the two fluids at $y = 0$ is perturbed by,

$$y = -0.1 l_y \cos\left(2\pi x / l_x\right). \tag{2.24}$$

For this problem with a dense fluid overlying a less dense one in the gravity field, density fingering will appear and grow towards top and bottom boundaries as time goes on.

For the purpose of comparison, simulation parameters are set as used in [152]. That is, by selecting the characteristic length $L = l_x$ and velocity $U = \sqrt{g\beta c_1 L}$, the Schmidt number is $\mathrm{Sc} = \nu/D = 1.0$ and the Rayleigh number is $\mathrm{Ra} = g\beta c_1 L^3/\nu^2 D = 10^6$. As for boundary treatments, the no-slip velocity and impermeable concentration boundary conditions at the top ($y = l_y$) and bottom ($y = -l_y$) walls are realized by the halfway bounce-back scheme. Periodic conditions are implemented on the two lateral sides. A mesh of size $N_x \times N_y = 256 \times 1024$ is used after grid independence tests.

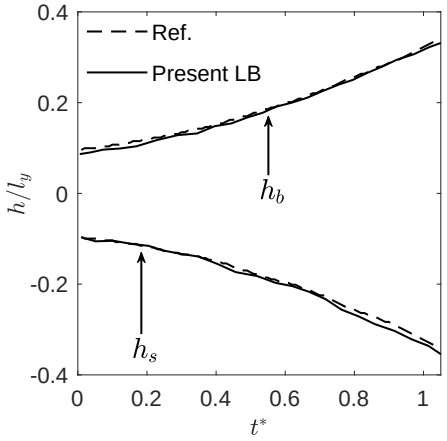

Figure 2.2 Validation test of density fingering in a single pore: Comparison of the penetration lengths of the spike (h_s) and the bubble (h_b) in the case with $\mathrm{Sc} = 1$ and $\mathrm{Ra} = 10^6$ between the present LB simulation results and those in the reference work.

To quantify the growth of density fingering, horizontally averaged concentration profiles $\overline{c}$ are calculated. Then, the penetration lengths of the spike (h_s) and the bubble (h_b) of density fingering are defined as the positions with $\overline{c} = 0.95$ and $\overline{c} = 0.05$, respectively. Figure 2.2 shows the comparison of the measured penetration lengths h_s and h_b. It is observed that our simulation results agree well with those widely-tested results in [152], indicating the reliability of our developed LB model in simulating density instability between two miscible fluids at the pore scale.

After that, an unsteady advection-diffusion-reaction problem in a square domain is modelled to test the present MRT LB model. The problem is described as [153],

$$\frac{\partial c}{\partial t} + \boldsymbol{u}\cdot\nabla c = D\nabla^2 c + \exp\left(\left(1-2\pi^2 D\right)t\right)\left(\pi(u+v)\cos(x+y)+\sin(x+y)\right), \quad \text{with} \quad \boldsymbol{x} = (x,\, y) \in [0,\, l_x]\times[0,\, l_y]. \tag{2.25}$$

By setting a constant velocity $\boldsymbol{u}$, the analytical solution of concentration c_a is obtained as,

$$c_a(x,\, y,\, t) = \exp\left(\left(1-2\pi^2 D\right)t\right)\sin(x+y). \tag{2.26}$$

In our simulations, the initial and boundary conditions are given by using the analytical solution in Eq. (2.26), which are realized by the non-equilibrium extrapolation scheme [154]. The lattice size is set as $N_x \times N_y = 256 \times 256$ after grid-independence tests. The characteristic parameters are selected as $L = l_y = 256$ and $U = u$, respectively. Table 2.1 shows the global relative errors E under different test conditions, where E is calculated as,

$$E = \frac{\sum|c - c_a|}{\sum|c_a|}. \tag{2.27}$$

Good agreements between the present simulation results and the data in the reference work [153] can be observed again.

Table 2.1 Validation test of an unsteady advection-diffusion-reaction problem: Comparison of the global relative error between the present LB simulation results and those in the reference work.

Parameters	Our results	Ref. [153]
$u = v = 0.01,\ D = 0.01,\ t^* = 0.005$	5.5785×10^{-5}	5.0705×10^{-5}
$u = v = 0.01,\ D = 10^{-3},\ t^* = 0.005$	1.0823×10^{-4}	9.9164×10^{-5}
$u = v = 0.10,\ D = 0.01,\ t^* = 0.05$	5.6398×10^{-5}	6.1848×10^{-5}
$u = v = 0.10,\ D = 10^{-3},\ t^* = 0.05$	1.2896×10^{-4}	1.0873×10^{-4}

The above validation results have shown that the present MRT LB model can be used to correctly simulate fluid flows with both density instability and homogeneous reaction in porous media at the pore scale. Therefore, this MRT LB model will be employed for

pore-scale studies of the dissolution-driven density fingering coupled with homogeneous chemical reaction $A + B \rightarrow C$ in Chapters 3-4.

2.2 MRT LB model for flows with heterogeneous reaction

This section further develops LB models for investigating porous media flows with heterogeneous chemical reaction between solid and fluid phases. Two types of reactions are considered. One is the coke combustion with heat transfer and thermal expansion effects. The other is the dissolution of porous matrices during the displacement of two miscible fluids with viscosity contrast. The governing equations for these two processes are firstly built and then corresponding D2Q9 MRT LB models are proposed.

2.2.1 Coke combustion with thermal expansion effects

In a 2D porous medium, coke combustion is assumed to take place at the interface I between coke and hot air as follows [132],

$$\mathrm{C} + \frac{2+N_p}{2+2N_p}\mathrm{O_2} \rightarrow \frac{N_p}{1+N_p}\mathrm{CO} + \frac{1}{1+N_p}\mathrm{CO_2} + Q. \tag{2.28}$$

Note that, both carbon monoxide (CO) and CO_2 are considered as reaction products, with N_p being the $\mathrm{CO}/\mathrm{CO_2}$ mole ratio. The combustion heat released Q is,

$$Q = F_r h_r, \tag{2.29}$$

where h_r is the reaction heat and F_r is the reaction rate (of coke combustion here). During combustion, fluid flow is assumed to satisfy the low Mach number condition and fluid density varies as a consequence of temperature change.

Based on these simplifications and assumptions, governing equations for fluid flow and species evolutions in pore spaces, as well as heat transfer in both pore spaces and solid

phases (solid matrices and solid coke) are built as,

$$\partial_t \rho + \nabla \cdot (\rho \boldsymbol{u}) = 0, \tag{2.30}$$

$$\partial_t (\rho \boldsymbol{u}) + \nabla \cdot (\rho \boldsymbol{u}\boldsymbol{u}) = -\nabla p + \nabla \cdot (\nu \rho \nabla \boldsymbol{u}) + \boldsymbol{F}, \tag{2.31}$$

$$\partial_t (\rho Y_n) + \nabla \cdot (\rho Y_n \boldsymbol{u}) = \nabla \cdot (D_n \rho \nabla Y_n), \tag{2.32}$$

$$\partial_t (\rho c_p T) + \nabla \cdot (\rho c_p T \boldsymbol{u}) = \nabla \cdot (\alpha \rho c_p \nabla T) + Q, \tag{2.33}$$

where ρ, T, c_p, and α are local values of density, temperature, specific heat at constant pressure, and thermal diffusivity, respectively. Y_n and D_n are the mass fraction and diffusion coefficient of species n ($n = \mathrm{O_2}, \mathrm{CO_2}, \mathrm{CO}$), respectively. At the interface I between coke and hot air, coke and $\mathrm{O_2}$ are consumed while products $\mathrm{CO_2}$ and CO are generated via coke combustion as in Eq. (2.28). Thus, coke combustion at interface I is considered as [10, 47],

$$\text{No-slip velocity:} \qquad \boldsymbol{u}^I = (0,\ 0), \tag{2.34}$$

$$\text{Species conservation:} \qquad \boldsymbol{n} \cdot \frac{D_n \rho}{M_n} \nabla Y_n^I = a_n F_r, \tag{2.35}$$

$$\text{Conjugate heat transfer:} \quad \begin{cases} T^{I,+} = T^{I,-}, \\ \boldsymbol{n} \cdot (k \nabla T + \rho c_p \boldsymbol{u} T)^{I,+} = \boldsymbol{n} \cdot (k \nabla T + \rho c_p \boldsymbol{u} T)^{I,-} + q, \end{cases} \tag{2.36}$$

where $\boldsymbol{n}$ is the interface normal pointing to the fluid phase, $+$ and $-$ denote parameters on either side of I, M_n and a_n are the molecular weight and the stoichiometric coefficient of species n, respectively, $k = \alpha \rho c_p$ is the thermal conductivity, and q is the heat flux released by coke combustion.

Considering different thermophysical properties between solid and fluid phases, as well as the thermal expansion effects involved, Eqs. (2.32)-(2.33) are derived to be [128],

$$\partial_t Y_n + \nabla \cdot (Y_n \boldsymbol{u}) = \nabla \cdot (D_n \nabla Y_n) + F_n, \tag{2.37}$$

$$\partial_t T + \nabla \cdot (T \boldsymbol{u}) = \nabla \cdot (\alpha \nabla T) + F_T, \tag{2.38}$$

with source terms for mass fraction and temperature fields being,

$$\begin{aligned} F_n = \frac{D_n}{\rho} \nabla Y_n \cdot \nabla \rho + Y_n \nabla \cdot \boldsymbol{u}, \quad F_T = F_{q1} + F_{q2}, \\ F_{q1} = \frac{Q}{\rho c_p}, \quad F_{q2} = \frac{1}{\rho c_p} \nabla (\rho c_p) \cdot (\alpha \nabla T - T \boldsymbol{u}) - \frac{T}{\rho c_p} \partial_t (\rho c_p). \end{aligned} \tag{2.39}$$

More details about this derivation are provided in Appendix A.

To solve the governing equations (2.30)-(2.31) and (2.37)-(2.38), as well as the coke combustion interface (2.34)-(2.36), a new D2Q9 MRT LB model is developed. The LB evolution equations are,

$$\begin{aligned} f_i(\boldsymbol{x} + \boldsymbol{e}_i \delta_t,\, t + \delta_t) - f_i(\boldsymbol{x},\, t) = &- \left(\boldsymbol{M}^{-1} \boldsymbol{S} \boldsymbol{M}\right)_{ij} \left[f_j(\boldsymbol{x},\, t) - f_j^{eq}(\boldsymbol{x},\, t) \right] \\ &+ \delta_t \left(\boldsymbol{M}^{-1} (\boldsymbol{I} - 0.5\boldsymbol{S}) \boldsymbol{M}\right)_{ij} \left(\overline{F}_j + \overline{C}_j\right), \end{aligned} \tag{2.40}$$

$$\begin{aligned} g_{n,i}(\boldsymbol{x} + \boldsymbol{e}_i \delta_t,\, t + \delta_t) - g_{n,i}(\boldsymbol{x},\, t) = &- \left(\boldsymbol{M}^{-1} \boldsymbol{S}_n \boldsymbol{M}\right)_{ij} \left[g_{n,j}(\boldsymbol{x},\, t) - g_{n,j}^{eq}(\boldsymbol{x},\, t) \right] \\ &+ \delta_t \overline{F}_{n,i} + 0.5 \delta_t^2 \partial_t \overline{F}_{n,i}, \end{aligned} \tag{2.41}$$

$$\begin{aligned} h_i(\boldsymbol{x} + \boldsymbol{e}_i \delta_t,\, t + \delta_t) - h_i(\boldsymbol{x},\, t) = &- \left(\boldsymbol{M}^{-1} \boldsymbol{S}_t \boldsymbol{M}\right)_{ij} \left[h_j(\boldsymbol{x},\, t) - h_j^{eq}(\boldsymbol{x},\, t) \right] \\ &+ \delta_t \overline{F}_{T,i} + 0.5 \delta_t^2 \partial_t \overline{F}_{T,i}, \end{aligned} \tag{2.42}$$

where $\overline{C}_j$ is the correction term to eliminate the deviation from third-order velocity moments [137]. $f_i(\boldsymbol{x},\, t)$, $g_{n,i}(\boldsymbol{x},t)$, and $h_i(\boldsymbol{x},t)$ are distribution functions for density, mass fraction of species n, and temperature, respectively. The corresponding equilibrium distribution functions f_i^{eq}, $g_{n,i}^{eq}$, and h_i^{eq} are given as [137, 140],

$$f_i^{eq} = w_i \rho \left[1 + \frac{\boldsymbol{e}_i \cdot \boldsymbol{u}}{c_s^2} + \frac{(\boldsymbol{e}_i \cdot \boldsymbol{u})^2}{2c_s^4} - \frac{\boldsymbol{u}^2}{2c_s^2} + \Lambda \right], \tag{2.43}$$

$$g_{n,i}^{eq} = w_i Y_n \left[1 + \frac{\boldsymbol{e}_i \cdot \boldsymbol{u}}{c_s^2} + \frac{(\boldsymbol{e}_i \cdot \boldsymbol{u})^2}{2c_s^4} - \frac{\boldsymbol{u}^2}{2c_s^2} \right], \tag{2.44}$$

$$h_i^{eq} = w_i T \left[1 + \frac{\boldsymbol{e}_i \cdot \boldsymbol{u}}{c_s^2} + \frac{(\boldsymbol{e}_i \cdot \boldsymbol{u})^2}{2c_s^4} - \frac{\boldsymbol{u}^2}{2c_s^2} \right], \tag{2.45}$$

with,

$$\Lambda = \frac{\theta - 1}{2c_s^2} \left(\boldsymbol{e}_i^2 - c_s^2 \mathrm{D} + \boldsymbol{e}_i \cdot \boldsymbol{u} \left(\frac{\boldsymbol{e}_i^2}{c_s^2} - \mathrm{D} - 2 \right) \right),\ \theta = \frac{\overline{r} T}{c_s^2},\ \overline{r} = \sum_n \frac{R Y_n}{M_n}. \tag{2.46}$$

Here D is the model dimension and θ is the dimensionless temperature for a gas mixture with thermal expansion effects. Different from classical iso-thermal LB models, the equilibrium density distribution function f_i^{eq} in Eq. (2.43) is obtained by the Hermite expansion of the corresponding continuous one [137]. In this way, the thermal expansion effect is taken into account via the temperature-dependent density. The equation of state to relate the gas pressure and temperature is defined as,

$$p = \rho \overline{r} T. \tag{2.47}$$

To avoid discrete lattice effects, distribution functions and moments for the force term $\boldsymbol{F}$ keep the same as in Eqs. (2.13) and (2.20), respectively. Distribution functions for source terms F_ς are defined as [56, 150],

$$\overline{F}_{\varsigma,i} = w_i F_\varsigma \left(1 + \frac{\boldsymbol{e}_i \cdot \boldsymbol{u}}{c_s^2} \frac{\tau_\varsigma - 0.5}{\tau_\varsigma} \right), \tag{2.48}$$

with $\varsigma = n,\ T$. Time derivatives of $\overline{F}_{\varsigma,i}$ in Eqs. (2.41)-(2.42) and $1/\rho c_p$ in Eq. (2.39) are treated by the backward-difference scheme in Eq. (2.15). In evolution equations (2.40)-(2.42), $\boldsymbol{S}$, $\boldsymbol{S}_n$, and $\boldsymbol{S}_t$ are the diagonal relaxation matrices. Based on the transformation equation (2.3), evolution equations (2.40)-(2.42) are implemented in the moment space as,

$$\hat{\boldsymbol{f}}(\boldsymbol{x} + \boldsymbol{e}_i \delta_t,\ t + \delta_t) = \hat{\boldsymbol{f}}(\boldsymbol{x},\ t) - \boldsymbol{S} \left[\hat{\boldsymbol{f}}(\boldsymbol{x},\ t) - \hat{\boldsymbol{f}}^{eq}(\boldsymbol{x},\ t) \right] + \delta_t (\boldsymbol{I} - 0.5\boldsymbol{S}) \left(\hat{\boldsymbol{F}} + \hat{\boldsymbol{C}} \right), \tag{2.49}$$

$$\hat{\boldsymbol{g}}_n(\boldsymbol{x} + \boldsymbol{e}_i \delta_t,\ t + \delta_t) = \hat{\boldsymbol{g}}_n(\boldsymbol{x},\ t) - \boldsymbol{S}_n [\hat{\boldsymbol{g}}_n(\boldsymbol{x},\ t) - \hat{\boldsymbol{g}}_n^{eq}(\boldsymbol{x},\ t)] + \delta_t \hat{\boldsymbol{F}}_n + 0.5 \delta_t^2 \partial_t \hat{\boldsymbol{F}}_n, \tag{2.50}$$

$$\hat{\boldsymbol{h}}\left(\boldsymbol{x}+\boldsymbol{e}_i\delta_t,\, t+\delta_t\right)=\hat{\boldsymbol{h}}\left(\boldsymbol{x},\, t\right)-\boldsymbol{S}_t\left[\hat{\boldsymbol{h}}\left(\boldsymbol{x},\, t\right)-\hat{\boldsymbol{h}}^{eq}\left(\boldsymbol{x},\, t\right)\right]+\delta_t\hat{\boldsymbol{F}}_T+0.5\delta_t^2\partial_t\hat{\boldsymbol{F}}_T. \quad (2.51)$$

Moments of the equilibrium distribution functions and source terms are expressed as,

$$\hat{\boldsymbol{f}}^{eq}=\rho\left(1,-4+3\boldsymbol{u}^2+2\theta,3-3\boldsymbol{u}^2-2\theta,u,-2u+u\theta,v,-2v+v\theta,u^2-v^2,uv\right), \quad (2.52)$$

$$\hat{\boldsymbol{g}}_n^{eq}=Y_n\left(1,\ -2+3\boldsymbol{u}^2,\ 1-3\boldsymbol{u}^2,\ u,\ -u,\ v,\ -v,\ u^2-v^2,\ uv\right), \quad (2.53)$$

$$\hat{\boldsymbol{h}}^{eq}=T\left(1,\ -2+3\boldsymbol{u}^2,\ 1-3\boldsymbol{u}^2,\ u,\ -u,\ v,\ -v,\ u^2-v^2,\ uv\right), \quad (2.54)$$

$$\hat{\boldsymbol{F}}_\varsigma=F_\varsigma\left(1,-2,1,\left(1-0.5s_{\varsigma,3}\right)u,-\left(1-0.5s_{\varsigma,4}\right)u,\left(1-0.5s_{\varsigma,5}\right)v,-\left(1-0.5s_{\varsigma,6}\right)v,0,0\right). \quad (2.55)$$

The macroscopic variables are finally calculated as,

$$\rho=\sum_i f_i,\quad \rho\boldsymbol{u}=\sum_i\boldsymbol{e}_i f_i+0.5\delta_t\boldsymbol{F},\quad Y_n=\sum_i g_{n,i},\quad T=\sum_i h_i. \quad (2.56)$$

Through the Chapman-Enskog analysis on the proposed LB equations, the constraints on the correction term $\hat{\boldsymbol{C}}$ in the moment space are established as [137],

$$\hat{\boldsymbol{C}}=\left(0,3\left(\partial_xQ_x+\partial_yQ_y\right),-3\left(\partial_xQ_x+\partial_yQ_y\right),0,0,0,0,\partial_xQ_x-\partial_yQ_y,0\right), \quad (2.57)$$

with $Q_x=\rho u\left(1-\theta-u^2\right)$ and $Q_y=\rho v\left(1-\theta-v^2\right)$. Meanwhile, by such an analysis, the governing equations can be recovered with the relaxation times τ, τ_n, and τ_t being,

$$\nu=c_s^2\left(\tau-0.5\right)\theta\delta_t,\quad D_n=c_s^2\left(\tau_n-0.5\right)\delta_t,\quad \alpha=c_s^2\left(\tau_t-0.5\right)\delta_t, \quad (2.58)$$

as well as the gradient terms of mass fraction ∇Y_n and temperature ∇T being [48],

$$\begin{aligned}\nabla_xY_n&=-\frac{\hat{g}_{n,3}-Y_nu+0.5\delta_tF_nu}{c_s^2\tau_n\delta_t},\qquad \nabla_yY_n=-\frac{\hat{g}_{n,5}-Y_nv+0.5\delta_tF_nv}{c_s^2\tau_n\delta_t},\\ \nabla_xT&=-\frac{\hat{h}_3-Tu+0.5\delta_tF_Tu}{c_s^2\tau_t\delta_t},\qquad \nabla_yT=-\frac{\hat{h}_5-Tv+0.5\delta_tF_Tv}{c_s^2\tau_t\delta_t}.\end{aligned} \quad (2.59)$$

In addition to these calculations, the other two gradient terms in Eq. (2.39) are determined using the isotropic central scheme as [155],

$$\nabla\vartheta=\sum_i\frac{w_i\boldsymbol{e}_i\vartheta\left(\boldsymbol{x}+\boldsymbol{e}_i\delta_t\right)}{c_s^2\delta_t},\ \ \left(\vartheta=\rho,\ \rho c_p\right). \quad (2.60)$$

Coke combustion at interface I between coke and hot air is modelled by resolving the interface conditions (2.34)-(2.36). On one hand, conjugate heat transfer conditions (Eq. (2.36)) are automatically achieved by solving the energy equation (2.38). On the other hand, to solve Eqs. (2.34)-(2.35), the finite-difference scheme is used to determine the interface mass fraction gradient ∇Y_n^I as [124],

$$\boldsymbol{n} \cdot \nabla Y_n^I = \frac{Y_n^l - Y_n^I}{0.5\boldsymbol{n} \cdot \boldsymbol{e}_i \delta_x}, \tag{2.61}$$

where Y_n^l is the species mass fraction at the fluid node neighboring interface I. By inserting Eq. (2.61) into Eq. (2.35), Y_n^I is calculated. Then, the halfway bounce-back scheme is adopted to implement this reactive boundary with no-slip velocity (Eq. (2.34)) and given Y_n^I. The unknown distribution functions at fluid node $\boldsymbol{x}_f$ adjacent to I are [124],

$$f_{\bar{i}}\left(\boldsymbol{x}_f,\, t+\delta_t\right) = f_i'\left(\boldsymbol{x}_f,\, t\right), \tag{2.62}$$

$$g_{n,\bar{i}}\left(\boldsymbol{x}_f,\, t+\delta_t\right) = -g_{n,i}'\left(\boldsymbol{x}_f,\, t\right) + 2w_i Y_n^I, \tag{2.63}$$

where $\boldsymbol{e}_{\bar{i}} = -\boldsymbol{e}_i$ ($\boldsymbol{e}_i$ points to solid), $f_i'\left(\boldsymbol{x}_f,\, t\right)$ and $g_{n,i}'\left(\boldsymbol{x}_f,\, t\right)$ denote post-collision values.

Compared with recent SRT LB models for coke combustion in [10] and char-pellet combustion in [132], the proposed MRT LB model makes advances from two perspectives. First, thermal expansion effects are taken into account through the equilibrium density distribution function f_i^{eq} in Eq. (2.43). Second, species conservation in Eq. (2.35) and conjugate heat transfer in Eq. (2.36) are modelled, without iterative calculations, by the bounce-back scheme in Eq. (2.63) and the source term F_{q2} in Eq. (2.39), respectively.

2.2.2 Miscible viscous fingering with dissolution reaction

Miscible displacement between two fluids 1 and 2 is studied in porous media at the pore scale. During the displacement, a heterogeneous dissolution reaction takes place as solute A from fluid 1 comes into contact with solid reactant Bs following the $A + Bs \rightarrow C$ scheme. Here the reaction product C dissolves in the fluid and thus the porous structure varies with the chemical dissolution of solid Bs. Governing equations for fluid flow and concentration transport in pore spaces are built as [45],

$$\nabla \cdot \boldsymbol{u} = 0, \tag{2.64}$$

$$\rho_0 \left(\partial_t \boldsymbol{u} + \boldsymbol{u} \cdot \nabla \boldsymbol{u}\right) = -\nabla p + \nabla \cdot \left(\nu \rho_0 \nabla \boldsymbol{u}\right) + \boldsymbol{F}, \tag{2.65}$$

$$\partial_t C_A + \boldsymbol{u} \cdot \nabla C_A = \nabla \cdot \left(D_A \nabla C_A\right). \tag{2.66}$$

$\mu = \rho_0 \nu$ is the fluid dynamic viscosity with ν being the kinematic viscosity. Effects of mass transfer on fluid viscosity is described by the widely used exponential law as [48],

$$\mu = \mu_2 \exp\left(-\frac{C_A}{C_{A,1}} \mathrm{R}\right), \tag{2.67}$$

where $\mathrm{R} = \ln\left(\mu_2/\mu_1\right)$ is the log-viscosity ratio, and μ_1 and μ_2 are dynamic viscosities of fluid 1 at concentration $C_A = C_{A,1}$ and fluid 2 at concentration $C_A = C_{A,2}$, respectively. To complete the present governing equations, the dissolution reaction $A + Bs \rightarrow C$ at interface I is described by boundary conditions as [47],

$$\text{No-slip velocity:} \qquad \boldsymbol{u}^I = (0,\ 0), \tag{2.68}$$

$$\text{Species conservation:} \qquad \boldsymbol{n} \cdot D_A \nabla C_A^I = F_r, \tag{2.69}$$

where F_r is the reaction rate of the heterogeneous dissolution reaction $A + Bs \rightarrow C$. For non-reactive cases, Eq. (2.69) becomes $\nabla C_A^I = 0$.

To solve the above governing equations and the reactive boundary conditions, a new D2Q9 MRT LB model is developed. Note that, by setting the fluid viscosity as in Eq. (2.67) and excluding the homogeneous reaction rate F_{ro}, Eqs. (2.4)-(2.6) in Sec. 2.1 turn into the present Eqs. (2.64)-(2.66). Therefore, the proposed MRT LB models for these two sets of governing equations are similar. For the sake of brevity, details of the present LB model for solving Eqs. (2.64)-(2.66) are provided in Appendix B. In addition, the dissolution reaction at interface I between fluid 1 and solid Bs is described by the boundary conditions (2.68)-(2.69), which are similar to Eqs. (2.34)-(2.35) for coke combustion. Thus, the boundary scheme in Eqs. (2.61)-(2.63) is extended to model the dissolution reaction $A + Bs \rightarrow C$.

2.2.3 Model validation

Simulations are conducted to demonstrate that the proposed two MRT LB models are capable of simulating porous media flows with heterogeneous reaction between the fluid and solid phases. It is emphasized that, the LB model for miscible displacement with dissolution reaction is an extension of the model in Sec. 2.1 combined with the boundary scheme in Sec. 2.2.1. Thus, this subsection focuses on validating the reliability of the MRT LB model as well as the reactive boundary scheme for coke combustion. Two validation cases with widely-accepted [130] or analytical [125] solutions are selected. One is the counter-flow premixed propane/air flame and the other is the reactive diffusion between two circular surface.

A counter-flow premixed propane flame is firstly simulated. As displayed in Fig. 2.3, the computational domain is $-l_x \leq x \leq l_x$ and $-l_y \leq y \leq l_y$, where premixed propane/air is injected from both top and bottom inlets at a fixed velocity $u_0 = 0.2$ m/s and temperature

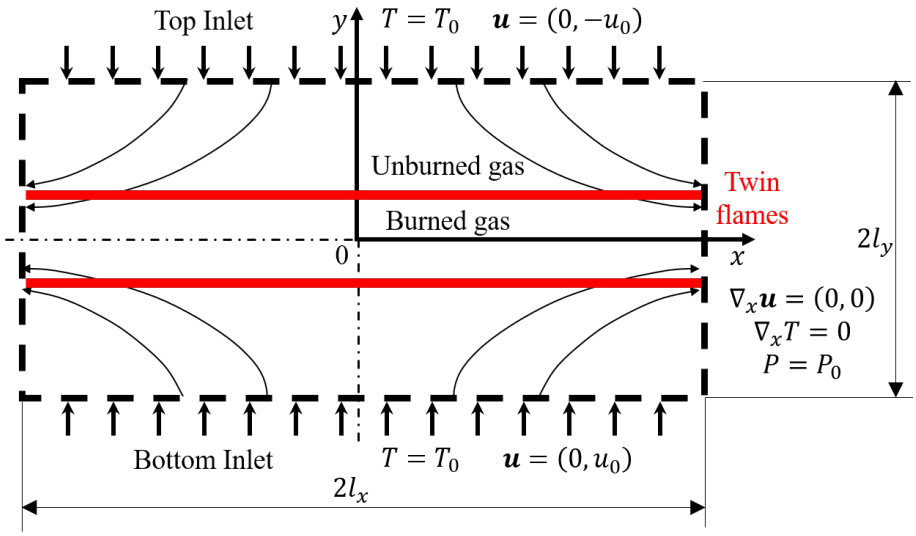

Figure 2.3 Validation test of counter-flow premixed propane/air flame: Computational domain and boundary conditions.

$T_0 = 300$ K. After injection, propane combustion takes place as,

$$C_3H_8 + 5O_2 \rightarrow 3CO + 4H_2O, \quad F_r = AC_{C_3H_8}C_{O_2}\exp\left(-E/RT\right). \tag{2.70}$$

Finally, burned gases leave the domain at two lateral boundaries. In simulations, the viscosity of the propane/air gas mixture is 1.6×10^{-5} m^2/s. The initial mass fractions of C_3H_8, O_2, and N_2 are, 0.0371, 0.2244, and 0.7386, respectively. The reaction coefficients are $A = 9.9 \times 10^{13}$ cm^3/mols, $E = 1.26 \times 10^5$ J/mol, and $hr = 2.05 \times 10^6$ J/mol, respectively. Other simulation parameters are set as, the heat diffusion coefficient $\alpha_g = 2.2 \times 10^{-5}$ m^2/s, the heat capacity $c_{p,g} = 1.01 \times 10^3$ J/kgK, and the diffusion coefficients for each species $D_{C_3H_8} = 1.1 \times 10^{-5}$ m^2/s, $D_{O_2} = 2.1 \times 10^{-5}$ m^2/s, $D_{CO_2} = 1.6 \times 10^{-5}$ m^2/s, $D_{H_2O} = 2.2 \times 10^{-5}$ m^2/s, respectively. A mesh of size $N_x \times N_y = 301 \times 181$ is used after checking the grid independence.

Figure 2.4 shows the comparison results of velocities u/u_0 at $y = 0$ and v/u_0 at $x = 0$, as well as species mass fractions, temperature, and mass reaction rate of C_3H_8 ($F_{r,C_3H_8} = a_{C_3H_8}M_{C_3H_8}F_r$) at $x = 0$. As can be seen, the present simulation results agree

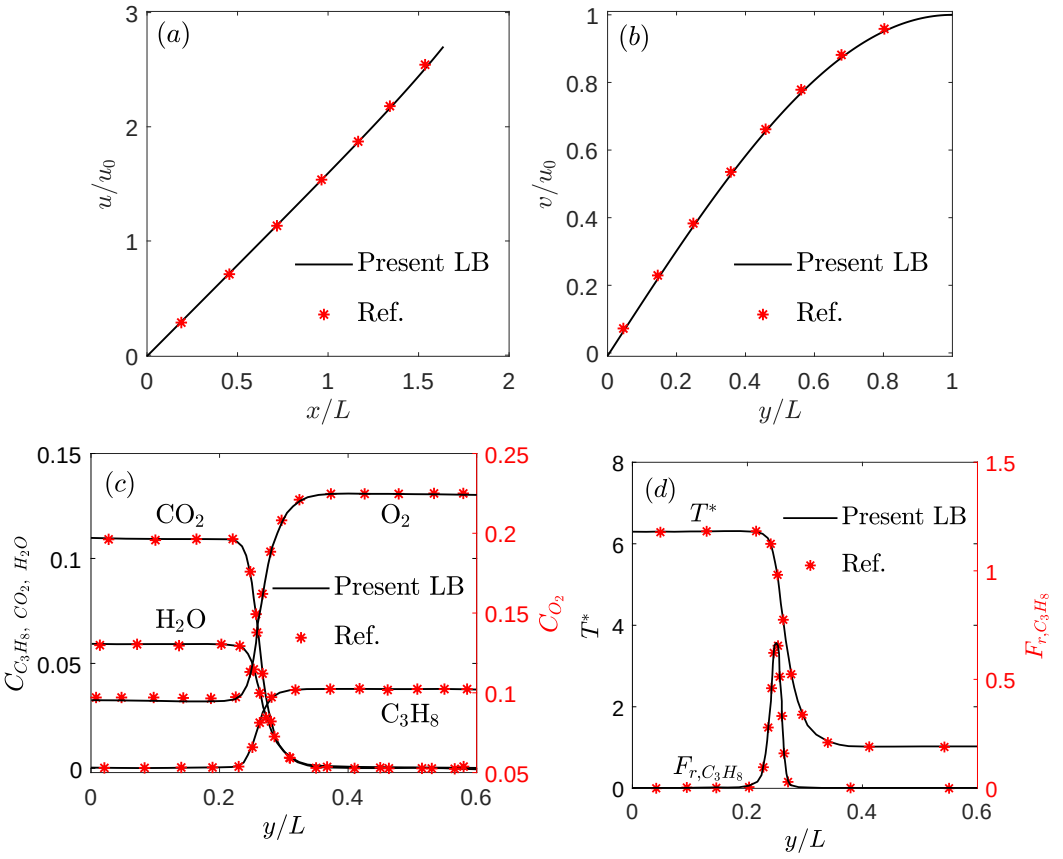

Figure 2.4 Validation test of counter-flow premixed propane/air flame: Comparison of the velocity (a)-(b), species mass fractions (c), and temperature and mass reaction rate of C_3H_8 (d), between the present LB simulation results and the reference data.

well with those benchmark results in [130], indicating the reliability of the developed LB model in simulating combustion.

The accuracy of the developed LB model is further examined, in terms of solving reactive boundary conditions on curved surfaces. For this purpose, the reactive diffusion between two circular surfaces is simulated. As shown in Fig. 2.5, the radii of the two circles are R_i and R_o, respectively. The fluid flow is not considered and the species diffusion takes place in the computational domain $R_i < r = \sqrt{x^2+y^2} < R_o$. The concentration at the inner boundary ($r = R_i$) is fixed as C_i, while a first-order reaction (like coke combustion) is imposed on the outer boundary ($r = R_o$) as $\boldsymbol{n} \cdot D\nabla C(R_o,t) = kC(R_0,t)$. For such a process,

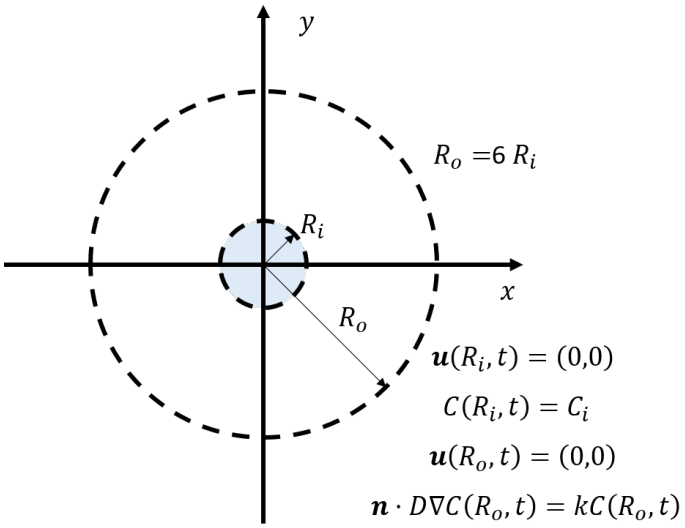

Figure 2.5 Validation test of reactive diffusion between two circular surfaces: Computational domain and boundary conditions.

the analytical solution of the steady-state concentration distribution is [125],

$$C = C_i + \frac{-kC_i}{k\ln(R_o/R_i) + D/R_o}\ln(r/R_i)\,. \tag{2.71}$$

In LB simulations, the circle radius is set as $R_o = 6R_i$ and a mesh of size $N_x \times N_y = 600 \times 600$ is used. The characteristic length and velocity are selected as $L = R_o$ and $U = D/R_o$, respectively. Thus, the Damköhler number is calculated as $\mathrm{Da} = kR_o/D$. Under different Da numbers, the simulated steady-state concentration profiles along the line $R_i < r = \sqrt{x^2 + 0^2} < R_o$ are presented in Fig. 2.6, as well as the values of concentration at the outer surface $C_o(r = R_o)$. As shown, simulated profiles are in good agreement with the analytical solutions, indicating that the proposed LB model can successfully simulate reactions at curved boundaries.

2.3 Summary

This chapter develops three MRT LB models for pore-scale simulations of porous media flows with chemical reaction. In these models, LB equations are built to describe the

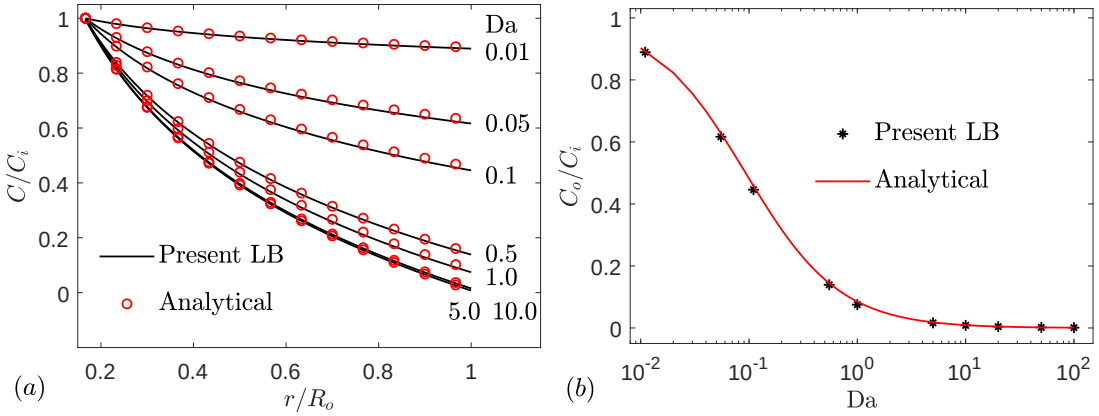

Figure 2.6 Validation test of reactive diffusion between two circular surfaces: Comparison of the steady-state concentration distributions along the line $R_i < r = \sqrt{x^2+0^2} < R_o$ (a) and concentration at the outer circular surface C_o (b) with different Da numbers between the present LB simulation results and analytical solutions in Eq. (2.71).

evolution of distribution functions for velocity, temperature, and species concentration (also mass fraction), respectively. Furthermore, two types of chemical reactions are considered. First, homogeneous chemical reaction $A+B \rightarrow C$ between two miscible fluids is incorporated into the model by introducing reaction source terms. Second, heterogeneous interface reaction (coke combustion and dissolution reaction) is modelled via implementing reactive boundary schemes at the fluid-solid interface. Moreover, in the MRT LB model for porous media flows with homogeneous reaction, different LB equations are developed to describe species transports, thus allowing for different species properties. In the MRT LB model for porous media flows with heterogeneous reaction, the density equilibrium distribution function is modified to include thermal expansion effects, and heat and mass source terms are derived to realize the conjugate heat transfer and species conservation conditions without iterative calculations. Finally, validation simulations have been carried out and the present simulation results match well with existing numerical data or analytical solutions, validating the reliability of these proposed MRT LB models.

Chapter 3 Dissolution-driven density fingering with homogeneous reaction

In a porous medium with a partially miscible top boundary, a buoyantly unstable stratification develops when a species A dissolves from the top boundary into the host fluid. Under effects of the gravity field, such a stratification usually gives rise to density fingering phenomena, which is also known as dissolution-driven density fingering. Once fingering is triggered, both fluid transport and mixing are enhanced by convection. This instability thus affects some industrial applications, such as oil recovery, CO_2 sequestration, and underground contamination treatment [28]. In parallel, the dissolved A may react with another solute B following the $A + B \rightarrow C$ scheme in the host fluid and subsequently modify fingering properties. Due to the wide applications, studies on such porous media flows have gathered great interest recently [28, 73, 78]. In this chapter, dissolution-driven density fingering with homogeneous reaction $A + B \rightarrow C$ is investigated in porous media at the pore scale, aiming to provide useful insights and guidance for industrial applications.

3.1 Problem description

Dissolution-driven density fingering is studied during the displacement between two miscible fluids 1 and 2 in 2D porous media. In this chapter, all the porous media are constructed artificially to share the same porosity ($\phi = 0.69$) and computational domain ($0 \leq x \leq l_x = 1, 0 \leq y \leq l_y = 2/3$), unless otherwise stated [156]. As displayed in Fig. 3.1, fluid 1 containing a chemical solute A is placed upon a porous medium saturated by another

fluid 2. This host fluid 2 in pore spaces contains a dissolved reactant B. These two miscible and incompressible solutions are initially placed in contact along a horizontal interface at $y = 0$, with y pointing into fluid 2 along the gravity field. During the course of time, species A dissolves into the host fluid, and reacts with solute B to give a product C (in the dissolved form) following the $A + B \rightarrow C$ scheme. The reaction rate F_{ro} is taken as [28],

$$F_{ro} = kC_AC_B, \tag{3.1}$$

with k being the kinetic reaction constant. These three chemical species contribute to modify the fluid density ρ. By applying the Boussinesq approximation, ρ is considered as a constant $\rho_0 = 1$ except in the body force term, where it is assumed to vary linearly with species concentrations as [28],

$$\rho = \rho_0 + \rho_0 \left(\beta_A C_A + \beta_B C_B + \beta_C C_C\right), \tag{3.2}$$

here β_r is the concentration expansion coefficient of species r.

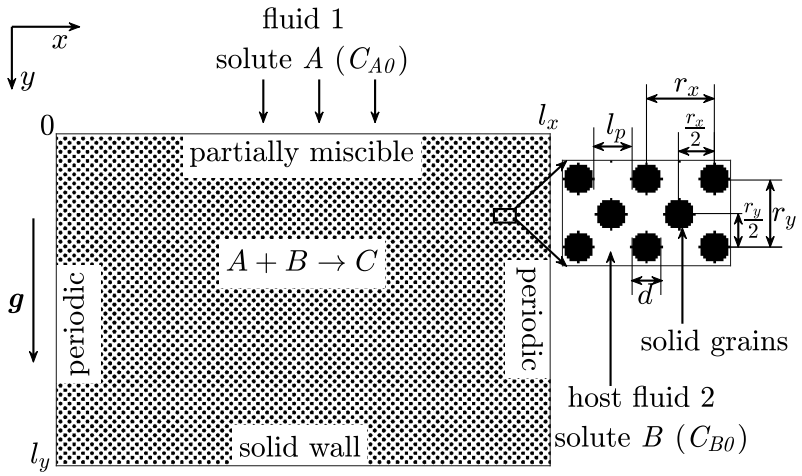

Figure 3.1 The schematic of the problem: Dissolution-driven density fingering with homogeneous reaction $A + B \rightarrow C$ in porous media.

The top boundary ($y = 0$) is assumed to be partially miscible [28]. That is, solute A from fluid 1 dissolves down into the host fluid 2 but no species moves in the reverse

direction. It thus focuses on fluid motion and concentration evolutions of fluid 2, which can be described by Eqs. (2.4)-(2.8). Here, the body force refers to the buoyancy force $\bar{\boldsymbol{F}} = \rho \boldsymbol{g}$ and is expressed as,

$$\boldsymbol{F} = \rho_0 \boldsymbol{g} \left(\beta_A C_A + \beta_B C_B + \beta_C C_C\right), \tag{3.3}$$

with $\boldsymbol{g}$ being the acceleration vector of gravity. Note that, the constant force term $\rho_0 \boldsymbol{g}$ has been absorbed into the pressure term ∇p in Eq. (2.5) [157]. The present governing equations (2.4)-(2.8) can be solved with the initial conditions,

$$\begin{aligned} &C_A\left(x,\, 0 \le y \le \vartheta,\, 0\right) = C_{A0} = 1, \quad C_A\left(x,\, y > \vartheta,\, 0\right) = 0, \\ &C_B\left(x,\, y,\, 0\right) = C_{B0}, \quad C_C\left(x,\, y,\, 0\right) = 0. \end{aligned} \tag{3.4}$$

The concentration of species A at the top boundary ($y = 0$) initially equals its solubility C_{A0} in fluid 2 and this value remains constant over time following the local chemical equilibrium assumption [28]. To trigger density fingering easily, a small perturbation ϑ is introduced in the initial concentration distribution of species A near the top boundary. The value of ϑ randomly varies along the x direction within the range $[0,\, 0.0067 l_x]$. The boundary conditions are also required, and as displayed in Fig. 3.1, the periodic boundary conditions for velocity and species concentrations are applied at the lateral boundaries ($x = 0$ and $x = l_x$). The no-slip and no-flux boundary conditions are used at the solid matrix interfaces ($\boldsymbol{x} = (x_s,\, y_s)$) and the solid bottom wall ($y = l_y$). The partially miscible top boundary ($y = 0$) is set as no-slip and no-flux for B and C but a prescribed concentration for A. These boundary conditions are described by,

$$\begin{aligned} &C_r\left(0,\, y,\, t\right) = C_r\left(l_x,\, y,\, t\right), \qquad \boldsymbol{u}\left(0,\, y,\, t\right) = \boldsymbol{u}\left(l_x,\, y,\, t\right), \\ &\nabla C_r\left(x,\, l_y,\, t\right) = \nabla C_r\left(x_s,\, y_s,\, t\right) = \left(0,\, 0\right), \quad \boldsymbol{u}\left(x,\, l_y,\, t\right) = \boldsymbol{u}\left(x_s,\, y_s,\, t\right) = \left(0,\, 0\right), \\ &C_A\left(x,\, 0,\, t\right) = C_{A0},\ \nabla C_{B,C}\left(x,\, 0,\, t\right) = \left(0,\, 0\right), \qquad \boldsymbol{u}\left(x,\, 0,\, t\right) = \left(0,\, 0\right), \end{aligned} \tag{3.5}$$

The governing equations (2.4)-(2.8) can be expressed in a dimensionless form by introducing the characteristic length L, velocity U, time T, and concentration C_{ch} as,

$$L = l_x, \quad U = \sqrt{g\beta_A L C_{ch}}, \quad T = L/U, \quad C_{ch} = C_{A0}. \tag{3.6}$$

In terms of the following non-dimensional variables,

$$\begin{aligned}
&\boldsymbol{u}^* = \frac{\boldsymbol{u}}{U}, \quad p^* = \frac{p}{\rho_0 U^2}, \quad C_r^* = \frac{C_r}{C_{ch}}, \quad \eta = \frac{C_{B0}}{C_{ch}}, \quad D_B^* = \frac{D_B}{D_A}, \quad D_C^* = \frac{D_C}{D_A}, \\
&x^* = \frac{x}{L}, \quad y^* = \frac{y}{L}, \quad t^* = \frac{t}{T}, \quad \rho^* = \frac{\rho - \rho_0}{\rho_0 \beta_A C_{ch}}, \quad \boldsymbol{F}^* = \frac{\boldsymbol{F}}{\rho_0 U^2/L}, \\
&{F_{ro}}^* = \mathrm{Da} C_A^* C_B^*, \quad \mathrm{Ra}_r = \frac{g\beta_r C_{ch} L^3}{\nu D_A}, \quad \mathrm{Sc} = \frac{\nu}{D_A}, \quad \mathrm{Da} = \frac{k C_{ch} L}{U},
\end{aligned} \tag{3.7}$$

where the asterisked variables are the corresponding dimensionless ones, the dimensionless equations (2.4)-(2.8) read,

$$\nabla \cdot \boldsymbol{u}^* = 0, \tag{3.8}$$

$$\frac{\partial \boldsymbol{u}^*}{\partial t^*} + \boldsymbol{u}^* \cdot \nabla \boldsymbol{u}^* = -\nabla p^* + \sqrt{\frac{\mathrm{Sc}}{\mathrm{Ra}_A}} \nabla \cdot (\nu \nabla \boldsymbol{u}^*) + \boldsymbol{F}^*, \tag{3.9}$$

$$\frac{\partial C_A^*}{\partial t^*} + \boldsymbol{u}^* \cdot \nabla C_A^* = \frac{1}{\sqrt{\mathrm{Ra}_A \mathrm{Sc}}} \nabla^2 C_A^* - {F_{ro}}^*, \tag{3.10}$$

$$\frac{\partial C_B^*}{\partial t^*} + \boldsymbol{u}^* \cdot \nabla C_B^* = \frac{D_B^*}{\sqrt{\mathrm{Ra}_A \mathrm{Sc}}} \nabla^2 C_B^* - {F_{ro}}^*, \tag{3.11}$$

$$\frac{\partial C_C^*}{\partial t^*} + \boldsymbol{u}^* \cdot \nabla C_C^* = \frac{D_C^*}{\sqrt{\mathrm{Ra}_A \mathrm{Sc}}} \nabla^2 C_C^* + {F_{ro}}^*. \tag{3.12}$$

As can be seen, dissolution-driven density fingering with homogeneous reaction $A + B \to C$ is characterized by the Rayleigh numbers Ra_r, the Schmidt number Sc, the Damköhler number Da, the diffusion coefficients D_r^*, and the initial concentration ratio η.

In this chapter, the above governing equations for describing dissolution-driven density fingering with reaction $A + B \to C$ are solved by the D2Q9 MRT LB model in Sec. 2.1. During such LB simulations, the treatment of boundary conditions in Eq. (3.5) plays an

important role. The no-slip velocity and impermeable concentration conditions at the solid bottom and the porous matrix interfaces are implemented by the halfway bounce-back scheme [158, 159]. The partially miscible condition at the top boundary is treated by the non-equilibrium extrapolation scheme [38]. It is noted that this chapter focuses on interactions between reaction and density fingering. To avoid differential diffusion effects, the molecular diffusion coefficients D_r of three species are set as an identical constant D in this chapter. Then, by adding Eqs. (3.11) and (3.12) and taking into account the initial and boundary conditions in Eqs. (3.4)-(3.5), the concentrations of species B and C are expected to remain constant as $C_B + C_C = C_{B0}$. Then, the dimensionless force term is rewritten as,

$$\boldsymbol{F}^* = \frac{\boldsymbol{F}}{\rho_0 U^2/L} = \left(C_A^* + \frac{\Delta \mathrm{Ra}_{CB}}{\mathrm{Ra}_A} C_B^* + \frac{\mathrm{Ra}_B}{\mathrm{Ra}_A}\eta \right) \boldsymbol{j} \tag{3.13}$$

with $\Delta \mathrm{Ra}_{CB} = \mathrm{Ra}_C - \mathrm{Ra}_B$ representing the relative contribution to density of product C and reactant B. Therefore, in the following LB simulations, the Schmidt number is fixed as $\mathrm{Sc} = 100$, and different values of Ra_r, Da, and η are selected to change the test conditions. In addition, the characteristic parameters in Eq. (3.6) are set as,

$$L = l_x = 1, \quad U = \sqrt{g\beta_A L C_{A0}} = 0.177, \quad T = L/U = 5.65, \quad C_{ch} = C_{A0} = 1, \tag{3.14}$$

and they are all in lattice units. Based on these characteristic numbers, the relevant parameters in LB simulations can be calculated as,

$$\begin{aligned} \nu &= \frac{LU}{\sqrt{\mathrm{Ra}_A/\mathrm{Sc}}}, \quad D = \frac{LU}{\sqrt{\mathrm{Ra}_A \mathrm{Sc}}}, \quad C_{B0} = C_{A0}\eta, \\ \tau &= \frac{\nu}{c_s^2 \delta_t} + \frac{1}{2}, \quad \tau_r = \frac{D}{c_s^2 \delta_t} + \frac{1}{2}, \quad k = \frac{U\mathrm{Da}}{LC_{A0}}. \end{aligned} \tag{3.15}$$

Before proceeding further, grid convergence tests have been carried out for all the porous media in this chapter. A mesh of size $N_x \times N_y = 1500 \times 1000$ is chosen for the subsequent simulations, unless otherwise noted.

3.2 General fingering dynamics with reaction $A + B \rightarrow C$

The general phenomena of dissolution-driven density fingering with homogeneous reaction $A + B \rightarrow C$ are firstly investigated in a homogeneous porous medium HO. As displayed in Fig. 3.1, the porous network contains a staggered array of circular grains with a uniform diameter $d = 12\delta_x$ (the lattice spacing is $\delta_x = l_x/N_x$). Every grain center $G_{HO} = (x_c,\ y_c)$ is located on a grid node and obeys a regular staggered distribution. The closest centre-to-centre distances between two cylinders in x and y directions are $r_x = 27\delta_x$ and $r_y = 27\delta_x$, respectively, and the single pore size is calculated as $l_p = r_x - d = 15\delta_x$.

After a series of simulations and comparisons, the density fingering phenomena can be divided into two non-reactive and four reactive groups, based on the Rayleigh numbers Ra_r of chemical species. To be specific, these six groups are described as follows:

- For $\mathrm{Ra}_A > 0$, non-reactive unstable.

  (1) Non-reactive group NR: The dissolution of species A into the host fluid is buoyantly unstable and can trigger density fingering.

  (2) Reactive group R1: Reaction product C is less dense than B ($\Delta\mathrm{Ra}_{CB} < 0$) and thus reaction $A + B \rightarrow C$ suppresses the development of density fingering.

  (3) Reactive group R2: Reaction enhances fingering development provided C is sufficiently denser than B ($\Delta\mathrm{Ra}_{CB} > 0$).

- For $\mathrm{Ra}_A < 0$, non-reactive stable.

  (4) Non-reactive group NRS: The dissolution of species A into the host fluid is buoyantly stable.

(5) Reactive group R3: Reaction $A + B \rightarrow C$ with $\Delta \mathrm{Ra}_{CB} > 0$ creates an unstable density stratification and triggers the development of density fingering.

(6) Reactive group R4: The system with reaction ($\Delta \mathrm{Ra}_{CB} < 0$) remains stable.

This classification is similar to existing predictions by linear stability analysis in [81], with differential diffusion effects being ignored. As an example, a few test conditions are provided in Table 3.1 to investigate the general fingering phenomena, including one non-reactive Test NR, and three reactive Tests R1-R3. Note that, the non-reactive group NRS and the reactive group R4 are not included because no fingering develops in these two stable systems. Figure 3.2 depicts the numerical density distributions varying with time for Tests NR and R1-R3, which reflect the typical characteristics of dissolution-driven density fingering in different groups.

Table 3.1 Parameters for Tests NR and R1-R3.

Tests	Parameters
NR	$\mathrm{Ra}_A = 10^9; \quad \mathrm{Da} = 0; \quad \eta = 0;$
R1	$\mathrm{Ra}_A = 10^9; \quad \Delta \mathrm{Ra}_{CB} = -10^9; \quad \mathrm{Da} = 5; \quad \eta = 1;$
R2	$\mathrm{Ra}_A = 10^9; \quad \Delta \mathrm{Ra}_{CB} = 10^9; \quad \mathrm{Da} = 5; \quad \eta = 1;$
R3	$\mathrm{Ra}_A = -10^9; \quad \Delta \mathrm{Ra}_{CB} = 10^9; \quad \mathrm{Da} = 5; \quad \eta = 1;$

The results show that the general dynamics of dissolution-driven density fingering in each test follow four similar stages. First, the miscible interface between A-enriched fluid 2 and fresh host fluid 2 almost remains planar (Fig. 3.2(a)), with diffusion dominating the flow dynamics. Then, with the dissolution of A, the flat interface deforms gradually and fingers of denser fluid appear and sink into the deep host fluid (Fig. 3.2(b)). After that, fingers begin to interact and merge with their neighbors, making the number of fingers decrease dramatically (Figs. 3.2(c)-(d)). Finally, small new fingers regenerate from the top

boundary and join the existing ones, leading to the fixed number of fingers (Figs. 3.2(e)-(f)).

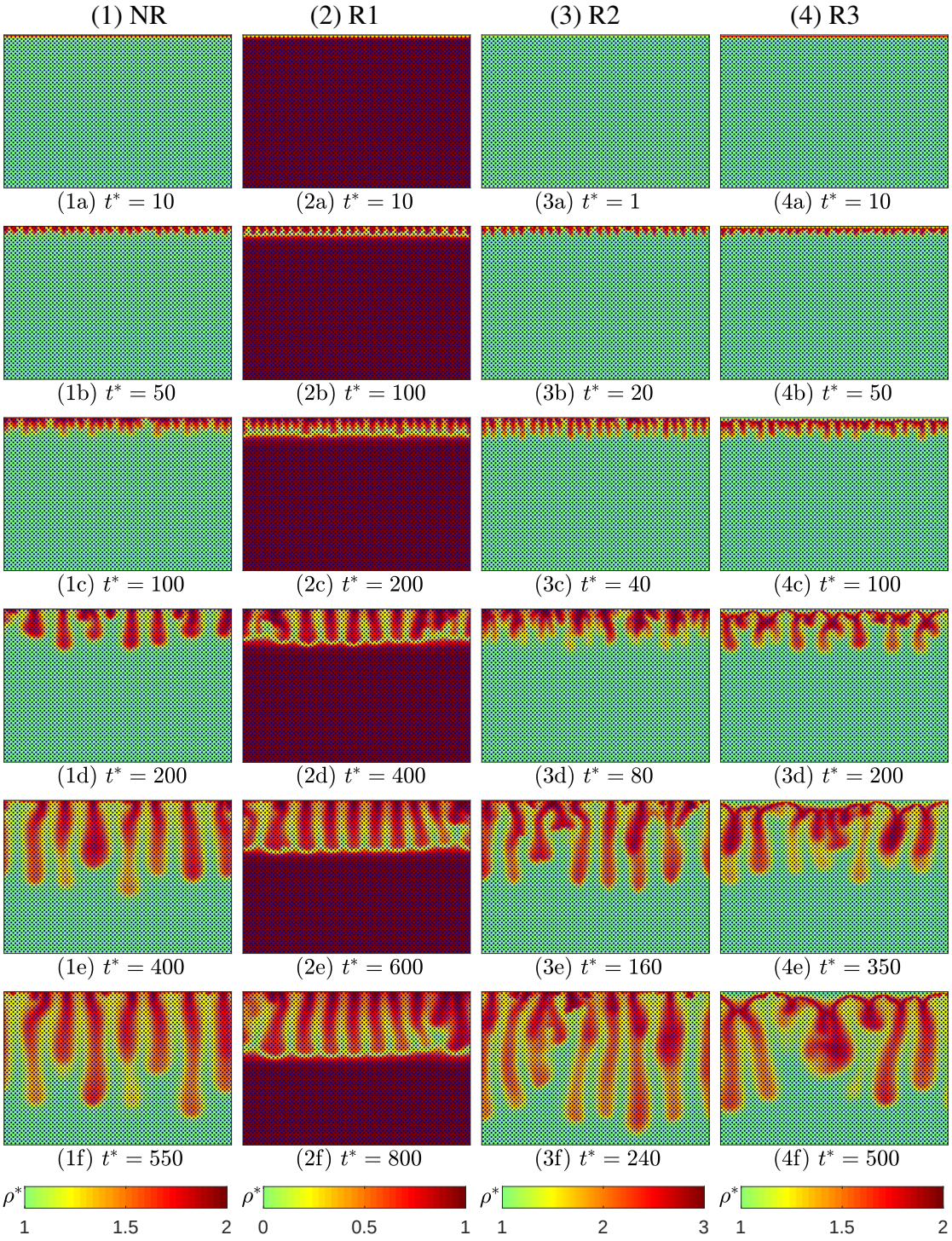

Figure 3.2 Contours of density fields ρ^* at six time instants t^* (a)-(f), for Tests NR (1), R1 (2), R2 (3), and R3 (4) in the homogeneous porous medium HO.

Together with these similarities, differences between fingering behaviours in Tests NR and R1-R3 are obvious as well. This is explained with the help of horizontally averaged density $\overline{\rho}^*$ in Fig. 3.3. In Test NR, density fingering develops with the dissolution of A (Fig. 3.2(1)) and the density profile at every time instant decreases monotonically (Fig. 3.3(1)). Compared with this non-reactive case, dissolution-driven density fingering coupled with reaction $A + B \rightarrow C$ develops more slowly in Test R1 (Fig. 3.2(2)). It is because product C cannot compensate for the consumption of reactant B in terms of density evolution ($\Delta \mathrm{Ra}_{CB} < 0$). Such a density contrast between B and C brings in a density profile with a local minimum, which has also been reported at the REV scale [28]. Seen from Fig. 3.3(2), each density curve decreases from the top boundary to the density minimum (top layer) and then increases until the bottom boundary (bottom layer). So, dissolution-driven density fingering develops in the unstable top stratification, while the buoyantly stable bottom layer acts as a barrier to counteract fingering propagation.

Note that, different from previous REV-scale results [28], the minimum density area keeps narrow and does not transit to span a certain depth. For pore- and REV-scale simulations, Tartakovsky *et al.* [160, 161] have argued that the REV-scale flow and transport equations can be obtained by averaging the corresponding pore-scale ones over a support volume, but the use of effective dispersion and permeability models at the REV scale tends to over-predict the degree of mixing and reaction. In addition, they simulated the transport of two solutes A and B coupled with reaction $A + B \rightarrow C$ in porous media at both REV and pore scales. Their results revealed that the REV-scale model overestimated the global mass of product C, implying the overestimated reaction rate between solutes A and B at the REV scale. This finding is applied to explain the inconsistency between the

present pore-scale and previous REV-scale results: REV-scale simulations over-predict the reaction intensity and thus introduce a fast reaction zone with a local minimum density over a certain depth.

By contrast, density fingering appears earlier and elongates more rapidly in Test R2 (Fig. 3.2(3)) than in Test NR (Fig. 3.2(1)). This is expected since the contribution to density of C is sufficiently larger than B ($\Delta\mathrm{Ra}_{CB} > 0$). Under this condition, every density profile in Fig. 3.3(3) decreases monotonically along the y direction as in Test NR. But product C enlarges the density difference from the top ($y = 0$) to the bottom ($y = l_y$) and subsequently enhances the fingering growth. Similarly, in Test R3, dissolution-driven density fingering develops due to the inclusion of reaction $A + B \rightarrow C$ with $\Delta\mathrm{Ra}_{CB} > 0$ (Fig. 3.2(4)), even though its non-reactive counterpart is stable. The density profiles in this test show a non-monotonic fashion (Fig. 3.3(4)): each curve has a reaction-induced maximum. Density fingering develops in the unstable bottom layer, while the stable top layer corresponds to the narrow stagnant liquid layer near the top boundary (Fig. 3.2(4)).

Generally, in agreement with previous theoretical predictions [81], six kinds of fingering scenarios are identified from the present pore-scale simulations. Each case has a specific type of density profile and the non-monotonic type appears when Ra_A and $\Delta\mathrm{Ra}_{CB}$ have the opposite signs. However, density profiles in Fig. 3.3 fluctuate at later time instants due to the non-linear fingering development, which cannot be theoretically predicted by linear stability analysis. In addition, similar to REV-scale findings [28], the present study demonstrates that the homogeneous reaction $A + B \rightarrow C$ can stabilize (Test R1), destabilize (Test R2), and trigger (Test R3) dissolution-driven density fingering. Nevertheless, different from REV-scale density profiles, no plateau with $\overline{\rho}^*$ keeping constant

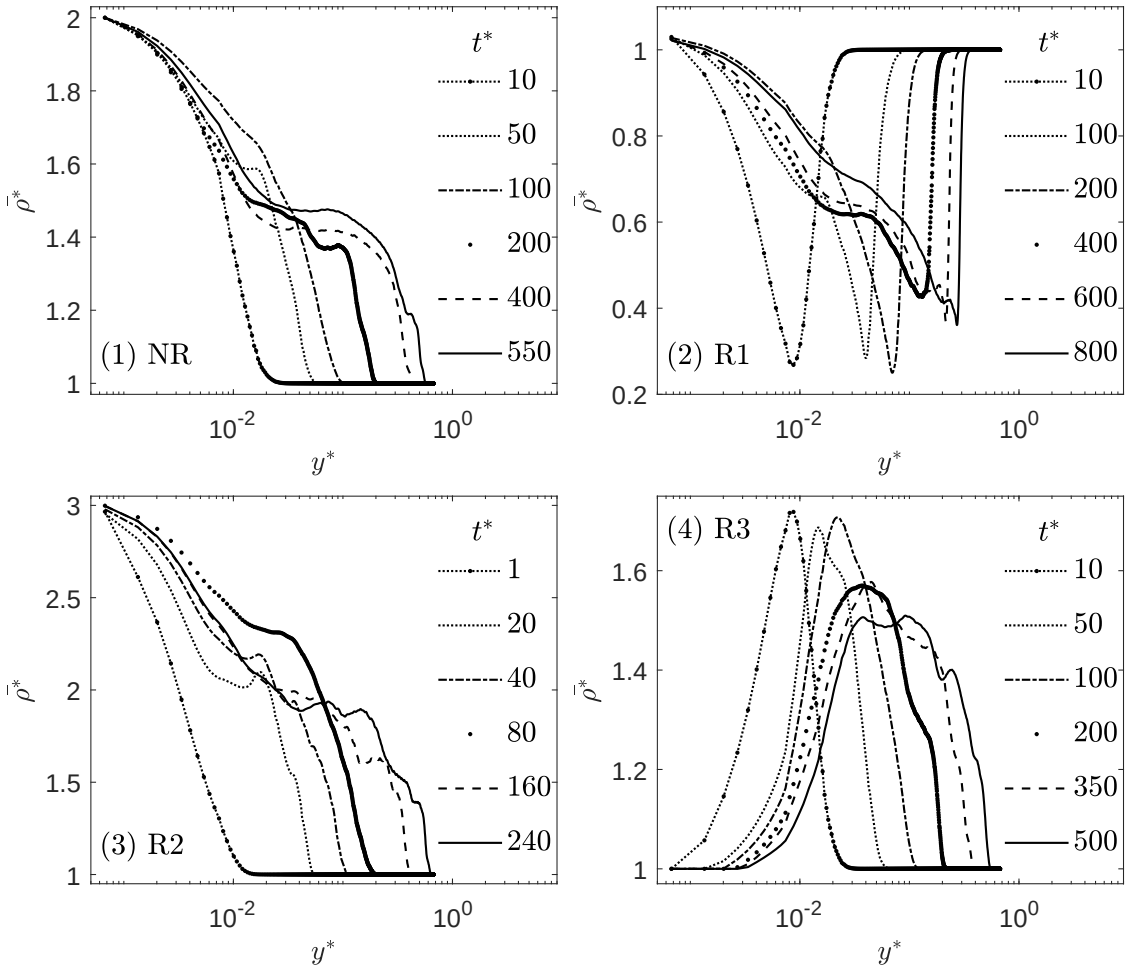

Figure 3.3 Horizontally averaged density $\overline{\rho}^*$ at six time instants t^*, for Tests NR (1), R1 (2), R2 (3), and R3 (4) in the homogeneous porous medium HO.

as a minimum exists in the present pore-scale results (Fig. 3.3). This is attributed to the over-prediction of reaction intensity at the REV scale. Therefore, the present pore-scale results enrich the understanding of dissolution-driven density fingering with homogeneous reaction $A + B \rightarrow C$ in porous media.

3.3 Effects of parameters ΔRa_{CB}, η, and Da

After observations of the general fingering phenomena, a parametric study is further carried out to investigate dissolution-driven density fingering with homogeneous reaction

$A + B \rightarrow C$ under various conditions. In the homogeneous medium HO, Tests I – III are carried out to evaluate the relationship between fingering and reaction $A + B \rightarrow C$. As summarized in Table 3.2, different values of $\Delta\mathrm{Ra}_{CB}$, η, and Da are considered. Note that, Test I with fixed Ra_A and varying $\Delta\mathrm{Ra}_{CB}$ represents different reactants A, B, and product C.

Table 3.2 Parameters for Tests I – III.

Tests	Parameters $\left(\mathrm{Ra}_A = 10^9\right)$
I	$\Delta\mathrm{Ra}_{CB}/\mathrm{Ra}_A = -1,\ 0,\ 0.25,\ 0.5,\ 0.75,\ 1; \quad \mathrm{Da} = 5; \quad \eta = 1;$
II	$\eta = 0.1,\ 0.5,\ 1,\ 1.5,\ 2; \quad \Delta\mathrm{Ra}_{CB} = 10^9; \quad \mathrm{Da} = 5;$
III	$\mathrm{Da} = 1,\ 5,\ 10,\ 50,\ 100; \quad \Delta\mathrm{Ra}_{CB} = 10^9; \quad \eta = 1;$

3.3.1 Fingering extension depth l_m

The quantity l_m is defined as the most advanced vertical position of fingering tips, which represents the extension of dissolution-driven density fingering along the propagation direction. Temporal evolutions of l_m for Test I are displayed in Fig. 3.4 along with the corresponding non-reactive results for comparison. It is shown that l_m for each $\Delta\mathrm{Ra}_{CB}$ matches well in the early stage, when diffusion dominates the fluid dynamics (Figs. 3.2(a)). After a short period t_s, l_m starts to depart from the initial diffusive trend and increase faster. This is because the unstable stratification becomes intensified with the dissolution of A from the top boundary, which finally gives rise to the appearance of density fingering at t_s (Fig. 3.2(b)). The time period t_s decreases monotonically as $\Delta\mathrm{Ra}_{CB}$ increases, implying the increasing destabilizing effects of reaction $A + B \rightarrow C$. Besides, a critical value $\Delta\mathrm{Ra}_{CB1} = 0.25\mathrm{Ra}_A$ is identified, above which the reactive l_m deviates from the diffusion stage earlier than the non-reactive one. On the basis of this property, the chemical stabilizing ($\Delta\mathrm{Ra}_{CB} <$

ΔRa_{CB1}) and destabilizing ($\Delta Ra_{CB} > \Delta Ra_{CB1}$) domains are identified for the early stage. During this period, effects of ΔRa_{CB} are coherent with theoretical predictions and the critical value ΔRa_{CB1} is of the same order as the theoretical one $0.32Ra_A$ in [81].

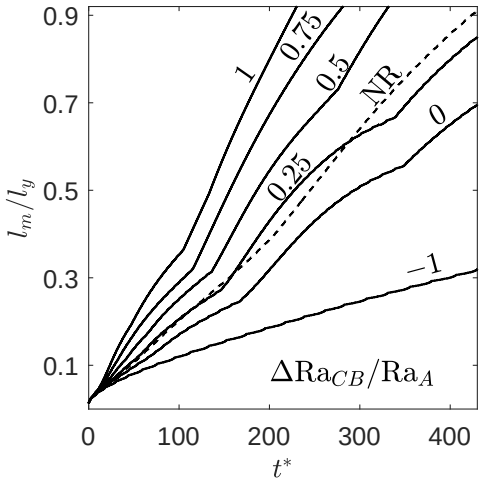

Figure 3.4 Temporal evolutions of fingering extension depth l_m for Test I with different values of ΔRa_{CB} in the homogeneous medium HO.

After this transition, each curve of l_m in Fig. 3.4 grows with time and finally reaches the bottom at t_e. t_e decreases with increasing ΔRa_{CB} and thus another critical value $\Delta Ra_{CB2} = 0.5Ra_A$ appears. Beyond this value, fingering with chemical reaction arrives at the bottom earlier than its non-reactive counterpart. Similarly, the chemical stabilizing ($\Delta Ra_{CB} < \Delta Ra_{CB2}$) and destabilizing ($\Delta Ra_{CB} > \Delta Ra_{CB2}$) regions are divided for the later fingering development stage. Note that, for the case with $\Delta Ra_{CB} = \Delta Ra_{CB1} \sim \Delta Ra_{CB2}$, dissolution-driven density fingering starts earlier but reaches the bottom later than the non-reactive Test NR. This is because the non-linear fingering growth and interactions at later times slow down the vertical progression of dissolution-driven density fingering. This later-stage critical value ΔRa_{CB2} is introduced by non-linearities and thus cannot be predicted by linear stability analysis in [81].

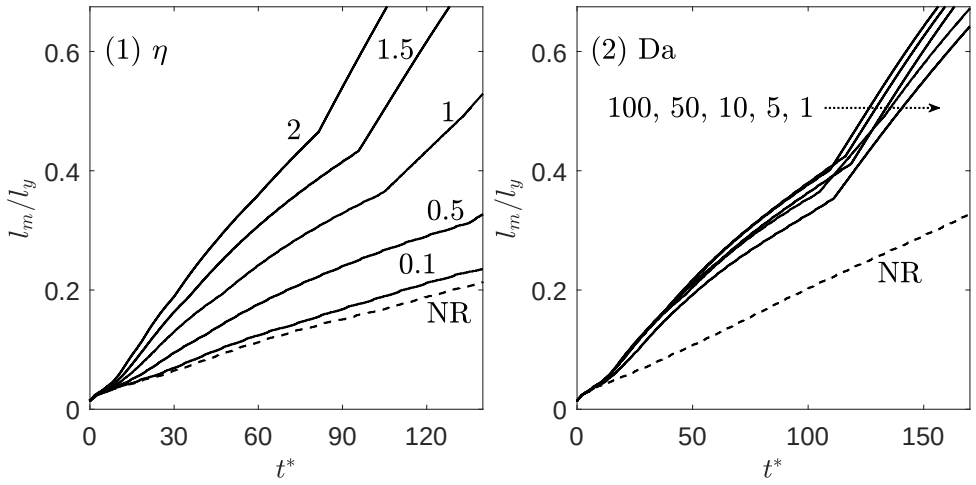

Figure 3.5 Temporal evolutions of fingering extension depth l_m for Tests II (1) and III (2) with varying η and Da, respectively, in the homogeneous medium HO.

The simulated curves of l_m for Tests II-III are then illustrated in Fig. 3.5. All the reactive cases have smaller t_s and t_e than their non-reactive counterpart, which implies the homogeneous reaction $A+B \rightarrow C$ keeps accelerating the onset and growth of fingering. Furthermore, as η (Fig. 3.5(1)) or Da (Fig. 3.5(2)) increases, differences between the reactive and non-reactive values of t_s (or t_e) are amplified, showing the boosted destabilizing effects of reaction on density fingering. Considering these two sets of tests locate in the reactive group R2 with $\Delta \mathrm{Ra}_{CB} > 0$, the influence of η and Da are then investigated in the reactive group R1 with $\Delta \mathrm{Ra}_{CB} < 0$, where reaction $A+B \rightarrow C$ stabilizes density fingering. Results show that increasing η or Da promotes the stabilizing effects of reaction. This tendency is similar to that in Fig. 3.5 and is not analyzed here for brevity. In conclusion, increasing η or Da intensifies the influence of reaction $A+B \rightarrow C$ on fingering development. By changing these two parameters, however, how the reaction affects fingering (stabilizing or destabilizing) cannot be modified. On the contrary, the influence of $\Delta \mathrm{Ra}_{CB}$ is much complex. Increasing $\Delta \mathrm{Ra}_{CB}$ boosts the destabilizing effects of reaction and thus covers both

the stabilizing and the destabilizing regimes. To obtain a comprehensive understanding, effects of ΔRa_{CB} are further analyzed and quantified in the next subsections.

3.3.2 Overall reaction strength

To better examine whether or not dissolution-driven density fingering returns to affect reaction $A + B \rightarrow C$, the volume-averaged reaction rate $\langle R^* \rangle$ is calculated. $\langle R^* \rangle$ reflects the global reaction strength and results for Test I are illustrated in Fig. 3.6. Each profile of $\langle R^* \rangle$ evolves with time non-monotonically at first and fluctuates around a steady-state value $\langle R^* \rangle_s$ after a while. $\langle R^* \rangle_s$ is limited by the steady-state mass flux J_s^* of species A from the top boundary as shown in Fig. 3.7(2). Regardless of the fluctuations, the global reaction rate $\langle R^* \rangle$ increases with ΔRa_{CB}. This is expected since chemical reaction increasingly destabilizes the development of density fingering. To be specific, the stronger density fingering elongates the contact zone between A and B more obviously. In the meantime, the destabilized fingering accompanied with stronger convection brings B up to react with A more efficiently. The combination of the larger contact zone and reaction rate leads to the increase in $\langle R^* \rangle$. Thus, dissolution-driven density fingering and reaction promote each other more strongly with increasing ΔRa_{CB}.

3.3.3 Storage of A in the host fluid

In some industrial applications (like the geological CO_2 sequestration), the dissolution of species A into the host fluid is favourable. Thereby, effects of dissolution-driven density fingering with reaction $A + B \rightarrow C$ on storage behaviours of A in the host fluid are investigated. For this purpose, the horizontally averaged mass flux of species A at the top

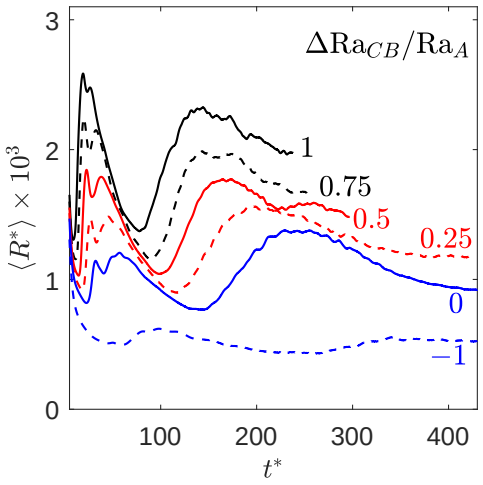

Figure 3.6 Temporal evolutions of the volume-averaged reaction rate $\langle R^* \rangle$ for Test I with different values of $\Delta \mathrm{Ra}_{CB}$ in homogeneous medium HO.

boundary is introduced as [162],

$$J^*(t) = -\frac{1}{l_x^* \sqrt{\mathrm{Ra}_A \mathrm{Sc}}} \int_0^{l_x^*} \partial_{y^*} C_A^*(x^*,\, 0)\, dx^*. \tag{3.16}$$

This parameter acts as an indicator of the diffusion speed of A into the host fluid. Temporal profiles of J^* are recorded in Fig. 3.7(1), showing a similar pattern in both non-reactive and reactive cases. Specifically, J^* initially decreases with time as long as diffusion dominates the transport process (Fig. 3.2(a)); then it starts to increase with the development of density fingering (Fig. 3.2(b)); after that it decreases again because of fingering merging (Figs. 3.2(c)-(d)); and finally it fluctuates around a steady-state value J_s^* corresponding to the nearly unchanged number of fingers (Figs. 3.2(e)-(f)). Note that, the later-stage fluctuations of J^* in Fig. 3.7(1) are introduced by the appearance of new fingering: J^* increases when new fingers occur and decreases as these new fingers merge with existing old ones. These behaviors of J^* verify that density fingering promotes the dissolution speed of A into the host fluid. In addition, every reactive J^* is larger than the non-reactive counterpart and the difference grows with $\Delta \mathrm{Ra}_{CB}$ (Fig. 3.7(1)). It is because the chemical

consumption of A increases the concentration gradient $\partial_{y^*} C_A^*$ at the top boundary, hence the larger J^* based on Eq. (3.16). Besides, the larger $\Delta \mathrm{Ra}_{CB}$ leads to the stronger reaction (Fig. 3.6) and subsequently the faster diffusion of A into the host fluid.

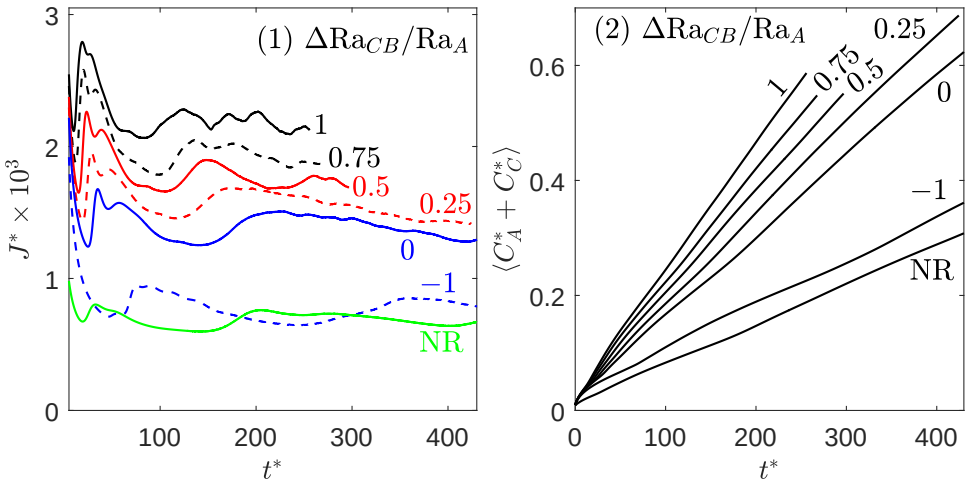

Figure 3.7 Temporal evolutions of horizontally averaged mass flux of A at the top boundary J^* (1) and stored amount of A in the host fluid $\langle C_A^* + C_C^* \rangle$ (2), for Test I with different values of $\Delta \mathrm{Ra}_{CB}$ in homogeneous medium HO.

In order to further quantify the storage behaviors, the amount of A stored in the host fluid is calculated. Considering the fact that species A is stored in forms of both un-reacted A and product C (reacted A), the stored A is defined as the volume-averaged concentration $\langle C_A^* + C_C^* \rangle$ [28]. As shown in Fig. 3.7(2), every curve of $\langle C_A^* + C_C^* \rangle$ increases with time monotonically. This can be explained by the evolution equation [28, 163],

$$\frac{\partial \langle C_A^* + C_C^* \rangle}{\partial t^*} = l_x^* J^*. \tag{3.17}$$

It is obtained by integrating equations (3.10) and (3.12) over the whole domain and taking into account the boundary conditions in Eq. (3.5). As the corresponding dissolution flux J^* remains positive in Fig. 3.7(1), the equation (3.17) expresses that $\langle C_A^* + C_C^* \rangle$ increases with time monotonically. On the other hand, results in Fig. 3.7(2) demonstrate that all the reactive lines of $\langle C_A^* + C_C^* \rangle$ increase more quickly than the non-reactive one, implying

the promoting effects of reaction on the storage of A in the host fluid. Furthermore, the growing speed of every reactive $\langle C_A^* + C_C^* \rangle$ in Fig. 3.7(2) increases with ΔRa_{CB}, which is consistent with the change of J^* in Fig. 3.7(1). Thus, the calculated J^* and $\langle C_A^* + C_C^* \rangle$ suggest that density fingering with reaction $A + B \rightarrow C$ enhances the storage of species A in the host fluid. Such an enhancing effect is intensified with the increasing ΔRa_{CB}.

In general, a comprehensive parametric study of dissolution-driven density fingering with homogeneous reaction $A + B \rightarrow C$ has been performed. The present pore-scale results about effects of ΔRa_{CB} and η are qualitatively similar to previous theoretical predictions [81] and REV-scale findings [28]. During the non-linear growth period however, the present critical value ΔRa_{CB2} to distinguish the stabilizing and destabilizing effects of chemistry has not been theoretically predicted by linear stability analysis [81]. In addition, the impact of Da is investigated, showing that increasing Da amplifies the influence of reaction on fingering development.

3.4 Fingering in heterogeneous porous media

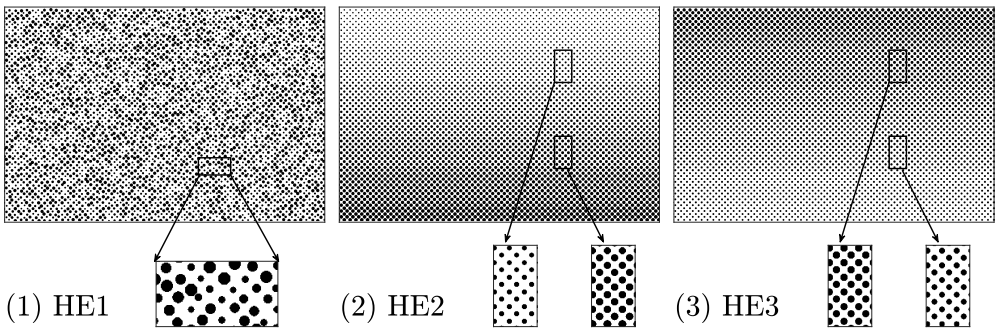

Figure 3.8 Schematic diagrams of heterogeneous media HE1-HE3.

Having investigated the general fingering dynamics in the homogeneous medium HO, effects of medium heterogeneity are further explored. As constructed in Fig. 3.8, three

types of heterogeneous porous media (HE1-HE3) are considered. The porous network HE1 in Fig. 3.8(1) is composed of randomly distributed circular grains with random diameters. The spatial location of each grain center is firstly generated as in medium HO (Fig. 3.1) and then a random perturbation $(x_p,\ y_p)$ is added to each grain center as $G_{HE1} = (x_c + x_p,\ y_c + y_p)$. The perturbations x_p and y_p are all in the range of $[-\delta_x,\ 4\delta_x]$. Each grain diameter d is randomly determined by [156],

$$d(\zeta) = \begin{cases} d_{min}, & 0 \le \zeta < \delta, \\ d_{min} + \frac{d_{max} - d_{min}}{1-2\delta}(\zeta - \delta), & \delta \le \zeta \le 1-\delta, \\ d_{max}, & 1-\delta < \zeta < \delta, \end{cases} \tag{3.18}$$

where the random number ζ is confined within the interval $[0,\ 1]$, $d_{min} = 8\delta_x$ and $d_{max} = 16\delta_x$ are the minimum and maximum values of the grain diameter, and parameter δ is selected as 0.05. Such a determination yields the mean grain diameter $12\delta_x$. On the other side, heterogeneous media HE2 and HE3 consist of regular circular grains with vertically decreasing (HE2) or increasing (HE3) pore spaces (permeability). The grain centers in these two media are determined as in medium HO ($G_{HE2} = G_{HE3} = (x_c,\ y_c)$) and the vertical grain diameter gradient λ is calculated as,

$$\lambda = \frac{d_b - d_t}{l_y}, \tag{3.19}$$

where d_b and d_t represent grain diameters at the bottom and the top layers, respectively. Based on this definition, positive and negative values of λ correspond to media with decreasing (HE2) and increasing (HE3) pore spaces along the flow direction, respectively. Here, parameters $d_t = 7\delta_x$, $\lambda = 0.01$, $r_x = r_y = 27\delta_x$, and $l_{p,t} = 20\delta_x$ are selected to

generate medium HE2 in Fig. 3.8(2); and $d_t = 15\delta_x$, $\lambda = -0.006$, $r_x = r_y = 27\delta_x$, and $l_{p,t} = 12\delta_x$ are used for medium HE3 in Fig. 3.8(3).

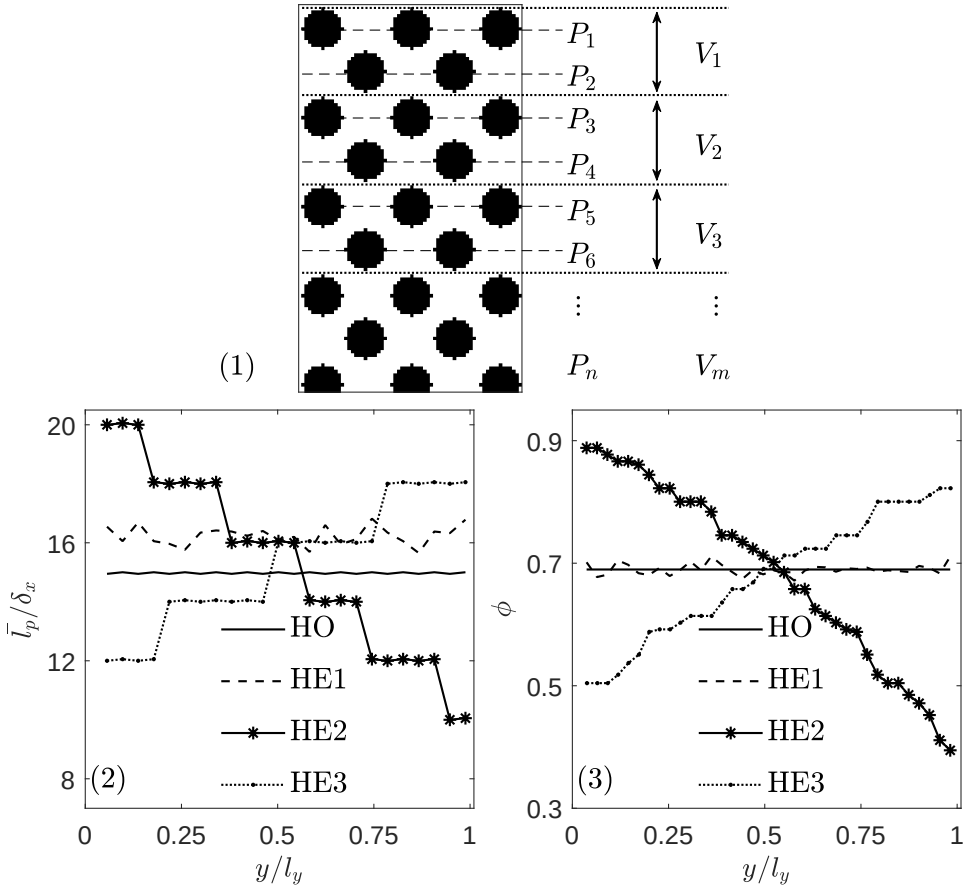

Figure 3.9 Measuring points P_n and volumes V_m based on the structure of medium HO (1). Vertical evolutions of horizontally averaged pore size $\overline{l_p}$ (2) and porosity ϕ (3) in both homogeneous and heterogeneous media.

Considering that fingering mainly develops along the y direction, the vertical change of horizontally averaged pore size $\overline{l_p}$ and porosity ϕ in both homogeneous and heterogeneous media are calculated. It is emphasized that the measuring positions P_n for $\overline{l_p}$ and volumes V_m for ϕ are identical in each medium and decided based on the porous structure of medium HO (see Fig. 3.9(1)). As illustrated in Figs. 3.9(2)-(3), both the calculated $\overline{l_p}$ and ϕ decrease (increase) monotonously in medium HE2 (HE3) along the flow direction, which is caused by the change of grain diameters. On the other hand, in media HO and HE1, results of

$\overline{l_p}$ and ϕ fluctuate around steady-state values. That is, along the y direction, ϕ remains constant as 0.69 in both media but $\overline{l_p}$ fluctuates around $15\delta_x$ and $16\delta_x$, respectively. The value of $\overline{l_p}$ in HE1 is slightly larger than that in HO due to the random porous structure.

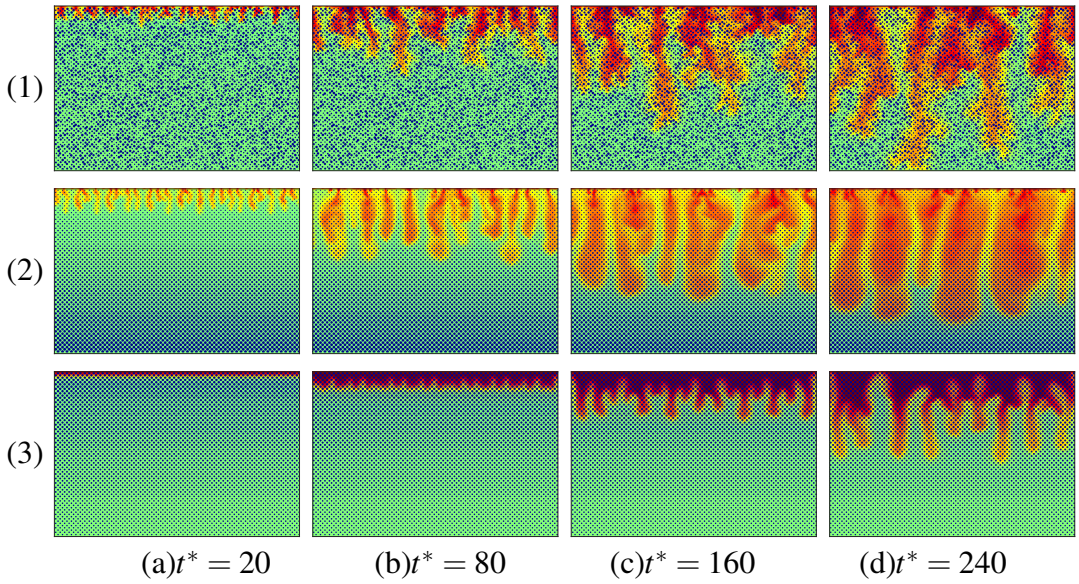

Figure 3.10 Contours of density fields ρ^* at four time instants $t^* = 20$ (a), 80 (b), 160 (c), and 240 (d), for Test R2 in heterogeneous media HE1 (1), HE2 (2), and HE3 (3).

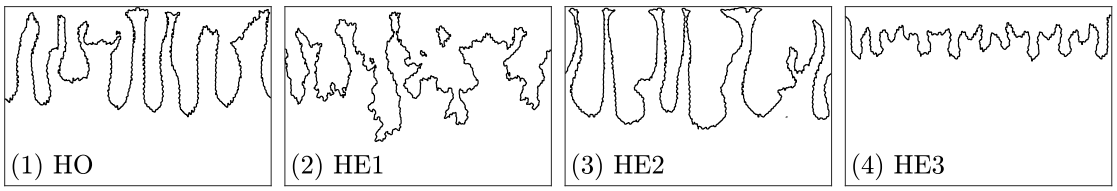

Figure 3.11 Outlines of density fingering at the time instant $t^* = 160$, for Test R2 in the homogeneous medium HO (1), heterogeneous media HE1 (2), HE2 (3), and HE3 (4).

With initial and boundary conditions being set as in Eqs. (3.4)-(3.5), simulation are performed in heterogeneous media. Similar to the above results in the homogeneous medium HO, six types of dissolution-driven density fingering with homogeneous reaction $A + B \rightarrow C$ are identified. As an example, Fig. 3.10 depicts density distributions in heterogeneous media for Test R2 (see Table 3.1). It is found that the development of density fingering in each heterogeneous medium experiences a similar set of periods as in

medium HO (Fig. 3.2(3)) but fingering development details are significantly influenced by the structure anisotropy. On one hand, in medium HE1, the large disorders of porous structure make some fingers grow rapidly and penetrate into the host fluid much deeper than the other fingers (Fig. 3.10(1)). Besides, in medium HE1, fingering tips are split regularly by the solid matrices (Fig. 3.10(1)) and the fingering interfaces become much rougher than that in HO (see outlines of density fingering in Fig. 3.11). On the other hand, in media HE2-HE3 with a regularly distributed matrix, fingering fronts show a relatively flat advancement and the fingering interface is smooth as in HO (Figs. 3.10(2)-(3) and 3.11). Compared with the homogeneous case HO (Fig. 3.2(3)) however, fingers are much thicker in HE2 (Fig. 3.10(2)) while much thinner in HE3 (Fig. 3.10(3)). This is introduced by vertical variations in pore spaces.

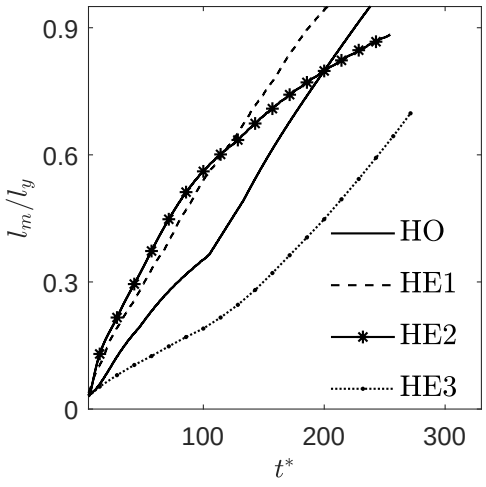

Figure 3.12 Temporal evolutions of fingering extension depth l_m for Test R2 in both homogeneous and heterogeneous media.

In addition to these various fingering shapes, differences in fingering propagation speed are observed from the calculated l_m in Fig. 3.12. In medium HE1, density fingering develops at a monotonic speed as in HO but the growing speed is much faster. It is reasonable since porosities ϕ of HO and HE1 are almost the same along the flow direction

(Fig. 3.9(3)) but the pore size $\overline{l_p}$ of HE1 is larger (Fig. 3.9(2)). This tendency suggests positive effects of the large pore size on the fingering growth. On the other side, in media HE2 and HE3, profiles of l_m exhibit two successive different velocities, which is different from the homogeneous case HO. This is also attributed to the change of pore size $\overline{l_p}$ and porosity ϕ along the flow direction (Figs. 3.9(2)-(3)). In HE2, the large pore bodies near the top boundary exert small resistance and thus lead to the fastest fingering growth among the four media during the early period. Due to the increasingly large resistance along the flow direction, the fast fingering development in HE1 is gradually suppressed and finally becomes slower than the homogeneous case HO. On the contrary, density fingering in HE3, with porosity being reversed to increase vertically, develops in a converse trend. Specifically, density fingering is weak and grows slowly at first, and then fingering is gradually intensified, and finally fingering becomes obvious and develops at a fast pace. Among the four cases, density fingering develops the slowest in HE3, even though the fingering growth speed increases in the later development period.

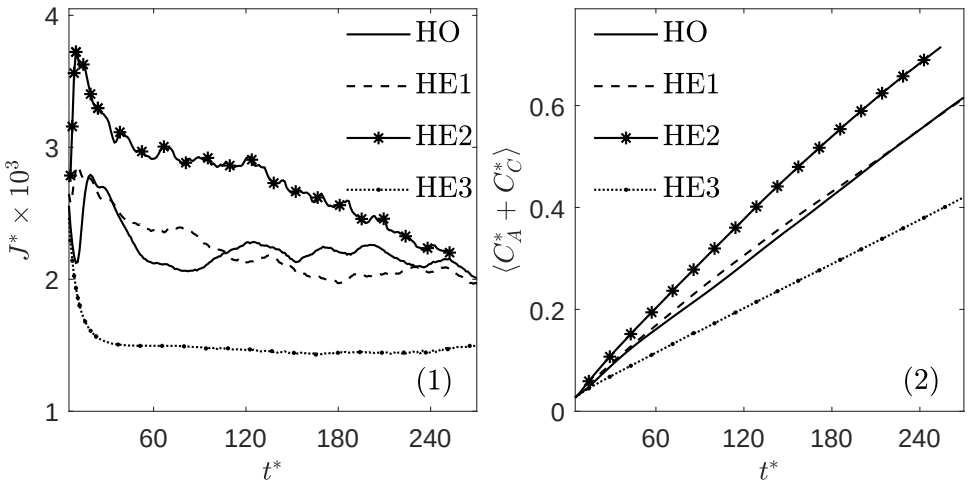

Figure 3.13 Temporal evolutions of horizontally averaged mass flux of A at the top boundary J^* (1) and stored amount of A in the host fluid $\langle C_A^* + C_C^* \rangle$ (2), for Test R2 in both homogeneous and heterogeneous media.

To quantify the impact of medium heterogeneity on the storage behaviours of A, results of metrics J^* and $\langle C_A^* + C_C^* \rangle$ are analyzed. Figure 3.13(1) firstly presents temporal evolutions of mass flux J^*. It is found that J^* fluctuates and finally collapses to a steady-state value in HE1, which is consistent with its homogeneous counterpart. This is introduced by their similar pore size $\overline{l_p}$ and porosity ϕ distributions along the flow direction (Figs. 3.9(2)-(3)). In media HE2 and HE3 however, curves of J^* deviate from the homogeneous case significantly. To be specific, in medium HE2, the curve of J^* initially shows a similar fashion as that in HO but keeps decreasing during the later development period, which is caused by the diminished pore spaces along the flow direction. In medium HE3, the profile of J^* also departs from the homogeneous case after the initial stage and it remains constant because of the significant suppression of porous structure on fingering development. Calculated curves of $\langle C_A^* + C_C^* \rangle$ are then plotted in Fig. 3.13(2). All these curves increase with time in a similar fashion, which is expected by Eq. (3.17). In addition, results of $\langle C_A^* + C_C^* \rangle$ are almost identical in media HO and HE1, suggesting these two media have a similar storage capacity of species A. Medium HE2 enhances the dissolution of A into the host fluid as both J^* and $\langle C_A^* + C_C^* \rangle$ become larger in HE2 than in HO.

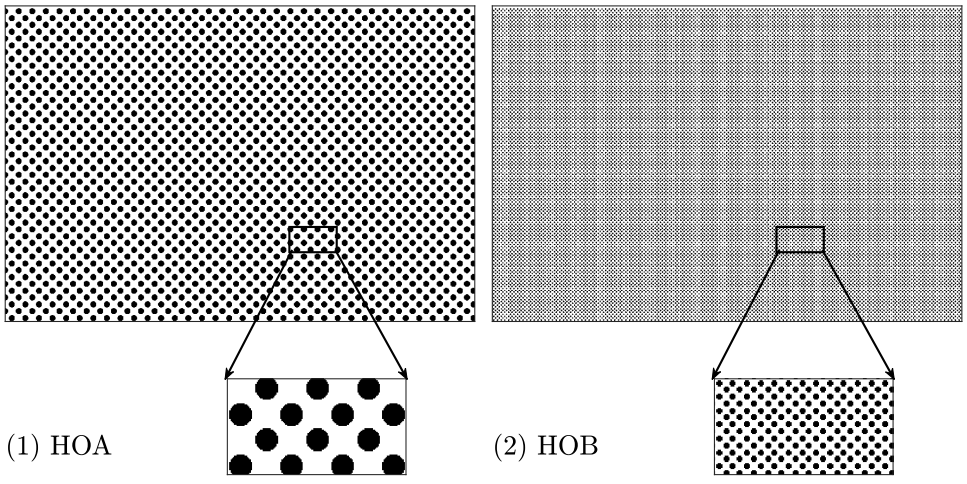

Figure 3.14 Schematic diagrams of homogeneous media HOA-HOB with different pore sizes.

The above results imply that, although the storage of A is almost identical in both HO and HE1, fingering growth speeds are different in these two media due to the different pore size distributions. Considering differences in pore size is not obvious in these two media, two homogeneous media HOA and HOB are generated as in Fig. 3.14 to further examine effects of pore size. Values of pore size for media HOA and HOB are selected as the largest ($24.4\delta_x$) and the smallest ($6\delta_x$) ones in medium HE1, respectively. In media HOA-HOB, solid grains obey a staggered distribution as in HO, and geometric parameters become, $d = 19\delta_x$, $r_x = r_y = 43.4\delta_x$, $l_p = 24.4\delta_x$ in HOA; and $d = 6\delta_x$, $r_x = r_y = 12\delta_x$, $l_p = 6\delta_x$ in HOB. The numbers of grains in these two media are different from that in HO, but their porosities and computational domains remain the same. In addition, similar to medium HE1, calculated ϕ keeps constant as 0.69 along the y direction in media HOA and HOB. However, results of $\overline{l_p}$ are different in these three media: curves of $\overline{l_p}$ fluctuate around $24.4\delta_x$ and $6\delta_x$ in HOA and HOB, respectively, while the curve of $\overline{l_p}$ for HE1 is bounded by these two profiles.

Based on media HOA-HOB, Test R2 is carried out and temporal evolutions of l_m, J^*, and $\langle C_A^* + C_C^* \rangle$ are compared with the corresponding results in HE1. As displayed in Fig. 3.15, among the three cases, fingering develops the fastest and the largest amount of species A is stored in HOA (with the largest pore size $24.4\delta_x$). Moreover, the simulated results in HE1 are bounded by those in media HOA and HOB, which is consistent with their vertical distributions of $\overline{l_p}$. These results verify that a medium with larger pore size is favourable for fingering development and storage of species A.

In summary, simulations have been conducted in three kinds of heterogeneous media. Similar to homogeneous cases in Sec. 3.2, results demonstrate reaction $A + B \rightarrow C$

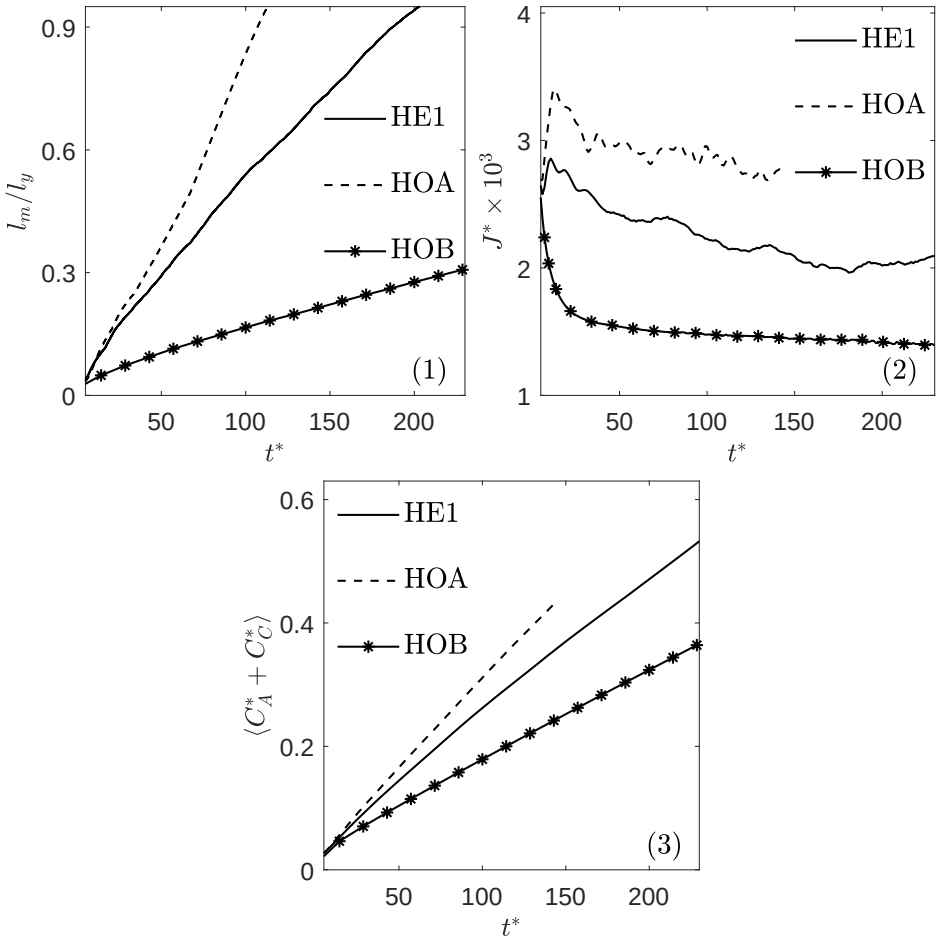

Figure 3.15 Temporal evolutions of fingering extension depth l_m (1), horizontally averaged mass flux of A at the top boundary J^* (2), and stored amount of A in the host fluid $\langle C_A^* + C_C^* \rangle$ (3), for Test R2 in homogeneous media HOA-HOB and heterogeneous medium HE1.

introduces six types of fingering scenarios. Besides, medium heterogeneity is found to influence the advancing position, shape, and propagation speed of density fingering. In terms of the storage efficiency of A, the calculated $\langle C_A^* + C_C^* \rangle$ and J^* indicate medium HE2 with large pore spaces in the top area is favourable.

3.5 Summary

Using the proposed MRT LB model in Sec. 2.1, this chapter conducts pore-scale simulations of dissolution-driven density fingering with homogeneous reaction $A + B \rightarrow C$ in both

homogeneous and heterogeneous porous media. One homogeneous medium and three heterogeneous media HE1-HE3 are artificially constructed, with HE1 containing randomly distributed solid grains while HE2-HE3 having vertically decreasing (HE2) or increasing (HE3) pore spaces. These media share the same porosity and computational domain.

Results in both homogeneous and heterogeneous media produce two non-reactive (NR and NRS) and four reactive (R1-R4) types of fingering scenarios and suggest reaction can enhance, inhibit, and trigger the development of density fingering. Then, a parametric study demonstrates that increasing $\Delta \mathrm{Ra}_{CB} = \mathrm{Ra}_C - \mathrm{Ra}_B$ (the relative contribution to fluid density of species C and B) introduces strong fingering and reaction, improves the storage of species A in the host fluid, and realizes the transition from stabilizing to destabilizing effects of reaction on the fingering development. In addition, increasing η or Da intensifies the impact of reaction on fingering but cannot modify how the reaction affects the fingering development. These results qualitatively confirm existing theoretical predictions and REV-scale simulations. They also provide new details of fingering development, including the later-stage non-linearities and the precise reaction intensity at the pore scale.

Effects of medium heterogeneity on fingering dynamics are analyzed at the pore scale. Compared with the homogeneous case, medium HE1 introduces obvious tip-splitting phenomena and rougher fingering interfaces; and media HE2-HE3 produce smooth but much thicker (HE2) or thinner (HE3) fingering. As for fingering growth speed, fingering develops the fastest in HE1 and the slowest in HE3. Besides, in medium HE2, fingering grows faster at early times but gradually becomes slower than the homogeneous case, which is caused by the decreased medium porosity along the flow direction. As for storage behaviors of species A, medium HE1 shows a similar capacity as the homogeneous one and

medium HE2 with large pore spaces near the top boundary introduces strong dissolution of *A* into the host fluid.

These pore-scale results have provided insights into dissolution-driven density fingering with homogeneous reaction and are important for industrial applications. For example, in the context of CO_2 sequestration, enhancing the dissolution of CO_2 is crucial to improving the storage efficiency and safety. The classified fingering types under effects of chemical reaction can provide a guidance for selecting geological storage sites according to their chemical compositions. Besides, effects of porous heterogeneity have highlighted the criterion that a medium with large pore size near the top layer is favorable.

CHAPTER 4 Differential diffusion effects on density fingering with homogeneous reaction

Dissolution-driven density fingering with homogeneous reaction $A + B \rightarrow C$ in porous media is closely related to some industrial applications, like geological sequestration of CO_2. Such a process has been simulated at the pore scale in Chapter 3 and six types of density fingering with reaction $A + B \rightarrow C$ have been produced and analyzed. In these simulations however, the three chemical species A, B, and C are assumed to diffuse equally. Recently, some theoretical analyses and REV-scale simulations have indicated that different diffusion coefficients between chemical species should be included to correctly interpret experimental data and appropriately guide engineering applications. These macroscopic studies have demonstrated that differential diffusion and chemical reaction can modify fluid concentration and density, thereby multiplying the types of dissolution-driven density fingering [71, 73, 84, 88]. Nevertheless, pore-scale descriptions of such a process is still missing. This chapter thus extends to model dissolution-driven density fingering in porous media at the pore scale, with effects of both homogeneous reaction $A + B \rightarrow C$ and differential diffusion being considered.

4.1 Problem description

Dissolution-driven density fingering between two reactive solutions 1 and 2 is investigated in a 2D homogeneous porous medium. The homogeneous medium constructed in Fig. 3.1 is applied here, with the porosity being $\phi = 0.69$ and the computational domain being $0 \leq x \leq$

$l_x = 1$ and $0 \leq y \leq l_y = 2/3$. In this medium, problem settings remain the same with those in Sec. 3.1. For brevity, more details concerning the problem description, governing equations, boundary and initial conditions, characteristic parameters, and boundary treatments are not repeated here and can be found in Sec. 3.1. The D2Q9 MRT LB model in Sec. 2.1 is further employed for pore-scale simulations of dissolution-driven density fingering coupled with homogeneous reaction $A + B \rightarrow C$ and differential diffusion.

This chapter focuses on the influence of reaction $A + B \rightarrow C$ and different diffusion coefficients of three chemical species, which are characterized by the buoyancy ratio $\mathrm{Ra}_B/\mathrm{Ra}_C$ and the diffusion ratio D_B/D_C, respectively [82]. Here $\mathrm{Ra}_B/\mathrm{Ra}_C$ describes the relative contributions to fluid density of solutes B and C and D_B/D_C quantifies the diffusion strengths of these two solutes. That is, $\mathrm{Ra}_B/\mathrm{Ra}_C > 1$ and $D_B/D_C > 1$ represent B is denser and diffuses faster than C. In the following simulations, the Schmidt number, Damköhler number, and initial concentration ratio are fixed as $\mathrm{Sc} = 100$, $\mathrm{Da} = 5$, and $\eta = 1$, respectively, and different values of Ra_r and D_r are selected to change test conditions. In addition, grid convergence tests have been carried out, and a mesh of size $N_x \times N_y = 1500 \times 1000$ is chosen to cover the computational domain in Fig. 3.1. Other geometrical parameters are set as, $d = 12\delta_x$, $r_x = 27\delta_x$, $r_y = 27\delta_x$, and $l_p = 15\delta_x$.

4.2 Fingering phenomena with reaction and differential diffusion

The general phenomena of dissolution-driven density fingering with impacts of homogeneous reaction $A + B \rightarrow C$ and differential diffusion are firstly investigated. To gain a comprehensive understanding, two Rayleigh numbers of species A ($\mathrm{Ra}_A = \pm 10^9$) are considered. Thus, density of the host fluid increases ($\mathrm{Ra}_A = 10^9$) or decreases ($\mathrm{Ra}_A = -10^9$)

upon the dissolution of A. These two tests are both simulated at different values of diffusion ratio D_B/D_C and a subsection of $\mathrm{Ra}_B/\mathrm{Ra}_C$ is modeled for each given D_B/D_C. In order to illustrate different scenarios of density fingering at the pore scale, obtained results are discussed from the following four groups: **Group I** with $\mathrm{Ra}_A = 10^9$, $D_B/D_C < 1$, and $\mathrm{Ra}_B/\mathrm{Ra}_C = 0.1 \sim 5$; **Group II** with $\mathrm{Ra}_A = 10^9$, $D_B/D_C > 1$, and $\mathrm{Ra}_B/\mathrm{Ra}_C = 0.1 \sim 5$; **Group III** with $\mathrm{Ra}_A = -10^9$, $D_B/D_C < 1$, and $\mathrm{Ra}_B/\mathrm{Ra}_C = 0.1 \sim 5$; and **Group IV** with $\mathrm{Ra}_A = -10^9$, $D_B/D_C > 1$, and $\mathrm{Ra}_B/\mathrm{Ra}_C = 0.1 \sim 5$. Results of eight typical cases P1-P8 are provided and discussed, with simulation parameters being provided in Table 4.1.

Table 4.1 Parameters for Cases P1-P8.

Cases	Parameters		
P1	$\mathrm{Ra}_A = 10^9$;	$D_B/D_C = 0.1$;	$\mathrm{Ra}_B/\mathrm{Ra}_C = 0.25$;
P2	$\mathrm{Ra}_A = 10^9$;	$D_B/D_C = 0.1$;	$\mathrm{Ra}_B/\mathrm{Ra}_C = 1.0$;
P3	$\mathrm{Ra}_A = 10^9$;	$D_B/D_C = 5.0$;	$\mathrm{Ra}_B/\mathrm{Ra}_C = 1.0$;
P4	$\mathrm{Ra}_A = 10^9$;	$D_B/D_C = 5.0$;	$\mathrm{Ra}_B/\mathrm{Ra}_C = 4.0$;
P5	$\mathrm{Ra}_A = -10^9$;	$D_B/D_C = 0.1$;	$\mathrm{Ra}_B/\mathrm{Ra}_C = 0.25$;
P6	$\mathrm{Ra}_A = -10^9$;	$D_B/D_C = 0.1$;	$\mathrm{Ra}_B/\mathrm{Ra}_C = 1.0$;
P7	$\mathrm{Ra}_A = -10^9$;	$D_B/D_C = 5.0$;	$\mathrm{Ra}_B/\mathrm{Ra}_C = 1.0$;
P8	$\mathrm{Ra}_A = -10^9$;	$D_B/D_C = 5.0$;	$\mathrm{Ra}_B/\mathrm{Ra}_C = 4.0$;

4.2.1 Density fingering in Group I with $\mathrm{Ra}_A = 10^9$ and $D_B/D_C < 1$

Simulations are firstly performed with $\mathrm{Ra}_A > 0$, $D_B/D_C < 1$, and various $\mathrm{Ra}_B/\mathrm{Ra}_C$. The development of density fingering is clearly observed in each test considered in this group. For a given D_B/D_C, two representative fingering patterns are identified depending on values of $\mathrm{Ra}_B/\mathrm{Ra}_C$. As an example, density evolutions of tests P1-P2 with $D_B/D_C = 0.1$, $\mathrm{Ra}_A = 10^9$, and $\mathrm{Ra}_B/\mathrm{Ra}_C = 0.25,\ 1$ are shown in Fig. 4.1. In case P1 with small $\mathrm{Ra}_B/\mathrm{Ra}_C = 0.25$, the initial fluid diffusion introduces a stratification of a denser fluid

layer L1 on top of a less dense one L2 (Fig. 4.1(1a)). Then, density fingering appears and experiences fingering growth, merge, and new fingering growth stages (Figs. 4.1(1b)-(1e)). The general fingering characteristics are similar to those of case R2 with three species diffusing at the same rate and more descriptions can be found in Chapter. 3.

With the increase of $\mathrm{Ra}_B/\mathrm{Ra}_C$, the other fingering pattern develops, like in case P2 with $\mathrm{Ra}_B/\mathrm{Ra}_C = 1$. Compared with case P1, the early diffusion introduces a different density stratification containing four layers: a denser fluid layer L1 near the top boundary overlies a local minimum density layer L2, and the following denser layer L3 is on top of a less dense one L4 (Fig. 4.1(2a)). Correspondingly, the density curve at $t^* = 30$ in Fig. 4.1(2f) has a local minimum followed by a local maximum. Layers L2 and L3 are introduced by the different diffusion rates between B and C, which is referred to as the diffusive-layer convection (DLC) mechanism [85]. To be specific, species A reacts with B to yield C at the reaction front (RF), where the largest reaction rate takes place and two reactants are almost consumed. So, less A and B penetrate RF and fast-diffusion C overlies slow-diffusion B ($D_B/D_C < 1$) (Fig. 4.2(b)). Considering C diffuses downwards from RF without being fully replaced by B, a local species-depleted (SD) and a local species-rich (SR) areas are subsequently generated at and below RF, respectively (Fig. 4.2(b)). In this case with $\mathrm{Ra}_B/\mathrm{Ra}_C = 1$, species C is not dense enough to change the fluid density distribution and thus a local minimum (L2) and a local maximum (L3) density layers develop at SD and SR, respectively (Fig. 4.2(b)).

These initial fluid layers form two buoyantly unstable stratifications: L1-L2 and L3-L4. After the short diffusion period, the first density fingering develops from L1 near the top boundary (Fig. 4.1(2b)), which corresponds to the unstable stratification L1-L2. This

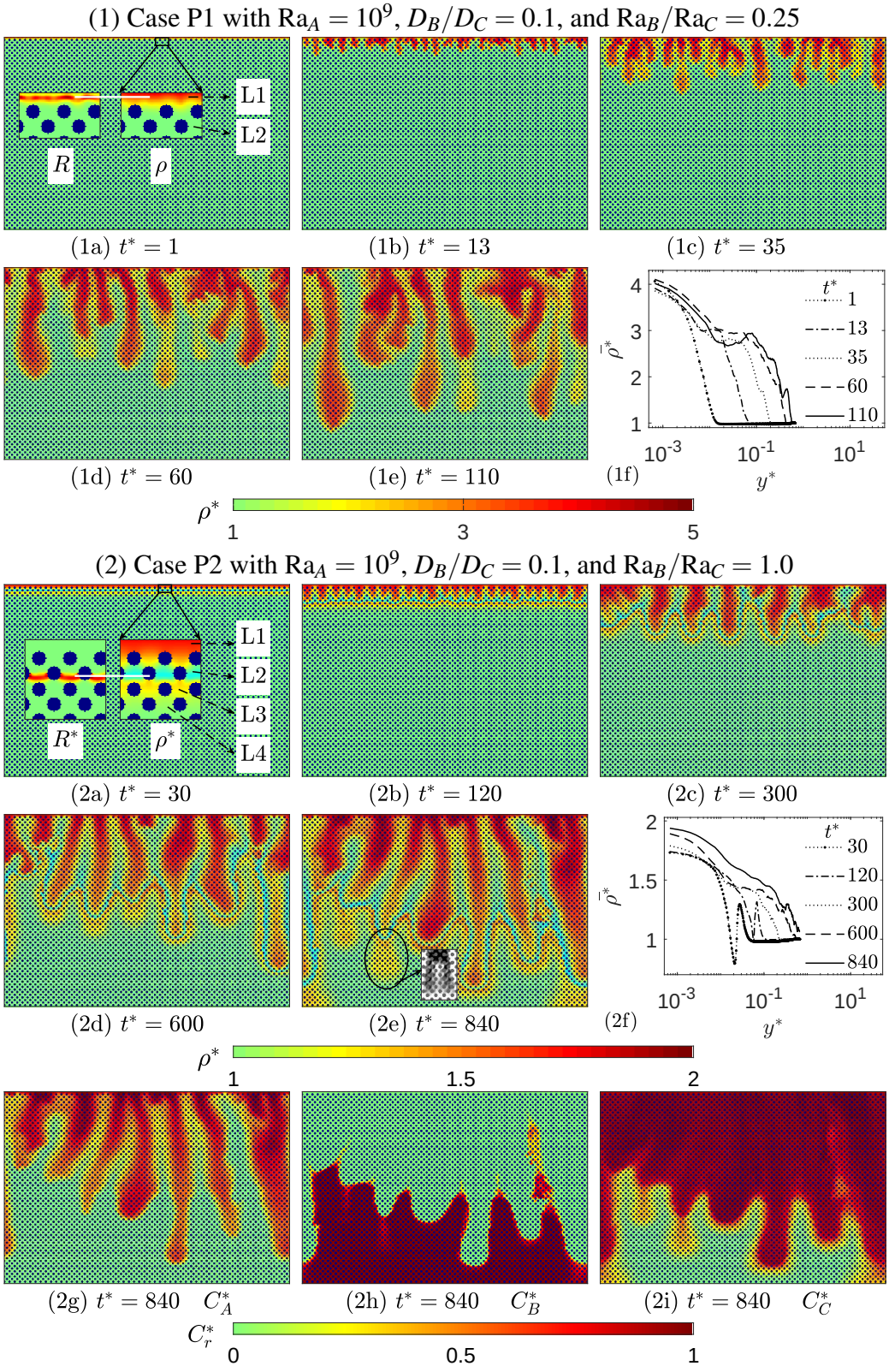

Figure 4.1 Contours of density fields ρ^* (a)-(e) and horizontally averaged density $\overline{\rho}^*$ (f) at five time instants t^*, for Cases P1-P2 with $Ra_A = 10^9$, $D_B/D_C = 0.1$, and $Ra_B/Ra_C = 0.25$ (1), 1.0 (2). Contours of species concentrations fields (2g)-(2i) at time instant $t^* = 840$ for case P2.

first fingering grows and experiences classical fingering merge and new fingering growth, but without penetrating the minimum density layer L2 (Figs. 4.1(2c)-(2e)). Compared with case P1, the development of the first fingering is slowed down by the local stable stratification L2-L3. During the late period, the second density fingering starts from L3 and gradually becomes visible (Fig. 4.1(2d)), which is triggered by the unstable stratification L3-L4. The two fingering areas are separated by L2. In contrast to fingers of the first density fingering area, fingers of the second fingering area tend to grow individually or form antenna-shaped patterns (Fig. 4.1(2e)), which can be explained by the fast-diffusion C in L3 [86]. The concentration fields in Figs. 4.1(2g)-(2i) corresponding to the density field in Fig. 4.1(2e) verifies that species C contributes to the second density fingering and the division of secondary fingers, while the first fingering is caused by fingers of A. Considering L2 and L3 are mainly introduced by the DLC mechanism, the specific fingering phenomenon in this case is defined as DLC-type density fingering.

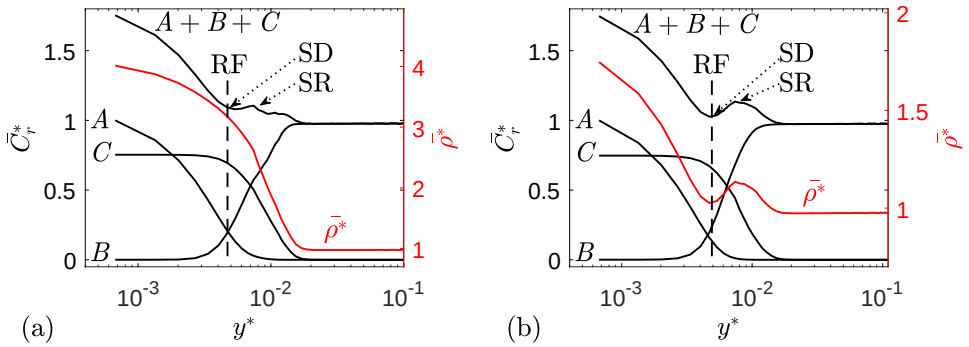

Figure 4.2 Horizontally averaged density $\overline{\rho}^*$ and concentration $\overline{C}_r^*$ at time instance $t^* = 24$, for Cases P1-P2 with $\mathrm{Ra}_A = 10^9$, $D_B/D_C = 0.1$, and $\mathrm{Ra}_B/\mathrm{Ra}_C = 0.25$ (a), 1.0 (b).

During the early diffusion stage of case P1, DLC also introduces similar species distribution as in P2 (Fig. 4.2). But product C is dense enough to modify the density field and generate a vertically decreasing one. Thus, density fingering wins in deforming the buoyantly unstable layer quickly and C sinks into the host fluid before it diffuses to form

layers L2 and L3. This also explains the weaker SD and SR areas in case P1 compared with those in P2. Considering product C enlarges the density difference between L1 and L2 and promote the development of density fingering as reported in Chapter 3, density fingering in P1 is defined as reaction-enhanced (RE) one.

The contribution amplitude of C to density decreases with increasing $\mathrm{Ra}_B/\mathrm{Ra}_C$ and the system switches from RE-type (P1) to DLC-type (P2) fingering at $\mathrm{Ra}_B/\mathrm{Ra}_{C_s}$. The obtained threshold for $D_B/D_C = 0.1$ is $\mathrm{Ra}_B/\mathrm{Ra}_{C_s} \approx 0.3$ and this critical value increases with D_B/D_C. In addition, calculated horizontally averaged density profiles keep decreasing monotonically along the y direction in P1 (Fig. 4.1(1f)), but transfer from a non-monotonically pattern into a monotonically decreasing one in P2 (Fig. 4.1(2f)). It is emphasized that, although the local minimum and maximum layers exist in case P2 (Fig. 4.1(2)), the averaged density curve decreases monotonically at later times. This is because the development of density fingering brings in large disorders to deform the minimum and maximum layers.

4.2.2 Density fingering in Group II with $\mathbf{Ra}_A = 10^9$ and $D_B/D_C > 1$

Fingering phenomena for $D_B/D_C > 1$ and $\mathrm{Ra}_A > 0$ at different $\mathrm{Ra}_B/\mathrm{Ra}_C$ are then simulated. Similarly, a part of the results are provided in Fig. 4.3 to illustrate two typical fingering scenarios in this group. Initial density fields in Figs. 4.3(1a) and (2a) display two similar stratifications: a denser fluid layer L1 lies above a local minimum density layer L2 on top of a layer L3. But L2 is located above (case P3) or at (case P4) RF, depending on the value of $\mathrm{Ra}_B/\mathrm{Ra}_C$. The formation of these two initial stratifications is attributed to another differential diffusion effect, namely, the double-diffusive (DD) mechanism [85]. As mentioned in group I, product C locates above B upon reaction. Thus, in both P3 and P4 with $D_B/D_C > 1$, the fast upward diffusion of B and the slow downward diffusion of C

contribute to the generation of a local SD area below RF (Fig. 4.4). Note that, although fast-diffusion B promotes the accumulation of C above RF by reaction $A + B \rightarrow C$, no local SR region exists. It is because the dissolution of A makes the SR layer located at the top boundary. Under this similar species distribution, two different density fields built up based on the contribution to fluid density of C. In case P3 with small $\mathrm{Ra}_B/\mathrm{Ra}_C$ (Fig. 4.3(1a)), C increases fluid density sufficiently as in P1. Thus, layer L2 with local minimum density develops below RF and more specifically at SD, where less C presents. On the other hand, in case P4 with large $\mathrm{Ra}_B/\mathrm{Ra}_C$ (Fig. 4.3(2a)), L2 locates at RF since C is not dense enough to compensate the consumption of B. Correspondingly, the initial density curves in Fig. 4.4 clearly illustrate a minimum below RF in P3 and at RF in P4.

After the initial diffusion stage, dense fingers sink from L1 towards the host fluid in both cases and fingering tips are located above L2 at first (Figs. 4.3(1b)-(2b)). Then, two types of density fingering are observed during fingering merge and new fingering stages. First, in case P3 with low $\mathrm{Ra}_B/\mathrm{Ra}_C$ (Figs. 4.3(1c)-(1e)), fingering tips progressively penetrate L2, with fingers being larger above L2 but narrower below. This is caused by the fact that L2 and L3 form a buoyantly stable stratification to hinder the progression of fingers into the host fluid. In case P3 however, species C is sufficiently dense and thus the the strength of the barrier L2-L3 is too weak to counteract fingering progression. Concentration distributions in Figs. 4.3(1g)-(1i) corresponding to the density field in Fig. 4.3(1e) also expresses that a small part of C penetrates L2 to yield narrow fingers below, while fingers of A play a vital role in forming wide fingers above. It is emphasized that, in case P3, the minimum layer L2 at SD is introduced by the DD mechanism, thus the fingering in this case is defined as DD-type density fingering. Second, in case P4 with

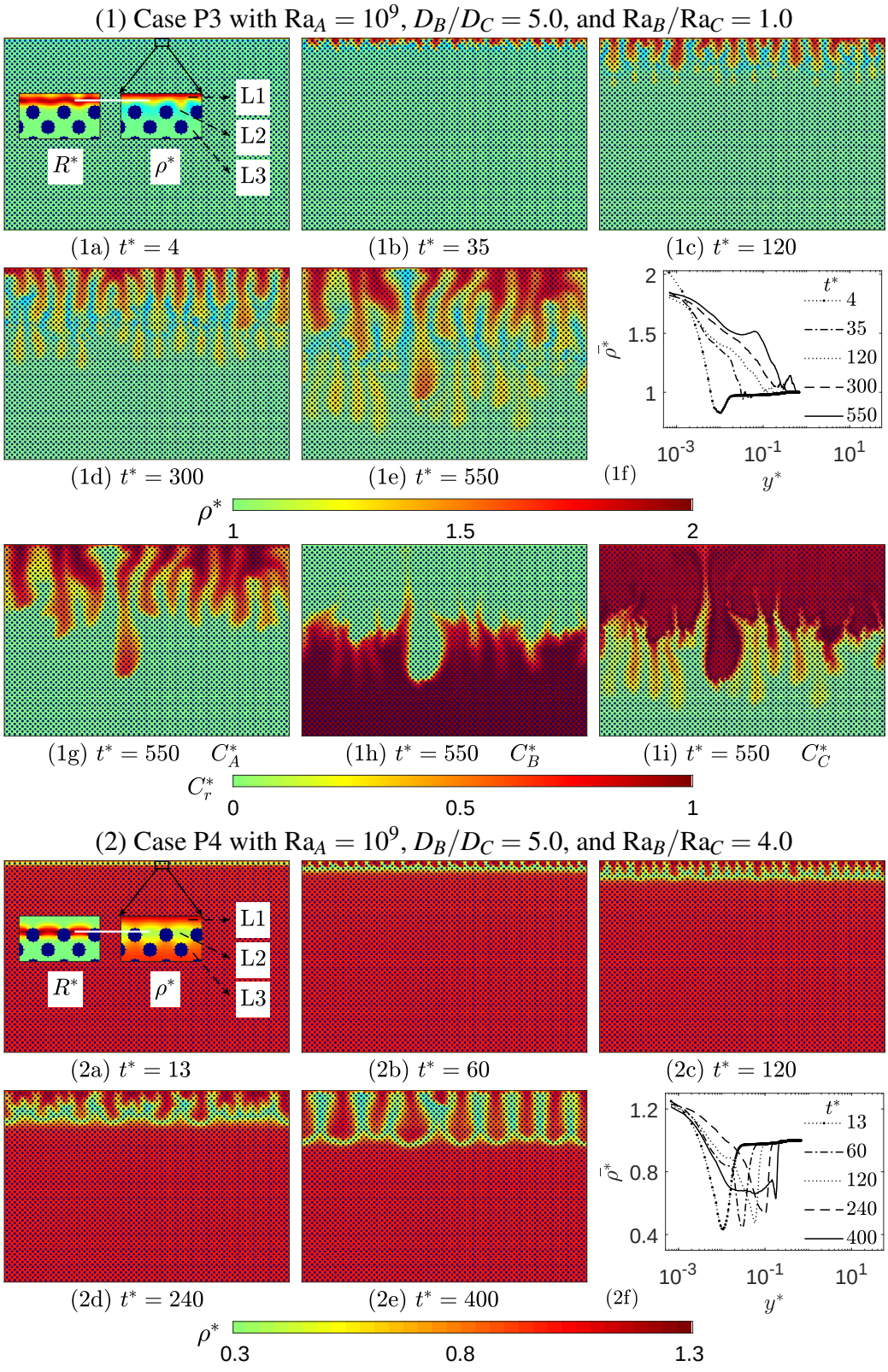

Figure 4.3 Contours of density fields ρ^* (a)-(e) and horizontally averaged density $\overline{\rho}^*$ (f) at five time instants t^*, for Cases P3-P4 with $Ra_A = 10^9$, $D_B/D_C = 5.0$, and $Ra_B/Ra_C = 1.0$ (1), 4.0 (2). Contours of species concentrations fields (1g)-(1i) at time instant $t^* = 550$ for case P3.

high $\mathrm{Ra}_B/\mathrm{Ra}_C$ (Fig. 4.3(2)), the downward movement of density fingering is efficiently refrained by L2. This is because product C is not dense enough to penetrate the stabilizing barrier of L2-L3. The development of density fingering agrees well with the equal diffusion case R1 in Chapter 3 and L2 at RF is mainly caused by reaction. Thus the development of fingering in P4 is classified as reaction-suppressed (RS) one.

Note that, the horizontally averaged density profiles remain non-monotonic (with a local minimum) in P4 (Fig. 4.3(2f)) but switches from a non-monotonic pattern to a monotonically decreasing one in P3 (Fig. 4.3(1f)). The most likely explanation for this difference is that the strong DD-type density fingering finally penetrates L2 and introduces obvious non-linearities in P3. Besides, the system transfers from DD-type to RS-type density fingering at $\mathrm{Ra}_B/\mathrm{Ra}_{C_s} \approx 2.5$ for $D_B/D_C = 5.0$ and this critical value increases with D_B/D_C.

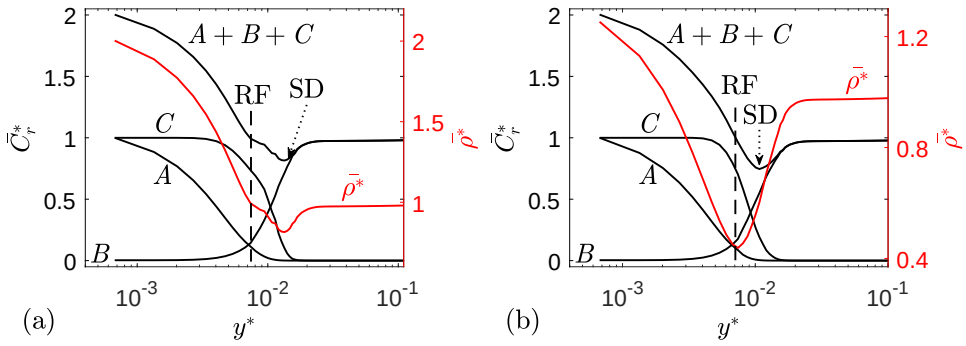

Figure 4.4 Horizontally averaged density $\overline{\rho}^*$ and concentration $\overline{C}_r^*$ at time instance $t^* = 6$, for Cases P3-P4 with $\mathrm{Ra}_A = 10^9$, $D_B/D_C = 5.0$, and $\mathrm{Ra}_B/\mathrm{Ra}_C = 1.0$ (1), 4.0 (2).

4.2.3 Density fingering in Group III with $\mathrm{Ra}_A = -10^9$ and $D_B/D_C < 1$

Based on simulation results obtained in this group, two types of fingering phenomena are defined. For illustration, density evolutions at $D_B/D_C = 0.1$, $\mathrm{Ra}_A = -10^9$, and $\mathrm{Ra}_B/\mathrm{Ra}_C = 0.25,\ 1$ are provided in Fig. 4.5. Similar to Group II, initial diffusion introduces two density

stratifications: a less dense fluid layer L1 lies above a local maximum density layer L2 at (case P5) or below (case P6) RF, and these two layers are followed by a layer L3 (Figs. 4.5(1a)-(2a)). Similar to group I, the DLC mechanism comes into play here and a local SD and a local SR areas form at and below RF, respectively (Fig. 4.6). Nevertheless, considering species A contributes to decreasing the fluid density, density fields formed in this group are different from those in group I. On one hand, in case P5 with relatively small $\mathrm{Ra}_B/\mathrm{Ra}_C$ (Fig. 4.5(1a)), the local maximum density layer L2 forms at RF, where less A and more C exist (Fig. 4.6(a)). This is because fluid density decreases with the dissolution of A but increases with the production of C. On the other hand, in case P6 with high $\mathrm{Ra}_B/\mathrm{Ra}_C$ (Fig. 4.5(2a)), the contribution to fluid density of C decreases but that of A remains the same. Thus, L2 develops below RF and specifically at SR, where almost all of A is consumed by reaction (Fig. 4.6(b)). Note that, no local minimum density layer appears corresponding to the local SD area in this group. This is attributed to the fact that dissolved A decreases fluid density and introduces a minimum density layer at the top boundary. Initial density curves in Fig. 4.6 quantitatively display positions of minimum and maximum density layers in both cases and indicate the unstable density jump between L2 and L3 is larger in P5 than in P6.

Dense fingers then develop from L2 and progress down into the host fluid. Fingering merge and new fingering growth are observed in both cases P5 and P6 (Figs. 4.5(b)-e). Due to different intensities of the unstable density jump from L2 to L3, two fingering scenarios are observed. First, in case P5 with relatively small $\mathrm{Ra}_B/\mathrm{Ra}_C$, the dense species C magnifies the unstable density gradient and subsequently brings in strong fingering. The fingering development in case P5 is similar to that in case R3 (Chapter 3) and is defined as

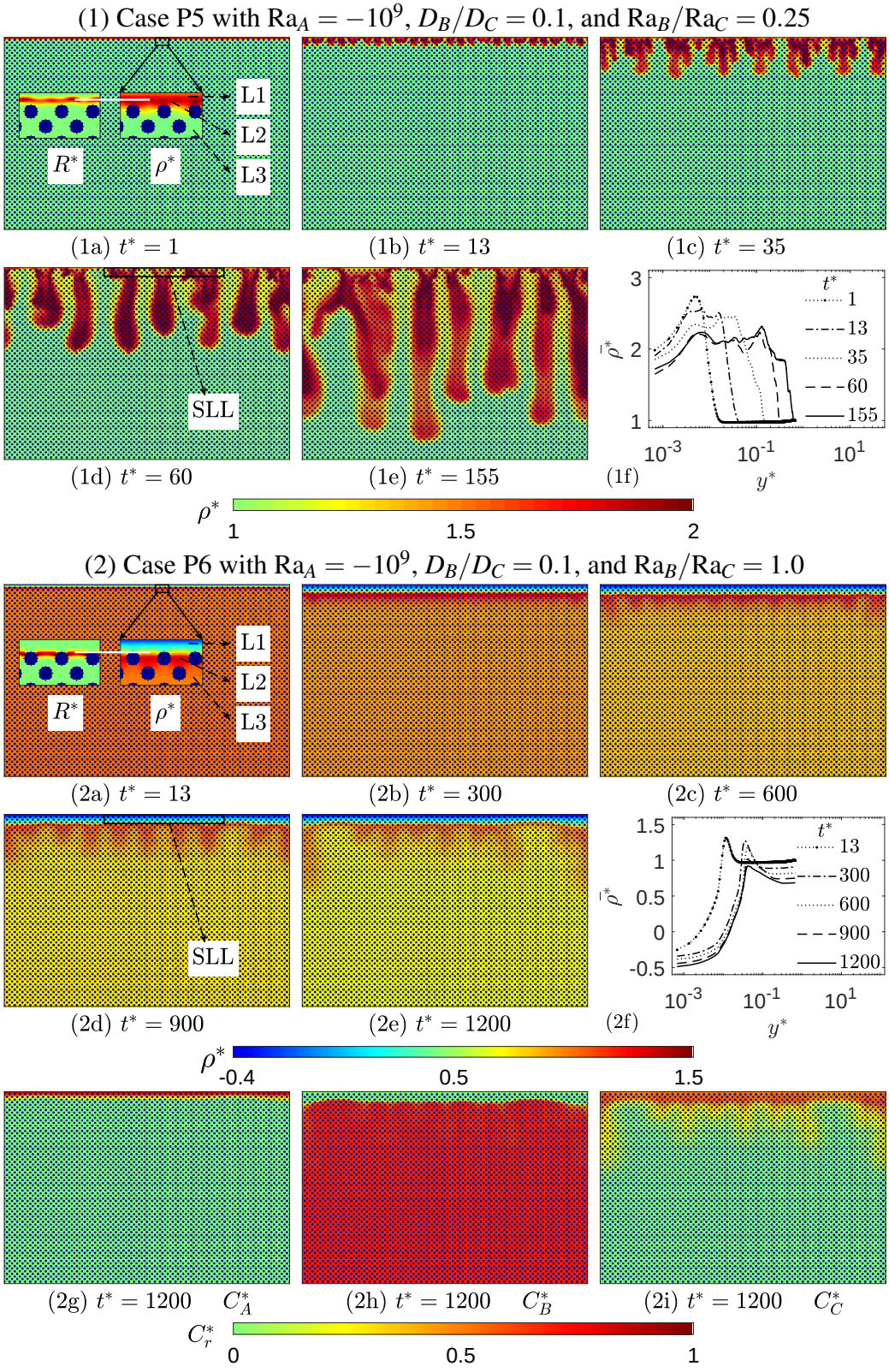

Figure 4.5 Contours of density fields ρ^* (a)-(e) and horizontally averaged density $\overline{\rho}^*$ (f) at five time instants t^*, for Cases P5-P6 with $\mathrm{Ra}_A = -10^9$, $D_B/D_C = 0.1$, and $\mathrm{Ra}_B/\mathrm{Ra}_C = 0.25$ (1), 1.0 (2). Contours of species concentrations fields (2g)-(2i) at time instant $t^* = 1200$ for case P6.

reaction-introduced (RI) density fingering. It is because L2 at RF is introduced by chemical reaction and density fingering is not observed in the non-reactive counterpart. Second, in case P6 with large $\mathrm{Ra}_B/\mathrm{Ra}_C$, fingering grows slowly and gradually becomes weak. This is related to the fact that the density difference between L2 and L3 is too weak to deform the fluid interface quickly. Thus species A and B tend to diffuse to meet and react with each other, making the concentration of B in the host fluid diluted gradually. This is verified by the relatively flat fluid interfaces in concentration fields of A and B (Figs. 4.5(2g)-(2h)), as well as the decreased host fluid density (Fig. 4.5(2f)). As time goes on, the concentration of B decreases and its upward diffusion slows down, which causes the descending production rate of C. Seen from concentration fields in Figs. 4.5(2g)-(2i), fingers of C are responsible for the development of density fingering. Thus, the decreased production of C ultimately results in the weak density fingering. The slow fingering development in P6 is called DLC-type density fingering since the DLC mechanism brings in the unstable stratification L2-L3.

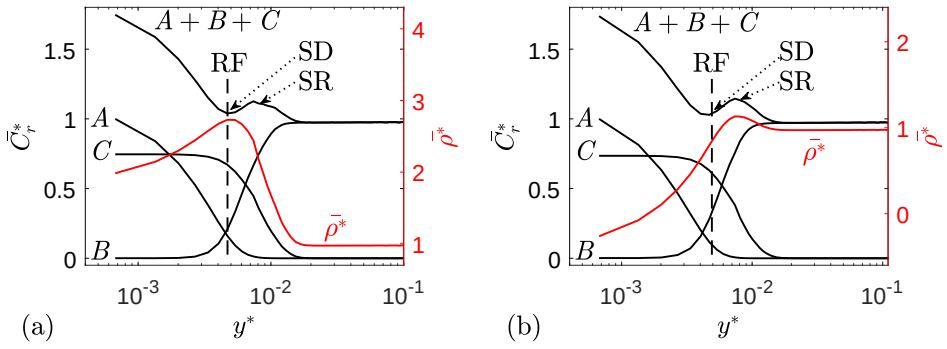

Figure 4.6 Horizontally averaged density $\overline{\rho}^*$ and concentration $\overline{C}_r^*$ at time instance $t^* = 6$, for Cases P5-P6 with $\mathrm{Ra}_A = -10^9$, $D_B/D_C = 0.1$, and $\mathrm{Ra}_B/\mathrm{Ra}_C = 0.25$ (a), 1.0 (b).

It is important to stress the characteristic base shape in these two cases, namely, the stagnant liquid layer (SLL) near the top boundary (Figs. 4.5(1d)-(2d)). The remaining A after reaction in the top layer decreases fluid density and is at the origin of SLL (Figs. 4.5(2g)),

which is not observed in cases with $\mathrm{Ra}_A > 0$. Seen from Figs. 4.5(1d)-(2d), SLL is weak and distributes in separated parts in P5, but it becomes thick and spans the entire domain width in P6. This is reasonable as species transport by convection is orders of magnitude larger than by diffusion. Specifically, in case P5, the well-developed density fingering is accompanied by strong convection and thus brings B up to react with A near the top boundary quickly. However, in case P6, reactants A and B come into contact and react by diffusion, which is slow. Consequently, A is consumed efficiently in P5 but tends to accumulate near the top boundary in P6. Again, in this group, a switch threshold $\mathrm{Ra}_B/\mathrm{Ra}_{C_s} \approx 0.3$ is identified for the RI-type and DLC-type density fingering at $D_B/D_C = 1.0$, and $\mathrm{Ra}_B/\mathrm{Ra}_{C_s}$ ascends with D_B/D_C. In terms of the horizontally averaged density profiles in Figs. 4.5(1f)-(2f), the late-stage profiles keep being non-monotonic with a local maximum. This is because the dissolution of A decreases fluid density obviously at the top boundary.

4.2.4 Density fingering in Group IV with $\mathrm{Ra}_A = -10^9$ and $D_B/D_C > 1$

Finally, two specific fingering scenarios are observed after simulations in this group. They are illustrated with the help of results at $D_B/D_C = 5$, $\mathrm{Ra}_A = -10^9$, and $\mathrm{Ra}_B/\mathrm{Ra}_C = 1.0,\ 4.0$ in Fig. 4.7. On one hand, at low $\mathrm{Ra}_B/\mathrm{Ra}_C$ (case P7 in Fig. 4.7(1)), initial diffusion introduces a density stratification containing four layers: layer L1 lies on top of a local maximum density layer L2 and the following layer L3 with local minimum density overlies layer L4 (Fig. 4.7(1a)). The DD mechanism, as introduced in group II, brings in a SD area below RF here (Fig. 4.8(a)), but the decrease of fluid density upon the dissolution of A leads to a different density distribution. That is, similar to case P5, the sufficiently dense C results in a local maximum (L2) at RF and a local minimum (L3) at SD. Only one unstable stratification is formed by L2 and L3 in this case. Thus, density fingering

develops from L2 and experiences fingering growth, merge, and new fingering growth periods (Figs. 4.7(1b)-(1e)). Even DD-induced L3 forms a buoyantly stable stratification with L4, fingering tips can penetrate this weak barrier as in case P3. It is emphasized that, after penetration, fingering becomes strong below L3 as species A decreases fluid density obviously in the top layer. In addition, similar to case P6, fingering grows slowly with the decreased B in the host fluid and SLL caused by remaining A near the top boundary is also observed. Considering the unstable stratification L2-L3 is caused by the DD mechanism, fingering phenomenon in this case is defined as DD-type density fingering.

As for density curves in Fig. 4.7(1f), they initially show a non-monotonic pattern with a maximum followed by a minimum, which is consistent with the density field in Fig. 4.7(1a). But as propagation goes on, the density curve changes in a non-monotonic fashion with only a local maximum and the disappearance of the local minimum density is caused by the penetration of fingering tips as in case P3. In addition, the local maximum density decreases with time because of the dilution of B as in case P6.

On the other hand, at high $\mathrm{Ra}_B/\mathrm{Ra}_C$ (case P8 in Fig. 4.7(2)), initial diffusion introduces a buoyantly stable stratification of a less dense layer L1 on top of a denser layer L2 (Fig. 4.7(2a)). Under this condition, the horizontally averaged density profile at each time instant increases monotonically and no fingering develops (Fig. 4.7(2)). Again, a critical value $\mathrm{Ra}_B/\mathrm{Ra}_{C_s} \approx 2.5$ is captured between cases P7 and P8 for $D_B/D_C = 5.0$ and this critical value increases with D_B/D_C.

To summarize, effects of D_B/D_C and $\mathrm{Ra}_B/\mathrm{Ra}_C$ on the development of density fingering are classified into eight regimes, as shown in Fig. 4.9. For cases P1-P4 with $\mathrm{Ra}_A > 0$, denser fluid rich in A grows from the top boundary and fingering develops from the top layer.

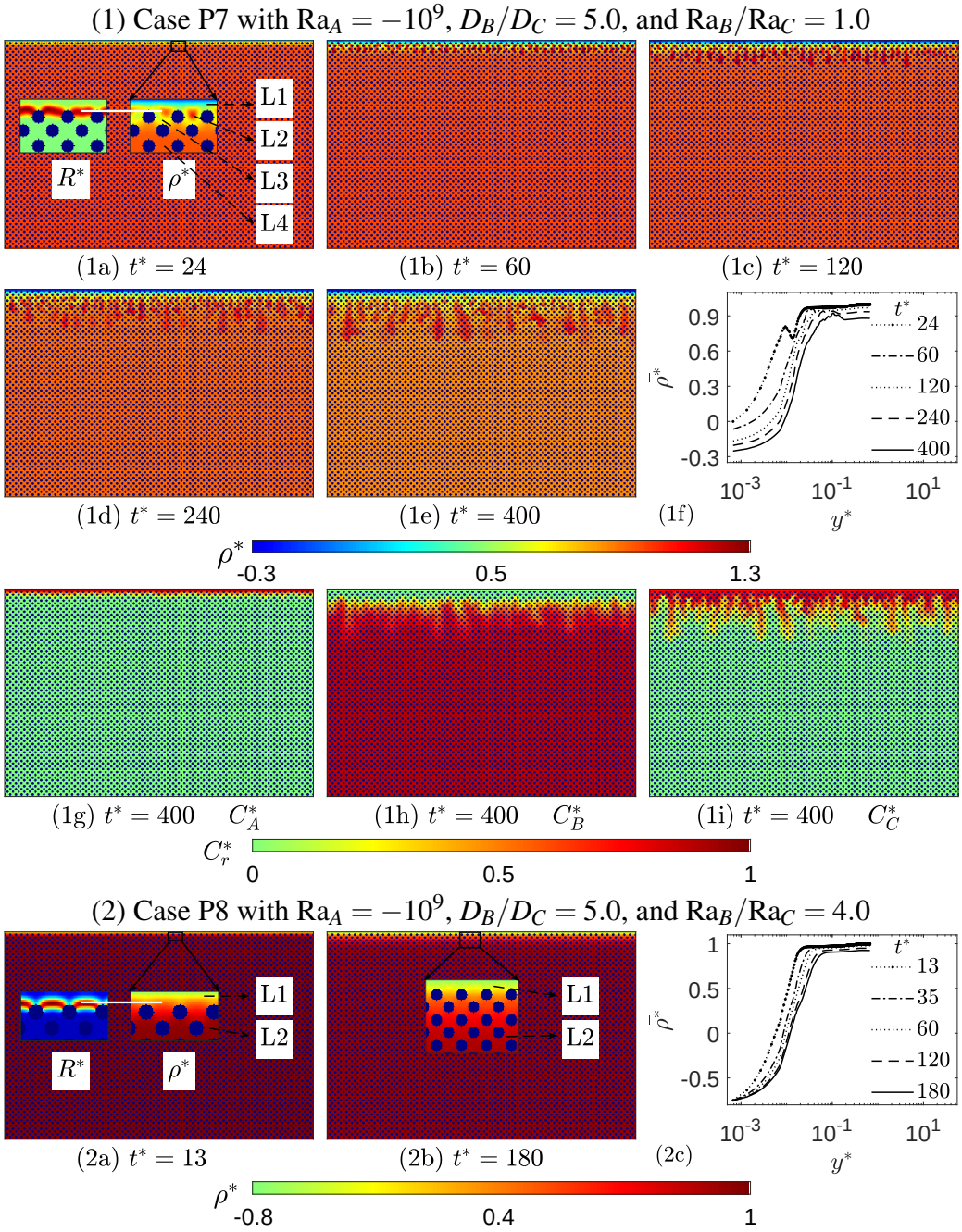

Figure 4.7 Contours of density fields ρ^* (a)-(e) and horizontally averaged density $\overline{\rho}^*$ (f) at five time instants t^*, for Cases P7-P8 with $Ra_A = -10^9$, $D_B/D_C = 5.0$, and $Ra_B/Ra_C = 1.0$ (1), 4.0 (2). Contours of species concentration fields (1g)-(1i) at time instant $t^* = 400$ for case P7.

Therefore, regardless of reaction or differential diffusion, the system is buoyantly unstable. Then, according to relative values of Ra_B/Ra_C and D_B/D_C, four different fingering patterns are classified as RE, DLC, DD and RS. On the other hand, for cases P5-P8 with $Ra_A < 0$, fluid density decreases upon the dissolution of A and the system keeps stable near the

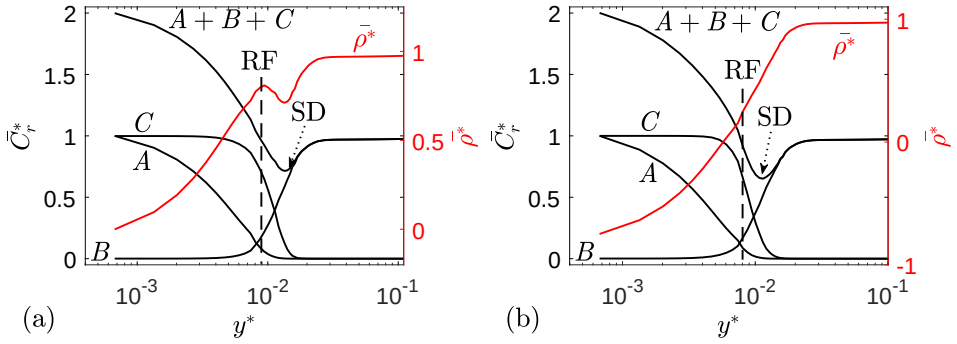

Figure 4.8 Horizontally averaged density $\overline{\rho}^*$ and concentration $\overline{C}_r^*$ at time instance $t^* = 6$, for Cases P7-P8 with $\mathrm{Ra}_A = -10^9$, $D_B/D_C = 5.0$, and $\mathrm{Ra}_B/\mathrm{Ra}_C = 0.25$ (a), 1.0 (b).

top boundary. In addition, density fingering only develops below the SLL layer that is introduced by remaining A near the top boundary. Similarly, four cases P5-P8 are identified depending on $\mathrm{Ra}_B/\mathrm{Ra}_C$ and D_B/D_C as RI, DLC, DD and stable.

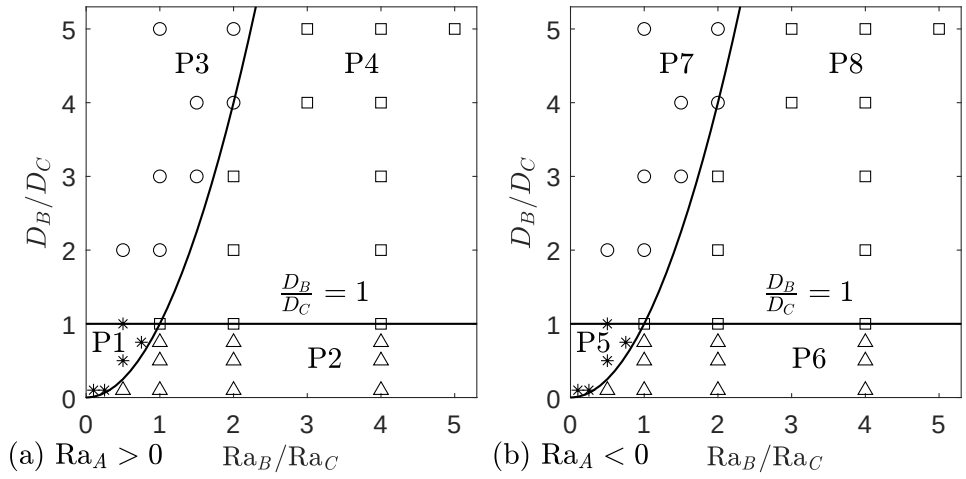

Figure 4.9 Plots of dissolution-driven density fingering simulation cases (black symbols) in a phase plane spanned by parameters D_B/D_C and $\mathrm{Ra}_B/\mathrm{Ra}_C$. Eight distinct areas are divided to represent eight regimes of density fingering development.

The present classification is generally consistent with theoretical results in [82] and calculated horizontally averaged density profiles also verify theoretical predictions in the early period: monotonically decreasing (P1) or increasing (P8), with one minimum below (P3) or at (P4) RF, with one maximum at (P5) or below (P6) RF, with a minimum followed by a maximum (P2) or the opposite (P7). As fingering comes into the late non-linear

stage however, density profiles in these eight cases are divided into two parts. On one hand, density curves remain the same as their initial patterns in cases P1, P4, P5 and P8. Fingering dynamics in these four cases are consistent with those in equal-diffusion cases R1-R4 (Chapter 3), where fingering properties are dominated by chemical reaction. On the other hand, when differential diffusion effects become obvious in cases P2, P3, P6 and P7, averaged density curves tend to decrease monotonically (P2, P3) or increase non-monotonically with a local maximum (P6, P7). In these four cases, the DD and DLC mechanisms introduce new fingering features not observed in Chapter 3. Specifically, the DLC-induced maximum density layer brings in the second density fingering area in P2; the DD-induced minimum density layer is penetrated by fingering tips in P3; and the DD and DLC mechanisms trigger fingering phenomena in cases P6 and P7. It is emphasized that, species distributions are captured to show local SD and SR areas and then to clearly identify positions of local minimum and maximum density layers.

4.3 Quantitative effects of differential diffusion

Having investigated the general phenomena of density fingering under different values of D_B/D_C and $\mathrm{Ra}_B/\mathrm{Ra}_C$, quantitative effects of these two parameters are further explored. Now that, pore-scale simulations in Chapter 3 with $D_A = D_B = D_C$ have proven that increasing $\mathrm{Ra}_B/\mathrm{Ra}_C$ destabilizes density fingering, this parameter is thus no longer analyzed here. To focus on differential diffusion effects, all species are assumed to contribute equally to fluid density, namely, $\mathrm{Ra}_A = \mathrm{Ra}_B = \mathrm{Ra}_C = 10^9$. Besides, the diffusion rate of B is fixed as $D_B = D_A$ and different values of D_C are selected to change D_B/D_C.

Effects of differential diffusion on the progression of density fingering are firstly evaluated by calculating the fingering extension depth l_m. Temporal evolutions of l_m in Fig. 4.10 show that l_m increases with decreasing D_B/D_C during the early diffusion stage. This is because, under the smaller D_B/D_C, the diffusion rate of C becomes larger and the top fluid layer rich in A and C progresses into the host fluid faster, leading to the larger l_m. After this short period, l_m starts to increase with time rapidly, which is introduced by the onset of fingering. It is found that, in tests with larger D_B/D_C, l_m deviates from the initial diffusive trend faster and grows to reach the bottom earlier. This is because the larger D_B/D_C indicates the faster-diffusion B and the slower-diffusion C. On one hand, slow-diffusion C tends to accumulate in the top layer and increase fluid density. Second, fast-diffusion B leads to intensified reaction and more product C. The combination of these two factors contributes to intensifying the unstable stratification and then promoting the onset and growth of density fingering.

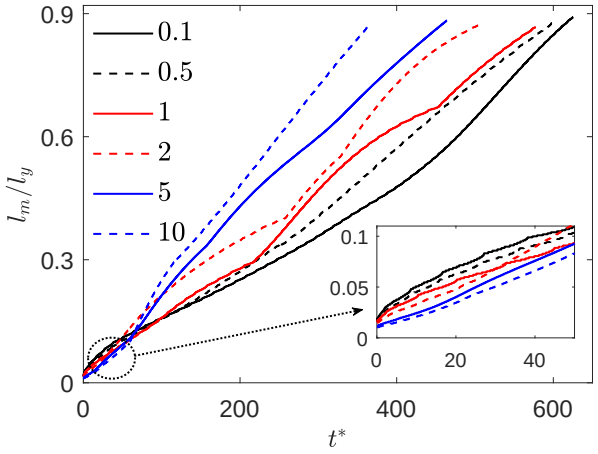

Figure 4.10 Temporal evolutions of fingering extension depth l_m for tests with $\mathrm{Ra}_A = \mathrm{Ra}_B = \mathrm{Ra}_C = 10^9$ and $D_B/D_C = 0.1,\ 0.5,\ 1,\ 2,\ 5,\ 10$ in homogeneous media.

Considering the dissolution of A into the host fluid is always desirable in industrial applications, effects of differential diffusion on the storage behaviors of A are quantitatively investigated. As conducted in Chapter 3, two metrics are calculated. The first one is the

horizontally averaged mass flux of A at the top boundary J^* (Eq. (3.16)). The second one is the amount of A stored in the host fluid, which is defined as the volume-averaged concentration $\langle C_A^* + C_C^* \rangle$ [28]. As illustrated in Fig. 4.11, temporal evolutions of J^* and $\langle C_A^* + C_C^* \rangle$ for each D_B/D_C are qualitatively similar to previous results in Chapter 3 with three species diffusing equally. That is, J^* evolves with time non-monotonically at first and finally fluctuates around a steady-state value, and $\langle C_A^* + C_C^* \rangle$ increases with time monotonically.

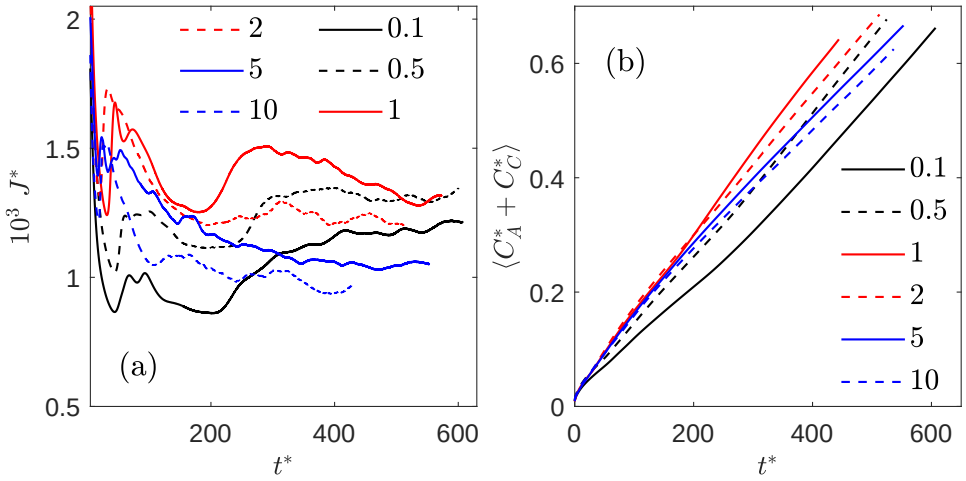

Figure 4.11 Temporal evolutions of horizontally averaged mass flux of A at the top boundary J^* (a) and stored amount of A in the host fluid $\langle C_A^* + C_C^* \rangle$ (b), for tests with $\mathrm{Ra}_A = \mathrm{Ra}_B = \mathrm{Ra}_C = 10^9$ and $D_B/D_C = 0.1,\ 0.5,\ 1,\ 2,\ 5,\ 10$ in homogeneous medium HO.

Regardless of the similar development pattern, differences introduced by differential diffusion are obvious from results in Fig. 4.11. Every J^* with differential diffusion is smaller than the equal-diffusion one. This difference amplifies when the value of D_B/D_C departs from $D_B/D_C = 1$ more obviously (Fig. 4.11(a)). It is attributed to the following two factors. First, for tests with $D_B/D_C < 1$, a local minimum density layer followed by a local maximum density layer develops due to the DLC mechanism (like case P2 in Fig. 4.1(2)). These two layers form a stable barrier to suppress the development of density fingering and the accompanied convection. Thus, less amount of B is brought up to react

with A, which thus decelerates the chemical consumption of A and leads to small J^*. With the increasing D_B/D_C, the intensity of DLC and the inhibition effects of the stable barrier become weak, hence the increased value of J^*. The influence of DLC finally disappears when D_B/D_C increases to be 1 and J^* ascends to reach a peak value. As D_B/D_C continues growing to become larger than 1, the DD mechanism comes into play and introduces a local minimum layer (like case P3 in Fig. 4.3). Similarly, this minimum layer suppresses the dissolution of A and the suppressing intensity accelerates as D_B/D_C increases. That is, with increasing D_B/D_C, J^* increases if $D_B/D_C < 1$, but decreases if $D_B/D_C > 1$.

Similar to results of J^*, lines obtained for $\langle C_A^* + C_C^* \rangle$ in Fig. 4.11(b) also illustrate that the largest amount of A is dissolved into the host fluid as $D_B/D_C = 1$. The stored amount decreases with increasing (or decreasing) D_B/D_C in the range $D_B/D_C > 1$ (or $D_B/D_C < 1$). Thus, calculated J^* and $\langle C_A^* + C_C^* \rangle$ suggest that, differential diffusion suppresses the storage of species A in the host fluid and the inhibition strength increases with the increasing difference between the diffusion rates of B and C. In addition, this conclusion has been checked for other values of $\mathrm{Ra}_B/\mathrm{Ra}_C$.

4.4 Summary

As a continuation of the work in Chapter 3, dissolution-driven density fingering is simulated in a homogeneous porous medium at the pore scale, using the proposed MRT LB model. In these simulations, the effects of both the homogeneous reaction $A + B \rightarrow C$ and differential diffusion are considered. Numerical results demonstrate eight types of density fingering depending on parameters Ra_A (Rayleigh number of species A), $\mathrm{Ra}_B/\mathrm{Ra}_C$ (buoyancy ratio of species B and C), and D_B/D_C (diffusion coefficient ratio of species B and C), which

confirm previous theoretical predictions [82]. On one hand, in cases P1, P4, P5 and P8, fingering dynamics are consistent with equal diffusivity simulation cases R1-R4 in Chapter 3. On the other hand, in cases P2, P3, P6 and P7, differential diffusion causes the double-diffusive (DD) and the diffusive-layer convection (DLC) mechanisms, which subsequently give rise to four new types of density fingering phenomena.

In cases P2 and P6 with $D_B/D_C < 1$ and relatively large $\mathrm{Ra}_B/\mathrm{Ra}_C$, the DLC mechanism introduces a local species-depleted (SD) area at the reaction front (RF) followed by a local species-rich (SR) region. With this species distribution, a local minimum density layer develops at RF and a local maximum density layer forms at SR if $\mathrm{Ra}_A > 0$ (P2), leading to the first density fingering from the top boundary and the second fingering from the DLC-caused local maximum density layer. Two fingering regions are separated by the local minimum density layer and the second fingers deform into antenna-shaped patterns. On the other hand, in cases P3 and P7 with $D_B/D_C > 1$ and relatively small $\mathrm{Ra}_B/\mathrm{Ra}_C$, the DD mechanism produces a local SD area below RF. This then brings in a local minimum density layer at SD to suppress fingering development. But this barrier is finally penetrated by fingering because it is too weak to hinder the sufficiently dense C. Note that, fingering tips below the minimum become narrow in P3 with $\mathrm{Ra}_A < 0$ but strong in P7 with $\mathrm{Ra}_A > 0$. In these four cases, although density curves are initially similar to theoretical results, they gradually change to decrease monotonically (P2 and P3) or increase non-monotonically with a local maximum (P6 and P7), due to the large disorders and non-linear interactions in the late development stage. In addition, in cases P6 and P7 with $\mathrm{Ra}_A < 0$, the DD and DLC mechanisms are found to trigger the development of density fingering.

Finally, the influence of differential diffusion is quantified by a parametric study. Results show that, with increasing D_B/D_C, fingering propagates into the host fluid more slowly in the early stage but gradually becomes faster in the late period. In addition, storage behaviours of A in the host fluid change non-monotonically with D_B/D_C: the storage of A reaches a peak value at $D_B = D_C$ but decreases as the difference between D_B and D_C increases. Thus, differential diffusion tends to suppress the storage of A.

The present pore-scale results indicate that understanding effects of differential diffusion is of great importance for industrial applications, such as geological CO_2 sequestration. That is, comparing chemical compositions among different underground sites and selecting the one, with reaction and differential diffusion enhancing the storage of CO_2, is important to improving the storage efficiency and safety.

CHAPTER 5

Miscible viscous fingering coupled with dissolution reaction

Global climate change is happening but may be mitigated by the technology of carbon dioxide (CO_2) sequestration in geological reservoirs. To gain comprehensive insights into this approach, pore-scale simulations of the displacement between two miscible fluids in porous media are necessary. During the miscible displacement, viscous fingering arises when the displacing fluid is less viscous than the displaced one. This interface instability is a common phenomenon in CO_2 sequestration because the injected CO_2 is less viscous than the host brine. In addition, in porous media, miscible viscous fingering is usually affected by chemical dissolutions of porous matrices [26, 92]. Recently, some pore-scale studies on miscible viscous fingering in porous media have been carried out, but have not involved the presence of dissolution reaction. The motivation of this chapter is to investigate miscible viscous fingering in porous media at the pore scale, with the coexistence of viscosity contrast and dissolution reaction being considered. The modelled results will be of interest to industrial applications like CO_2 sequestration.

5.1 Problem description

In this chapter, the miscible displacement between two fluids 1 and 2 is investigated in porous media at the pore scale. As depicted in Fig. 5.1, a 2D homogeneous structure with length l_x and width l_y is built [63]. This porous network contains a staggered array of circular and non-reactive grains, which are homogeneously coated by reactive solid *Bs*.

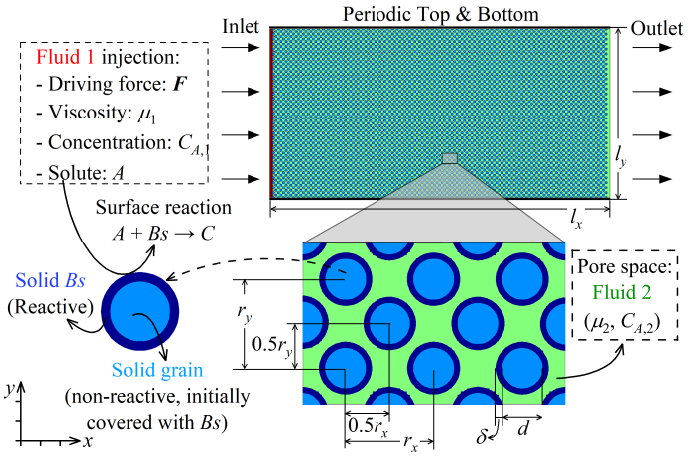

Figure 5.1 The schematic of the problem: Miscible displacement between two fluids with viscous contrast and dissolution reaction in porous media.

Pore spaces between these grains are initially filled with fluid 2 of viscosity μ_2. Another fluid 1 of viscosity μ_1 is injected from the left inlet by a driving force $\boldsymbol{F} = (F_x,\, 0)$ to displace fluid 2. These two fluids are considered miscible, incompressible, isothermal, and neutrally buoyant. During such a displacement, viscous fingering is expected to occur if the displacing fluid 1 is less viscous than fluid 2 ($\mu_1 < \mu_2$). In the meantime, the injected fluid 1 contains a solute A in concentration $C_A = C_{A,1}$, while fluid 2 does not ($C_A = C_{A,2} = 0$). Solute A can act as a dissolving component to react with solid Bs following the $A + Bs \rightarrow C$ scheme, with the reaction product C being in the dissolved form. The reaction rate F_r of this dissolution reaction is defined as [47],

$$F_r = kC_A^I, \tag{5.1}$$

where k is the kinetic reaction constant and C_A^I is the concentration of solute A at the interface I between fluid 1 and solid Bs. As solid Bs is dissolved out gradually, the update of the porous structure is tracked by [47],

$$\partial_t V_B = -S_B V_{Bm} F_r, \tag{5.2}$$

where V_B and V_{Bm} are the volume and the molar volume of solid Bs, respectively, and S_B is the reactive surface area. Such a dissolution reaction changes medium porosity and permeability, leading to variations in fluid mobility and interface instability.

Based on the above introduction, governing equations for fluid flow and concentration transport in pore spaces can be built as in Eqs. (2.64)-(2.66). By introducing the characteristic length $L = l_y$, velocity $U = \nu_2/L$, and concentration $C_{ch} = C_{A,1}$, dimensionless parameters marked by asterisks can be derived as,

$$t^* = \frac{t}{L/U},\ c^* = \frac{C_A}{C_{ch}},\ \mathrm{Pe} = \frac{LU}{D},\ \mathrm{Re} = \frac{LU}{\nu},\ \mathrm{Da} = \frac{k}{U}. \tag{5.3}$$

Key characteristic numbers of this problem are: the viscosity ratio R, the Reynolds number Re, the Peclet number Pe, and the Damköhler number Da.

The D2Q9 MRT LB model developed in Sec. 2.2.2 is used to study viscous fingering dynamics in the context of miscible displacement with dissolution reaction. To conduct pore-scale simulations in the homogeneous medium as built in Fig. 5.1, geometric parameters are set as, $l_x = 1$, $l_y = 0.497$, $d = 0.0063$, $\delta = 0.001$, and $r_x = r_y = 0.015$, respectively, leading to the medium porosity as $\phi = 0.508$ and the initial volume fraction of solid Bs as $\phi_{B,0} = 0.232$. In regards to boundary conditions, the top and bottom boundaries are periodic, zero-gradient conditions are applied for all the scalars at the outlet, and fixed viscosity and concentration of fluid 1 are employed at the inlet. Moreover, the Reynolds number of fluid 2 and the driving force are fixed as $\mathrm{Re} = 1.0$ and $F_x = 0.09$, respectively. Different values of viscosity ratio R, Peclet number Pe, and Damköhler number Da are chosen to change modelling conditions. Before proceeding further, grid convergence tests have been carried out. After grid independence tests, a mesh of size $N_x \times N_y = 1920 \times 954$ is selected to describe the medium in Fig. 5.1, with geometrical parameters being, $d = 12\delta_x$,

$\delta = 2\delta_x$, $r_x = r_y = 28\delta_x$, and $\delta_x = l_x/N_x$, respectively. Each of the following simulations continues until the fluid front, l_f, reaches the position $0.75l_x$. Note that, all parameters are set in lattice units and the fluid front refers to the front position of fluid 1.

5.2 General viscous fingering patterns

Pore-scale simulations are firstly performed to investigate general patterns and dynamics of miscible viscous fingering, in the presence of both viscosity contrast and dissolution reaction. Numerical results reveal different fingering types that are determined by coupled effects of three factors, namely, viscosity contrast (R), fluid diffusion (Pe), and chemical dissolution (Da). As an example, two sets of simulations are discussed to illustrate these fingering patterns, including cases Ia-Ic with R $= 3$, Pe $= 30$, and Da $= 0,\ 0.01,\ 0.3$; and cases IIa-IIc with R $= -0.5$, Pe $= 30$, and Da $= 0,\ 0.01,\ 0.3$. These three Da values are selected to represent no dissolution, slow dissolution, and fast dissolution, respectively.

Cases Ia-Ic are considered at first, of which the viscosity contrast between fluids 1 and 2 is classically understood as unstable (R $= 3$). For each test, Fig. 5.2 depicts spatial distributions of concentration c^* at four time instants, showing a classical development pattern of viscous fingering [29, 48]. That is, upon the injection of fluid 1 from the inlet, the displacement starts with a planar fluid interface and the system is dominated by fluid diffusion (Figs. 5.2(a1), (b1), (c1)). As the injection continues, the initially uniform interface gradually distorts and grows into viscous fingering to control the displacement dynamics (Figs. 5.2(a2), (b2), (c2)). After this fingering initiation stage, fingers experience individual growth, nonlinear interaction, merge, and fading periods (Figs. 5.2(a3), (b3),

(c3)). In the final stage, only a few leading fingers are left, which will block or adsorb trailing fingers.

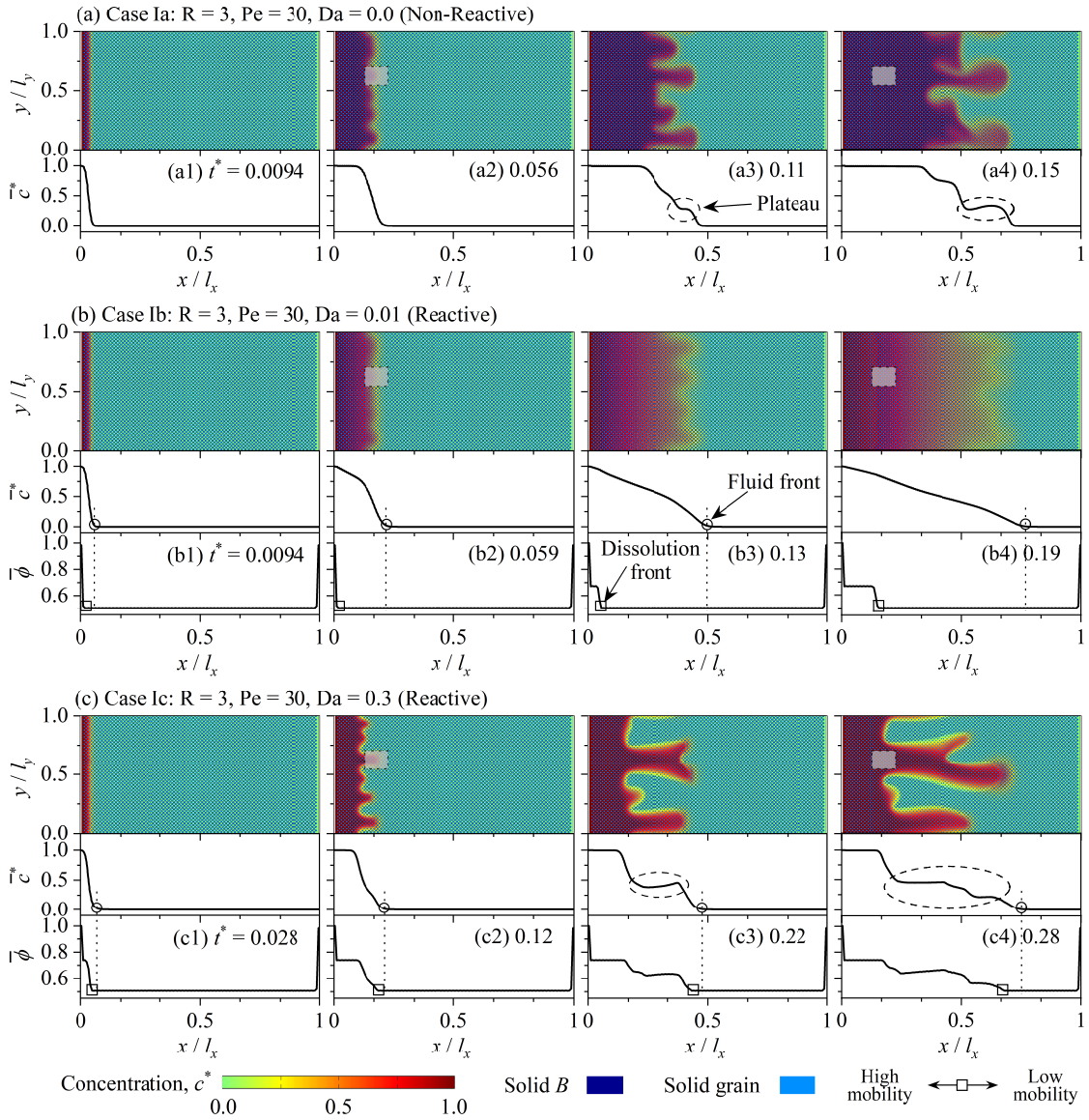

Figure 5.2 Concentration contours c^* and transversely averaged concentration $\overline{c^*}$ and porosity $\overline{\phi}$ at four time instants, for cases Ia-Ic with R = 3, Pe = 30, and Da = 0 (a), 0.01 (b), 0.3 (c). Gray rectangles are marked for zoom-in views in Fig. 5.3.

In spite of this similar development pattern, the dissolution of solid *Bs* is different among the three cases. As an illustration, Fig. 5.3 provides zoom-in views of concentration and residual solid *Bs* distributions. In case Ia with no dissolution (Fig. 5.3(a)), solid *Bs* keeps its initial distribution and medium porosity remains unchanged during

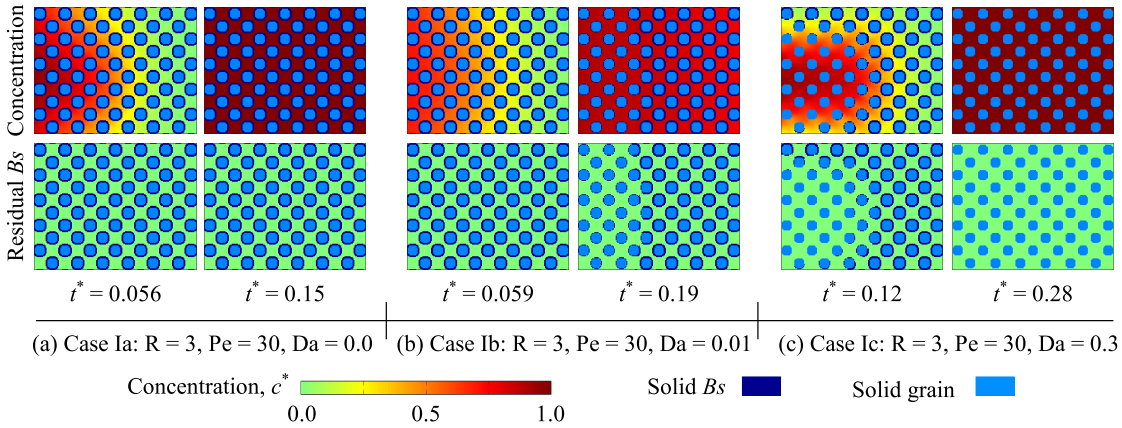

Figure 5.3 Zoom-in views of regions highlighted by gray rectangles in Fig. 5.2: concentration c^* and residual solid *Bs* distributions at two time instants, for cases Ia-Ic with R = 3, Pe = 30, and Da = 0 (a), 0.01 (b), and 0.3 (c).

the displacement. With the introduction of dissolution in cases Ib-Ic (Figs. 5.3(b)-(c)), solid *Bs* is gradually dissolved out and medium porosity increases behind the moving interface between the two fluids. This results in a situation of fluid 1 from a high-mobility region displacing fluid 2 in a low-mobility area. To further quantify the difference in dissolution dynamics between cases Ib and Ic, transversely averaged concentration $\overline{c^*}$ and porosity $\overline{\phi}$ are calculated in Figs. 5.2(b)-(c). Note that, due to the slow dissolution in case Ib, the propagation of fluid 1 (or the fluid front) obviously exceeds the expansion of the high-mobility area (or the dissolution front) along the flow direction. Differently, in case Ic, expansions of fluid 1 and the high-mobility area are almost consistent with each other. It is because dissolution is fast enough to exhaust both species *A* and solid *Bs* at the moving interface, making fluid 1 accumulate in but not penetrate the high-mobility region.

In addition, cases Ia-Ic demonstrate different fingering dynamics during different development stages. On one hand, at the initiation stage (Figs. 5.2(a2), (b2), (c2)), fingering appears the earliest in the non-reactive case Ia (Da = 0) and much later in the two reactive cases Ib and Ic, indicating that dissolution delays the onset of fingering. To quantitatively explain this impact, Fig. 5.4 provides transversely averaged concentration $\overline{c^*}$ and viscosity

$\ln(\overline{\mu}/\mu_1)$, as well as truncated contours for cases Ia-Ic at $t^* = 0.075$. In case Ib, the low-speed dissolution consumes species A in fluid 1 but cannot suppress the propagation of fluid 1. It thus increases viscosity of fluid 1 and decreases viscosity contrast between fluids 1 and 2. Differently, in case Ic, the high-speed dissolution slows down the accumulation and expansion of fluid 1 along the displacing direction. Both the decreased viscosity contrast (case Ib) and the decelerated displacing fluid 1 (case Ic) contribute to the delayed viscous fingering appearance. Additionally, as Da increases from cases Ib to Ic, the fingering delay period lasts longer and thus the suppressing effect of dissolution is stronger.

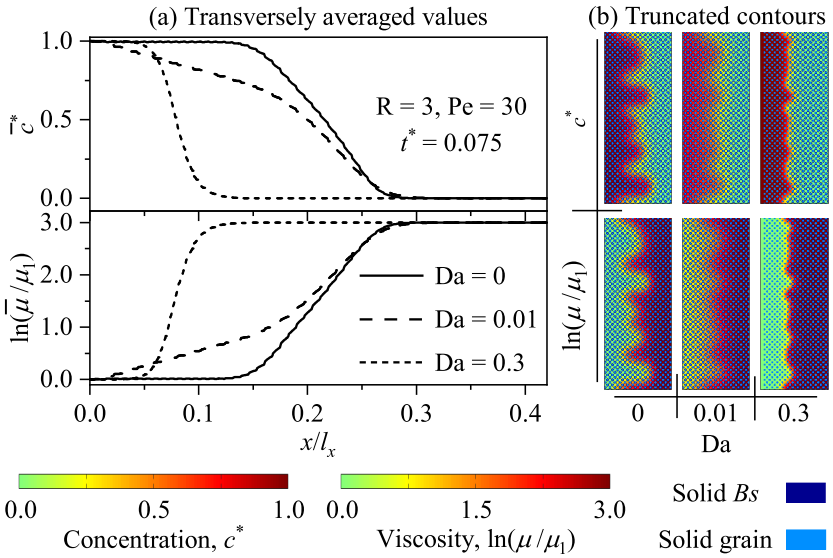

Figure 5.4 Transversely averaged concentration $\overline{c^*}$ and viscosity $\ln(\overline{\mu}/\mu_1)$ (a), and truncated contours of c^* and $\ln(\mu/\mu_1)$ (b), for cases Ia-Ic with R $= 3$, Pe $= 30$, and Da $= 0,\ 0.01,\ 0.3$, at time instant $t^* = 0.075$.

On the other hand, at the late stage, the influence of dissolution becomes non-monotonic. That is, compared with case Ia (Figs. 5.2(a2)-(a4)), chemical dissolution tends to stabilize (Figs. 5.2(b2)-(b4)) or destabilize (Figs. 5.2(c2)-(c4)) viscous fingering, depending on the dissolution rate Da. In case Ia, fingers grow and merge with neighboring ones, forming two obvious fingers during the late stage. This is however absent in case Ib, where fingers fade away with time. It is attributed to the fact that the slow dissolution keeps smoothening

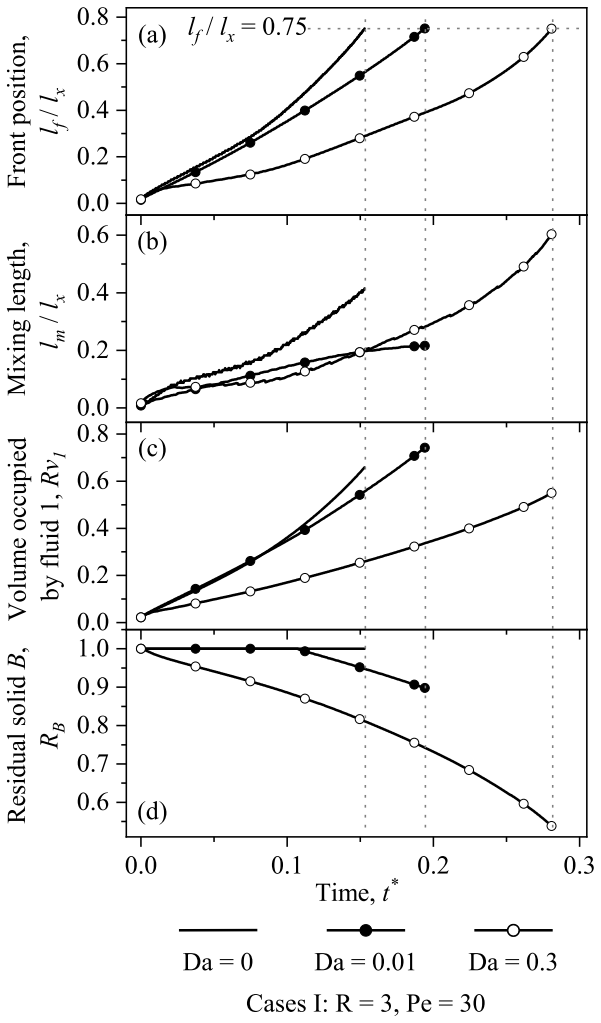

Figure 5.5 Temporal evolutions of front position l_f/l_x (a), mixing length l_m/l_x (b), volume fraction of fluid 1 Rv_1 (c), and residual solid Bs R_B (d), for cases I with R = 3, Pe = 30, and Da = 0.0, 0.01, 0.3.

the fluid viscosity contrast and suppressing fingering development. In case Ic, although the onset of fingering is delayed, the fast dissolution of solid Bs, in turn, brings in a high-mobility region saturated with the displacing fluid 1 behind the moving interface. This subsequently enlarges the fluid mobility contrast and results in the enhanced fingering dynamics (i.e., long fingering and tip splitting). Such a destabilizing effect of dissolution is not observed in case Ic because, as mentioned above, the expansion of the high-mobility area is obviously slower than the propagation of fluid 1. In addition, profiles of transversely averaged concentration $\overline{c^*}$ exhibit plateaus in cases Ia and Ic (Fig. 5.2). These plateaus emerge because fingers contain almost the same quantity of A. By comparing the plateau

length, it is also concluded that viscous fingering is reinforced by fast dissolution but inhibited by slow dissolution at the late development stage.

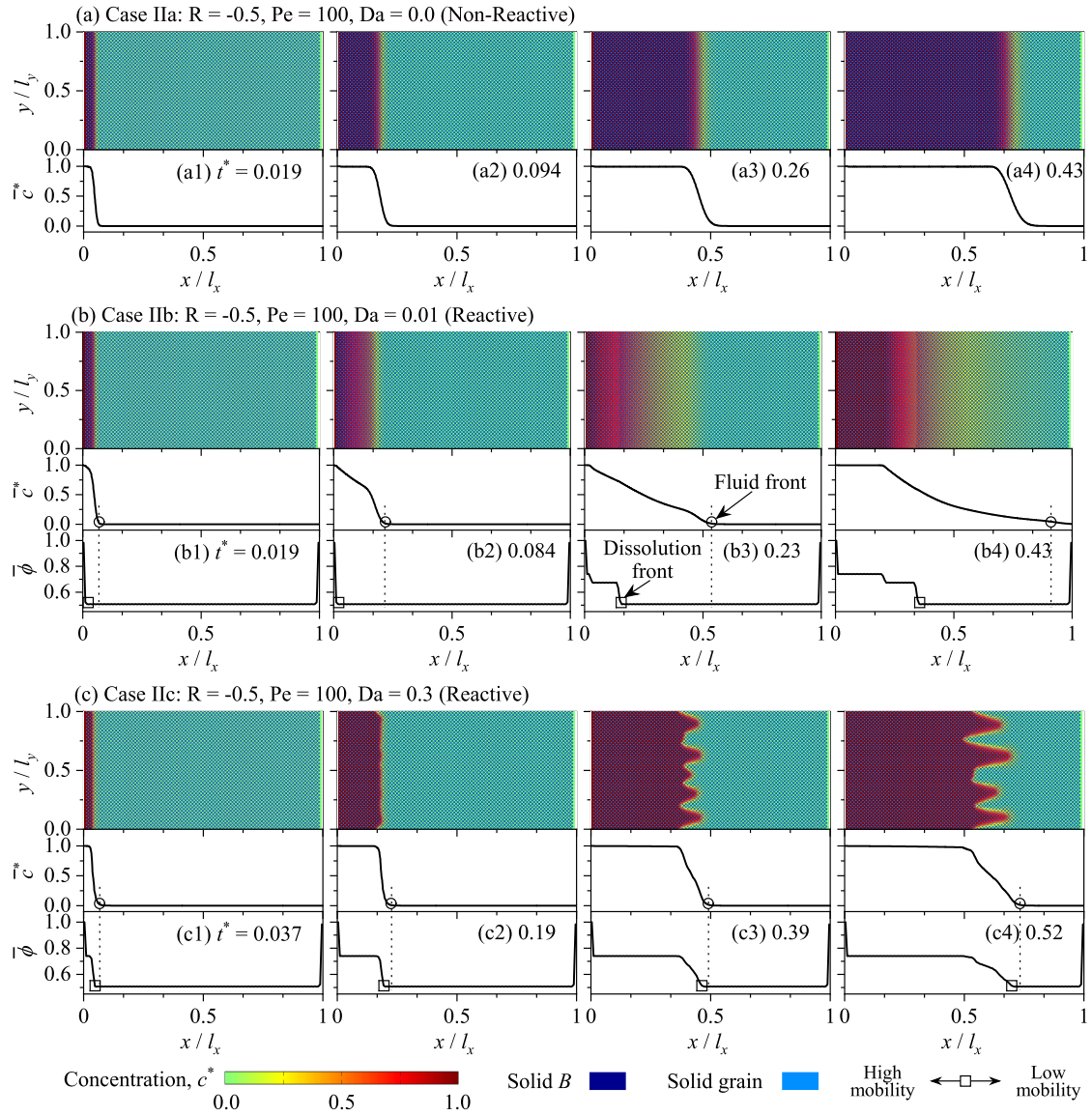

Figure 5.6 Concentration contours c^* and transversely averaged concentration $\overline{c^*}$ and porosity $\overline{\phi}$ at four time instants, for cases IIa-IIc with R $= -0.5$, Pe $= 100$, and Da $= 0$ (a), 0.01 (b), and 0.3 (c).

To quantitatively grasp fingering dynamics in cases I, Fig. 5.5 plots temporal evolutions of front position l_f/l_x, mixing length l_m/l_x, volume fraction of fluid 1 $Rv_1 = V_1/V_p$, and residual solid *Bs* $R_B = \phi_B/\phi_{B,0}$. Parameters V_1, V_p, and ϕ_B are the volume occupied by fluid 1, the volume of pore spaces, and the volume fraction of *Bs* at a given time, respectively. Note that, based on profiles of transversely averaged concentration $\overline{c^*}$, l_f is defined as

the position with $\overline{c^*} = 0.01$ and l_m is calculated as the distance between $\overline{c^*} = 0.01$ and $\overline{c^*} = 0.99$. Curves of l_f/l_x in Fig. 5.5(a) show the non-reactive case Ia propagates faster than the two reactive cases Ib-Ic. It is because chemical dissolution consumes species A, which contributes to decreasing viscosity (or increasing mobility) of the displacing fluid 1. To understand behaviours of l_m/l_x as a function of time in Fig. 5.5(b), it is recalled that l_m/l_x grows in a diffusive tendency during the initial period, but starts to depart from this tendency once viscous fingering appears, exhibiting two different growth velocities [29, 48]. It is thus observed, from profiles of l_m/l_x, that dissolution delays the onset of fingering in reactive cases Ib-Ic and even suppresses the late-stage fingering growth in case Ib. Results of Rv_1 and R_B in Figs. 5.5(c)-(d) suggest that the dissolution of Bs (or the expansion of high-mobility area) is slower than the propagation of fluid 1 in case Ib. Finally, by comparing final states (with $l_f/l_x = 0.75$) of cases Ia-Ic, the fast dissolution case Ic is found to feature the strongest fingering with the longest mixing length (or fingering length). These results quantitatively confirm the above observations from Fig. 5.2.

For a comprehensive understanding, cases IIa-IIc with a stable viscosity gradient R $= -0.5$ are then investigated. Figure 5.6 shows the spatial-temporal evolutions of concentration c^* and transversely averaged concentration $\overline{c^*}$ and porosity $\overline{\phi}$. In cases IIa and IIb, diffusion dominates the displacement and fluid interface remains almost undeformed. Once fast dissolution comes into play in case IIc, fluid interface is distorted with time and finally becomes fingered, in spite of the stable viscosity contrast. As explained in cases I, it is because fast dissolution results in an unstable situation of high-mobility fluid 1 displacing low-mobility fluid 2. This subsequently triggers viscous fingering (or infiltration instability). Different displacement dynamics between cases IIb and IIc suggest the onset

of fingering requires sufficiently fast dissolution. In addition, compared with cases I, fingering is less intense here and no obvious plateau is observed in profiles of $\overline{c^*}$, indicating the importance of viscosity contrast to viscous fingering. As in cases I, these observations are verified by quantitative profiles, which are not provided for brevity.

In conclusion, for viscous unstable cases ($R > 0$), dissolution delays the onset of viscous fingering. During the late stage of fingering development, however, dissolution may stabilize or destabilize viscous fingering, depending on the dissolution rate Da. The suppressed viscous fingering under slow dissolution is a novel finding of this chapter. On the other hand, in viscous stable situations with fluid viscosity decreasing along the propagation direction ($R < 0$), fast dissolution is capable of triggering the development of viscous fingering, which however is less intense than that in viscous unstable cases.

5.3 Effects of Pe and R

After discussing general fingering dynamics and patterns, effects of Pe and R are then investigated. Simulations are performed at a fixed $Da = 0.3$ and a wide range of R and Pe. Figure 5.7(a) plots the concentration contour for each test at the time instant when the fluid front moves to $l_f = 0.6l_x$. A range of fingering dynamics are visible from these concentration distributions, including no interface instability, marginal fingering, and intense fingering. In tests with small R or Pe, the fluid interface remains flat as the stable viscosity contrast or fluid diffusion dominates the system. Nevertheless, with increasing R or Pe, an interface deformation tendency and a transition from planar interface to viscous fingering are noticed. These observations are in qualitative agreement with existing results of miscible viscous fingering without dissolution [105].

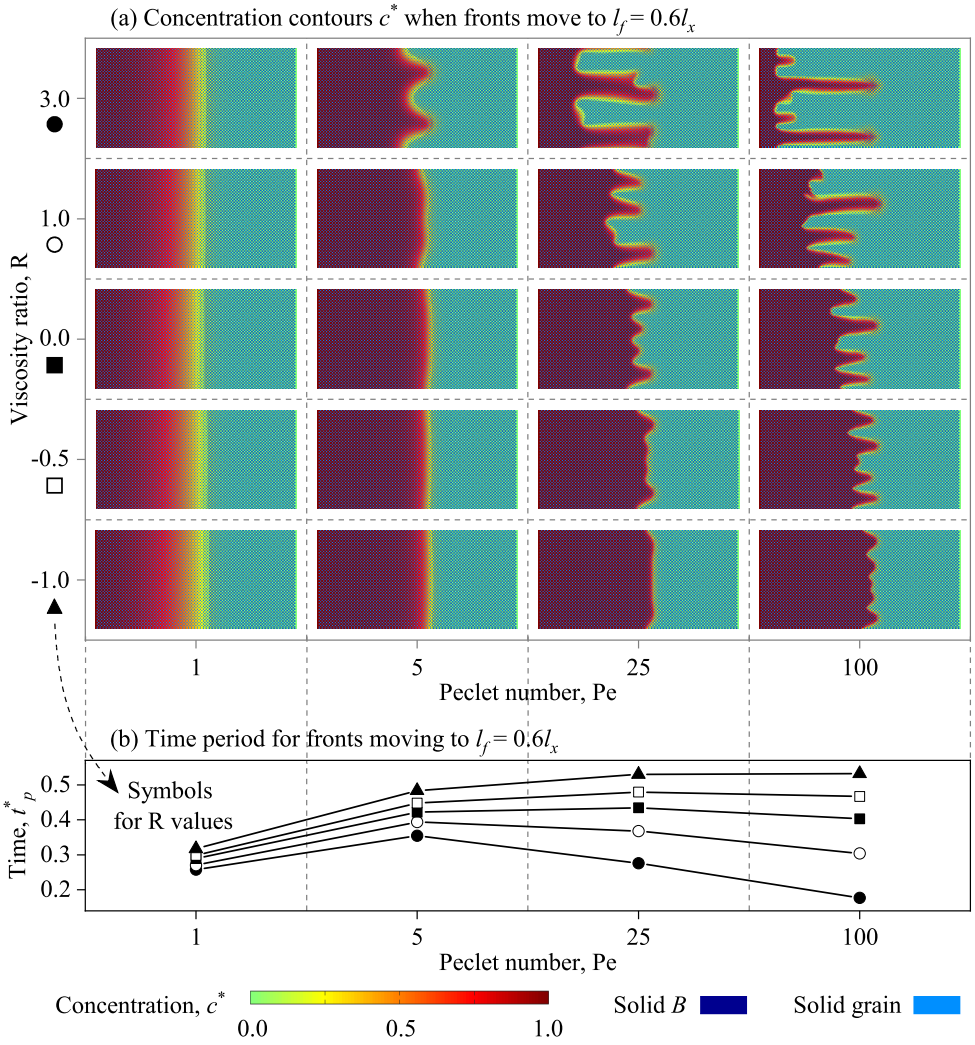

Figure 5.7 Concentration contours c^* when fluid fronts move to $l_f = 0.6l_x$, for cases with Da $= 0.3$ and different values of R and Pe (a). Plots of time periods t_p^* required for fronts moving to $l_f = 0.6l_x$ as a function of Pe for different R (b).

Moreover, Fig. 5.7(b) measures the time period t_p^* required for a fluid front to propagate to the position $l_f = 0.6l_x$. The smaller t_p^* indicates the faster displacing speed. All cases are observed to share a common tendency that, with increasing R, the displacing speed increases monotonically. It is because the larger R represents the less viscous fluid 1. In contrast, with ascending Pe, the displacing speed is found to decrease at first and then turn to increase at later times. This can be explained in terms of the stability condition of the fluid interface: with the increase in Pe at each fixed R, the fluid interface transits from stable diffusion to viscous fingering. In the diffusion regime, larger Pe denotes slower

diffusion and thus a decreased displacing speed. Once viscous effects take over, fingering development and fluid front propagation are accelerated by ascending Pe. It indicates that the maximum t_p^* at each fixed R locates near the transition point from stable diffusion to unstable fingering.

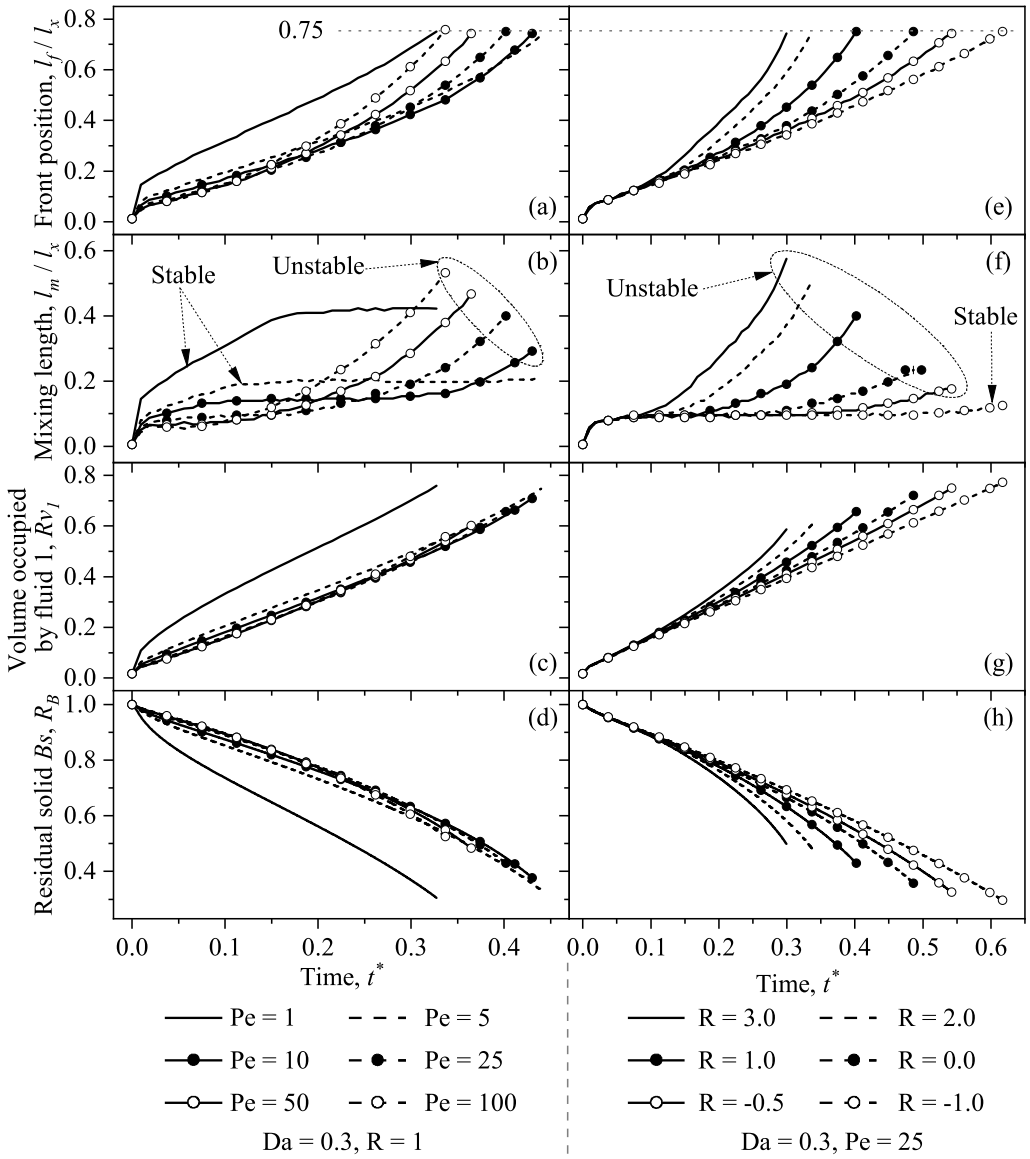

Figure 5.8 Temporal evolutions of front position l_f/l_x, mixing length l_m/l_x, volume fraction of fluid 1 Rv_1, and residual solid Bs R_B, for cases with R = 1, Da = 0.3, and different Pe (a)-(d); and cases with Pe = 25, Da = 0.3, and varying R (e)-(h).

To quantify effects of R and Pe, temporal evolutions of front position l_f/l_x, mixing length l_m/l_x, volume fraction of fluid 1 Rv_1, and residual solid Bs R_B are provided, for

tests with fixed Da = 0.3 and R = 1 but varying Pe (Figs. 5.8(a)-(d)), or fixed Da = 0.3 and Pe = 25 but different R (Figs. 5.8(e)-(h)). First, profiles of l_m/l_x in Figs. 5.8(b) and (f) demonstrate that, with increasing Pe or R, the system transits from stable to unstable states and fingering starts earlier. This finding is consistent with observations from Fig. 5.7. Then, curves of Rv_1 and R_B in Figs. 5.8(c)-(d) indicate the increase in Pe suppresses the storage of fluid 1 and the consumption rate of *Bs*. Such effects continue in stable cases but become negligible in unstable cases. Finally, Figs. 5.8(g)-(h) show both the storage of fluid 1 and the dissolution of *Bs* are boosted monotonically by increasing R.

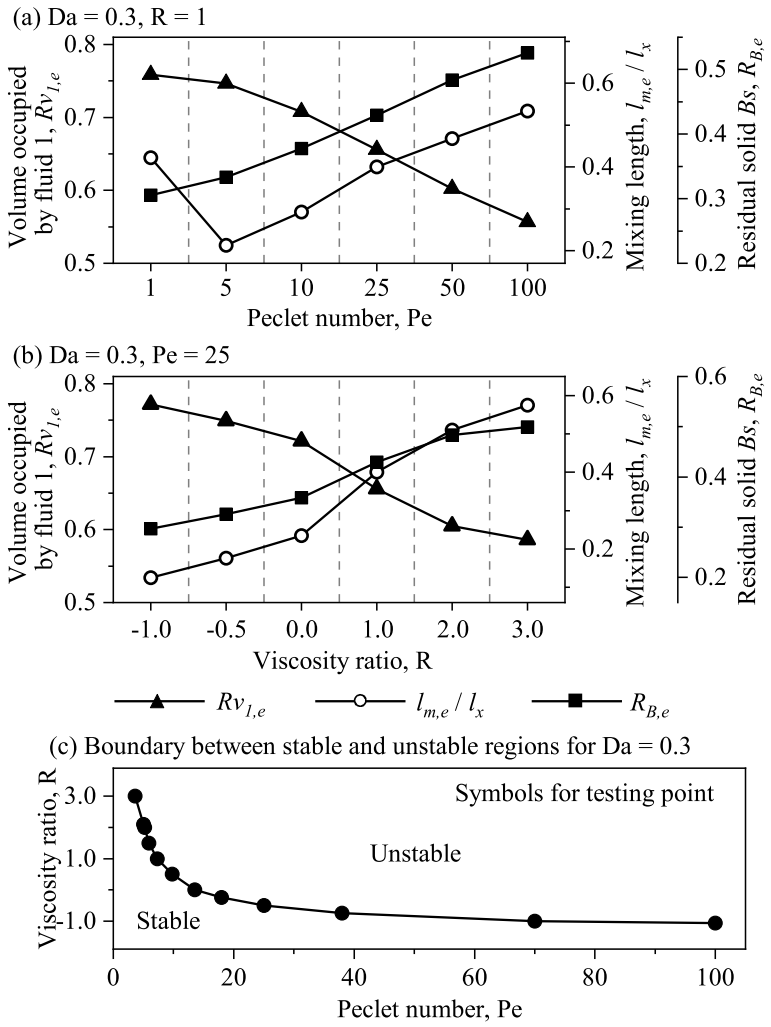

Figure 5.9 Plots of mixing length $l_{m,e}/l_x$, volume fraction of fluid 1 $Rv_{1,e}$, residual solid *Bs* $R_{B,e}$ at the time instant with $l_f = 0.75l_x$: as a function of Pe for cases with R = 1 and Da = 0.3 (a); as a function of R for cases with Pe = 25 and Da = 0.3 (b). Phase plot in the Pe-R plane for Da = 0.3, showing a stable and an unstable regions (c).

Based on these temporal results, Figs. 5.9(a)-(b) measure final values of mixing length $l_{m,e}/l_x$, volume fraction of fluid 1 $Rv_{1,e}$, and residual solid Bs $R_{B,e}$, when fluid fronts move to $l_f/l_x = 0.75$. On one hand, with the increase in Pe or R, descending $Rv_{1,e}$ profiles and ascending $R_{B,e}$ curves are evident in Figs. 5.9(a)-(b). This is because, as shown in Fig. 5.7(a), viscous fingering is intensified as Pe or R ascends, causing less volume being occupied by fluid 1 and more solid Bs being left un-dissolved behind the fluid front. On the other hand, curves of $l_{m,e}/l_x$ generally ascend with increasing Pe or R, suggesting the intensified viscous fingering. A different tendency should be noted: the profile of $l_{m,e}/l_x$ decreases with Pe when Pe is relatively small. It is because diffusion dominates the displacement and larger Pe represents slower fluid diffusion and smaller $l_{m,e}/l_x$. This declining tendency however lasts a small range of Pe and then $l_{m,e}/l_x$ turns to increase with Pe, indicating the system transits into the unstable state with viscous fingering. A local minimum in $l_{m,e}/l_x$ is thus noticed and the corresponding Pe can roughly represent the threshold for the unstable regime.

In general, it is both qualitatively and quantitatively demonstrated that fingering intensity boosts with increasing R or Pe. To grasp the distribution of system stability conditions in a phase plane spanned by Pe and R, profiles of l_m for fixed Pe and Da but varying R are further compared, as conducted in Fig. 5.8(f). To stand for the stable state, a reference curve of mixing length $l_{m,r}$ is measured versus time at R $= -2.5$ for each pair of Pe and Da. The viscosity ratio R $= -2.5$ is selected after checking that it can make the system stay stable despite values of Pe and Da. Consequently, l_m is compared with $l_{m,r}$ to identify the parameter set (Pe, Da, R) as stable or unstable. If l_m coincides with $l_{m,r}$ even up to the final time (when $l_f = 0.75l_x$), the corresponding case with (Pe, Da, R) is identified as stable,

otherwise, it is unstable. Accordingly, for Da $= 0.3$, the stable and unstable cases obtained are summarised in the Pe-R space in Fig. 5.9(c). Results show that, along constant Pe (or R) lines, the system undergoes a transition from stable planar interface to unstable viscous fingering. This reveals the existence of a critical Pe_c at a given R (or a critical R_c at a fixed Pe) for the onset of viscous fingering. A boundary line, on which critical parameters (Pe_c, R_c) distribute, is thus identified. Such a line divides the Pe-R space into a stable regime and an unstable one.

5.4 Effects of Da

Effects of the dissolution rate Da on fingering dynamics are explored in two subsections. Considering that typical fingering phenomena with varying Da have been discussed in Sec. 5.2, this subsection focuses on quantitative results. For cases with Pe $= 30$ and R $= 3$, values of three metrics at the final time instant (when $l_f = 0.75 l_x$), i.e., mixing length $l_{m,e}/l_x$, volume fraction of fluid 1 $Rv_{1,e}$, and residual solid *Bs* $R_{B,e}$, are depicted as a function of Da in Fig. 5.10. On one hand, from profiles of $l_{m,e}/l_x$ and $Rv_{1,e}$, a local minimum and a local maximum are noticed at around Da $= 0.01$. It is attributed to the fact that dissolution inhibits viscous fingering at small Da and goes back to enhance fingering after a threshold at around $\mathrm{Da}_c = 0.01$. This tendency is illustrated via truncated concentration contours in Fig. 5.10. Note that, as Da increases, either $l_{m,e}/l_x$ or $Rv_{1,e}$ gradually approaches an asymptotic value and then the destabilizing effect of dissolution is reflected by tip splitting phenomena. On the other hand, results of $R_{B,e}$ demonstrate, as expected, that large dissolution rate Da brings in less residual *Bs*. In addition, Fig. 5.10 compares the time period t_e^* required for the fluid front to move to $l_f = 0.75 l_x$ in each

case, showing that t_e^* accelerates with Da. As explained above, this is because dissolution consumes species A and slows down the development speed of fingering. Again, these findings quantitatively confirm observations in Sec. 5.2. Similar simulations and analyses are conducted for varying Da at other pairs of (Pe, R) and results in Fig. 5.10 remain almost unaffected in terms of qualitative tendency.

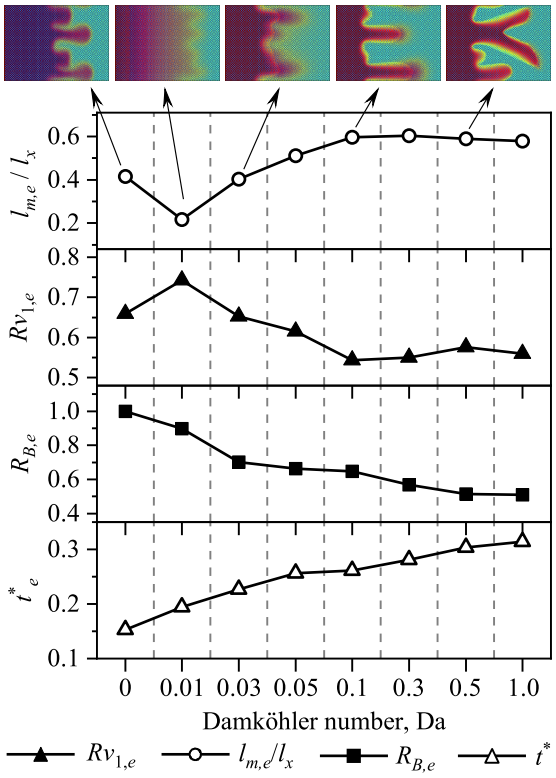

Figure 5.10 Plots of mixing length $l_{m,e}/l_x$, volume fraction of fluid 1 $Rv_{1,e}$, residual solid Bs $R_{B,e}$, and time period t_e^* for fronts moving to $l_f = 0.75l_x$, as a function of Da with R = 3 and Pe = 30.

The analysis mentioned in Sec. 5.3 is then conducted to summarize stable and unstable cases obtained in the Pe-R parameter space for different values of Da. To grasp the distribution of typical fingering patterns, boundary lines for Da $= 0.0,\ 0.01,\ 0.3$ are firstly provided in Fig. 5.11. Similar to results in Fig. 5.9(c), each boundary line divides the space into a stable area and an unstable one. In addition, the curve for non-reactive cases (Da $=$ 0.0) is sandwiched between the two reactive profiles (Da $= 0.01,\ 0.3$). Under these three lines, four different stability regimes are further obtained: unstable (I), stable (II), reactive

stable (III), and reactive unstable (IV). As an example, truncated concentration contours are provided in Fig. 5.11 to help visualize fingering patterns in these four regions. It is emphasized that, the reactive stable regime, as a novel finding, gives stable displacements even though under non-reactive unstable conditions. These results help to enrich the understanding of dissolution reaction effects on viscous fingering.

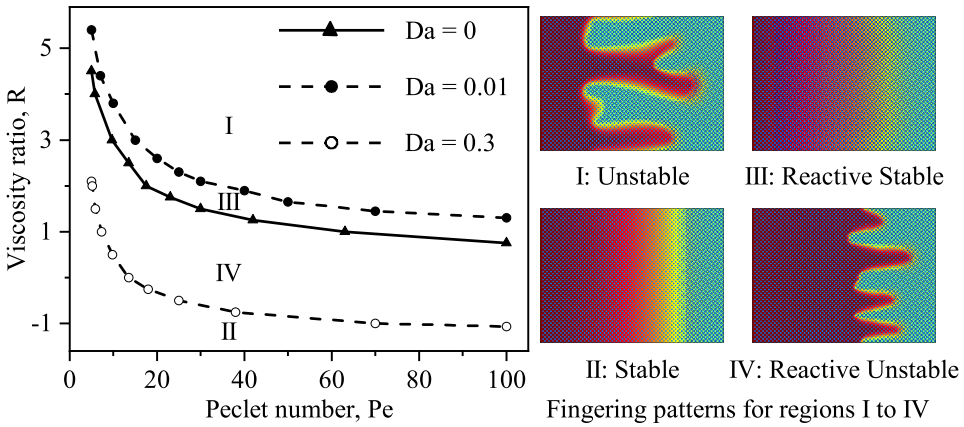

Figure 5.11 Phase plot in the Pe-R plane for Da $= 0.0,\ 0.01,\ 0.3$, with each boundary line dividing the space into a stable and an unstable regions. Three lines divide four distinct regimes: unstable (I), stable (II), reactive stable (III), and reactive unstable (IV). Truncated concentration contours are presented to illustrate fingering phenomena under these regimes.

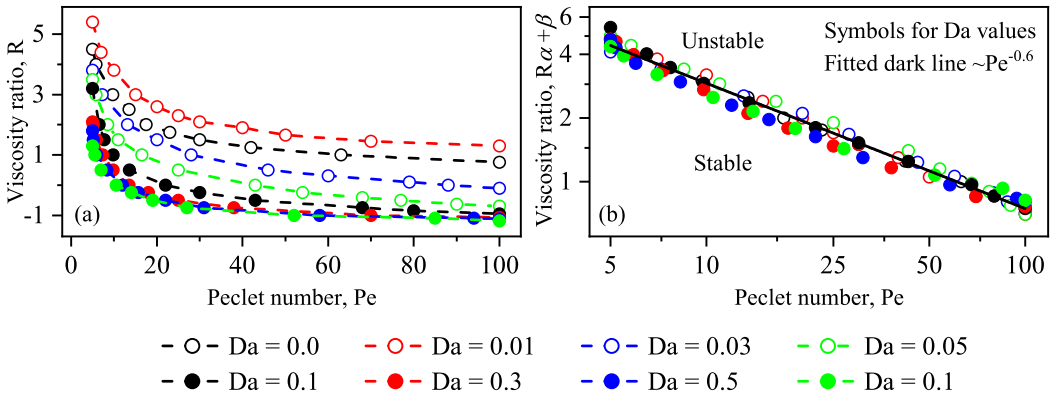

Figure 5.12 Phase plot in the Pe-R plane for different values of Da, with the space being divided into a stable and an unstable regions for each Da (a). Boundary lines between stable and unstable zones in the normalised Pe-R space (b).

Furthermore, Fig. 5.12(a) shows boundary lines between stable and unstable regions for a wide range of Da in the Pe-R parameter spaces. It is observed that, with increasing Da, the unstable region spans over a smaller range of both Pe and R than the non-reactive case

at first, but turns to span a larger area after a threshold value (approximately at $\mathrm{Da}_c = 0.01$). In addition, regime boundary lines for different Da follow a unified scaling relation as $\mathrm{R}_c\alpha + \beta \sim \mathrm{Pe}_c^{-0.6}$, with correlations α and β being related to the dissolution rate Da. Using this scaling relation we may predict the stability of miscible displacement with dissolution in porous media. It is worth mentioning that porous media with different domain sizes or porosities have been constructed for repeating the above simulations of viscous fingering with dissolution reaction. The observed fingering dynamics are qualitatively the same as the present findings.

5.5 Summary

Based on the proposed MRT LB model, pore-scale simulations of miscible displacement between two fluids have been performed in a homogeneous porous medium. Considering that finger-shaped propagation affects the storage efficiency of the displacing fluid, viscous fingering dynamics are investigated in situations with both viscosity contrast and dissolution reaction. Specifically, a chemical component is introduced in the displacing fluid to dissolve porous matrices and cause the evolution of the porous structure. Simulations have been conducted over a wide range of Damköhler number Da, Peclet number Pe, and viscosity ratio R.

The results obtained demonstrate different fingering patterns. On one hand, in situations of a less viscous fluid displacing a more viscous one ($\mathrm{R} > 0$), dissolution decelerates both the onset and the development of viscous fingering. A new finding is that, during the late development stage, viscous fingering gradually fades away in slow-dissolution cases, but becomes intensified and features long fingers and tip splitting under fast-dissolution

conditions. On the other hand, for cases with stable viscosity contrast ($R < 0$), fast dissolution is observed to increase medium porosity behind the moving interface and thus trigger viscous fingering. In addition, effects of Pe, R, and Da have been quantitatively analyzed. Results suggest that, as Pe or R increases, the intensified viscous fingering is made evident by long and clear fingers. By contrast, with the increase in Da, fingering intensity is firstly suppressed and then enhanced by chemical dissolution. By measuring behaviours of mixing length, the stability condition of each test is identified and summarized in a parameter space spanned by Pe and R. For each fixed Da, a boundary line is determined to divide the Pe-R space into a stable region and an unstable one. All the boundary lines for different Da values show a similar pattern and are scaled by a unified empirical equation. Furthermore, the boundary line for non-reactive cases ($Da = 0$) is sandwiched by reactive lines ($Da > 0$). Thus, four distinct stability regimes are classified as, unstable, stable, reactive stable, and reactive unstable. Based on the present pore-scale simulations, improved physical insights into miscible viscous fingering with dissolution reaction are achieved and useful suggestions for geological CO_2 sequestration are obtained, like introducing appropriate dissolution components to inhibit viscous fingering.

CHAPTER 6 Coke combustion front during in-situ combustion for heavy oil recovery

In-situ combustion (ISC) for heavy oil recovery is a high-risk process and thus calls for a deep understanding of the coke combustion front. However, simulations for describing pore-scale coke combustion are challenging because of the complex combustion dynamics. Recently, some numerical studies on coke combustion in porous media have been carried out and achieved successes, but mainly at macroscopic scales. Therefore, this chapter aims to simulate the combustion process of solid coke in porous media at the pore scale, using the D2Q9 MRT LB model proposed in Sec. 2.2.1.

6.1 Problem description

Coke combustion is investigated in a 2D porous medium, where the reactive coke is deposited on unreactive solid matrices. The compressible hot air containing O_2 and nitrogen (N_2) is injected into such a system by a driving force $\boldsymbol{F} = (F_x, F_y)$. Coke combustion is then assumed to take place at the interface I between coke and hot air as in Eq. (2.28). The CO/CO_2 mole ratio N_p is defined as [132],

$$N_p = A_p \exp\left(-\frac{E_p}{RT}\right), \tag{6.1}$$

where R is the ideal gas constant, T is the local temperature, and A_p and E_p are empirical parameters describing the CO/CO_2 product ratio. The reaction rate F_r is estimated

according to the first-order Arrhenius-type equation as [130],

$$F_r = A\exp\left(-\frac{E}{RT}\right)\frac{Y^I_{O_2}\rho}{M_{O_2}}, \tag{6.2}$$

where A and E are the pre-exponential factor and the activation energy, respectively. As coke burns out gradually, the update of solid geometry is tracked by [47],

$$\partial_t V_c = -S_c V_{cm} F_r. \tag{6.3}$$

where V_c is coke volume, V_{cm} is molar coke volume, and S_c is the reactive surface area.

Governing equations for fluid flow, species evolutions, and heat transfer during coke combustion are described by Eqs. (2.30)-(2.33). By introducing the characteristic length L, velocity U, temperature T_{ch}, and density ρ_{ch}, dimensionless parameters marked by asterisks can be derived as,

$$\begin{aligned} &x^* = \frac{x}{L},\ y^* = \frac{y}{L},\ t^* = \frac{t}{L/U},\ \boldsymbol{u}^* = \frac{\boldsymbol{u}}{U},\ \rho^* = \frac{\rho}{\rho_{ch}},\ T^* = \frac{T}{T_{ch}},\ hr^* = \frac{hr}{M_{O_2}c_{p,g}T_{ch}},\\ &F_r^* = \frac{F_r}{\rho_{ch}U/M_{O_2}},\ A^* = \frac{A}{U},\ \boldsymbol{F}^* = \frac{\boldsymbol{F}}{\rho_{ch}U^2/L},\ \mathrm{Re} = \frac{LU}{\nu},\ \mathrm{Pe}_n = \frac{LU}{D_n},\ \mathrm{Pr} = \frac{\nu}{\alpha_g}, \end{aligned} \tag{6.4}$$

Key characteristic numbers are: the Reynolds number Re, the Peclet number Pe, and the Prandtl number Pr.

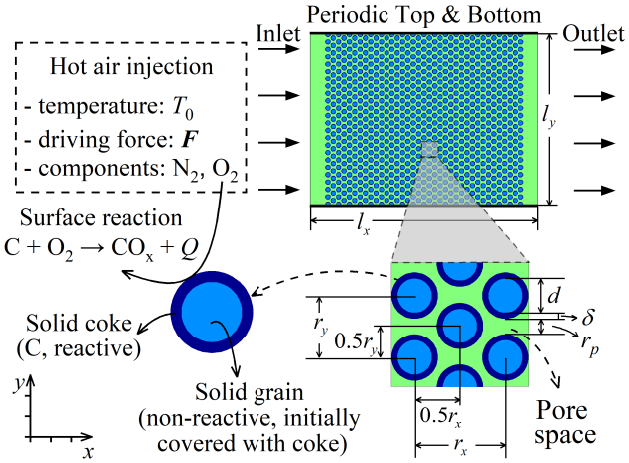

Figure 6.1 The schematic of the problem: Coke combustion in porous media.

A 2D homogeneous structure with length $l_x = 850$ μm and width $l_y = 633.33$ μm is built and illustrated in Fig. 6.1. The porous network contains a staggered array of circular grains with a uniform diameter $d = 15$ μm. Every grain is homogeneously covered by reactive coke with a thickness $\delta = 2.5$ μm. The closest center-to-center distances between two grains in x and y directions are $r_x = 40$ μm and $r_y = 27.5$ μm, respectively. Such a geometric construction leads to the porosity $\phi = 0.443$ and the initial coke volume fraction $\phi_{c,0} = 0.239$. Considering that the injected flow develops along the x direction, the pore size r_p between every two neighboring grains is calculated in the y direction and the volume-averaged value is $\langle r_p \rangle = 7.5$ μm here. This base medium is used for the following combustion simulations, unless otherwise stated. Pore spaces are initially filled with hot N_2 at temperature T_0. The compressible hot air at temperature T_0, density $\rho_{g,0}$, and O_2 mass fractions $Y_{O_2,0}$ ($Y_{N_2,0} = 1.0 - Y_{O_2,0}$) is injected from the inlet to react with coke by a driving force $\boldsymbol{F} = (F_x,\ 0)$. For boundary conditions, zero-gradient conditions are applied for all the scalars at the outlet and the top and bottom are periodic.

In the subsequent simulations, required combustion parameters are set as, $A_p = 3.0 \times 10^8$, $E_p = 251.04$ kJ/mol, $A = 9.717 \times 10^6$ m/s, $E = 131.09$ kJ/mol, $hr = 388.5$ kJ/mol, and $R = 8.314$ J/molK, respectively [10, 164]. During simulations, ρ_g and k_g change with temperature, while other thermophysical properties are assumed to be constant and determined according to the initial temperature [10, 121]. For example, thermophysical properties of the solid (coke and solid grains) and the fluid phases at $T_0 = 773$K are, $\rho_{g,0} = 4.5$ kg/m^3, $c_{p,g} = 1.096$ kJ/kgK, $\alpha_g = 1.14 \times 10^{-5}$ m^2/s, $k_g = 5.64 \times 10^{-2}$ J/smK, $\rho_s/\rho_{g,0} = 556.7$, $c_{p,s}/c_{p,g} = 0.661$, $\alpha_s/\alpha_g = 0.119$, and $k_s/k_g = 43.79$, respectively. In each simulation, the variation in $c_{p,g}$ with burning temperature is less than 10% and thus

$c_{p,g}$ is treated as a constant. The conversion between physical and lattice units is based on a match of the dimensionless parameters in Eq. (6.4), with the characteristic parameters being selected as,

$$L = 0.5r_x, \quad U = \alpha_g/L, \quad \rho_{ch} = \rho_{g,0}, \quad T_{ch} = 3000 \text{ K}. \tag{6.5}$$

A high characteristic temperature T_{ch} is chosen to restrict variations in θ and improve the numerical stability [140]. This chapter focuses on coke combustion dynamics and effects of inlet air and porous structure. Thus, the Reynolds, Prandtl, and Peclet numbers are fixed as (at $T_0 = 773$K), Re $= 1.397$, Pr $= 0.716$, $\text{Pe}_{\text{O}_2} = 1.490$, $\text{Pe}_{\text{CO}_2} = 1.639$, and $\text{Pe}_{\text{CO}} = 1.639$, respectively. Different driving forces, inlet air temperatures, and porous structures are used to change the combustion conditions. Before proceeding further, grid convergence tests have been conducted. A mesh of size $N_x \times N_y = 1020 \times 760$ with lattice resolution 0.833 μm is applied to describe all the porous media in this chapter.

6.2 General coke combustion dynamics

The general dynamics of coke combustion are firstly discussed by a base case with driving force $F_x^* = 6.557$, inlet air temperature $T_0 = 773$ K, and inlet O_2 mass fraction $Y_{\text{O}_2,0} = 0.233$. Figure 6.2 presents the distributions of residual coke and species mass fractions (Y_{O_2} and Y_{CO_2}) at two time instants $t = 3.61$ s and 7.22 s. Note that, fields of Y_{CO} are not provided since they show the same pattern as Y_{CO_2}. In this figure, coke burns out gradually and the combustion front divides the medium into a coke-depleted region and a coke-rich one. Meanwhile, injected O_2 expands in the coke-depleted area and is exhausted at the combustion front, while generated CO_2 from the front prefers

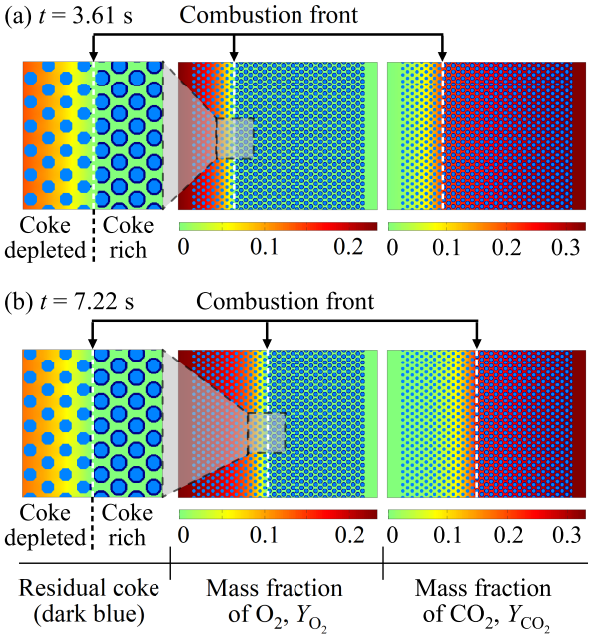

Figure 6.2 Contours of residual coke and species mass fractions (Y_{O_2} and Y_{CO_2}) at time instants $t = 3.61$ s (a) and $t = 7.22$ s (b), for the base case with driving force $F_x^* = 6.557$, inlet air temperature $T_0 = 773$ K, and inlet O_2 mass fraction $Y_{O_2,0} = 0.233$.

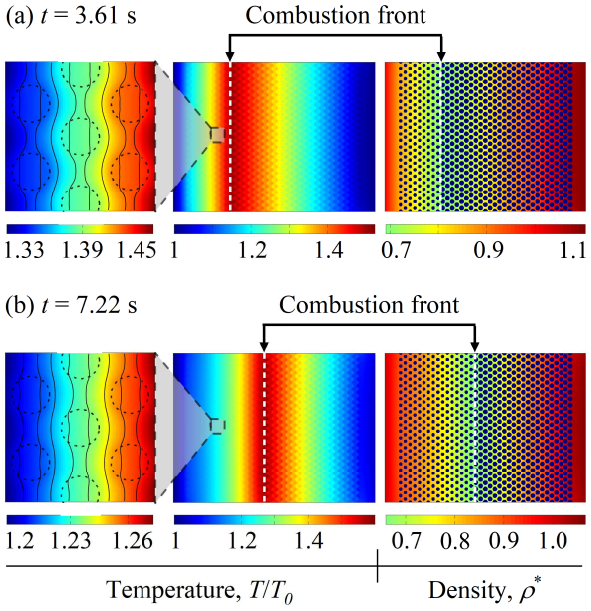

Figure 6.3 Contours of temperature T/T_0 and density ρ^* fields at time instants $t = 3.61$ s (a) and $t = 7.22$ s (b), for the base case with driving force $F_x^* = 6.557$, inlet air temperature $T_0 = 773$ K, and inlet O_2 mass fraction $Y_{O_2,0} = 0.233$. In partially enlarged contours, isotherms and porous geometries are plotted by black and dotted lines, respectively.

to move downstream and accumulate in the coke-rich region. As time goes on, the combustion front propagates from one column of grains to another and advances towards

the outlet, leading to the expansion of the coke-depleted (or O_2-rich) region in the flow direction. The corresponding temperature T/T_0 and density ρ^* fields are illustrated in Fig. 6.3. As can be seen, T/T_0 reaches a peak value near the combustion front, owing to the released combustion heat and the slow heat transfer from the solid phase to the fluid phase ($k_s/k_g = 43.79$). Based on Eq. (2.47), air density is expected to decrease as a consequence of temperature rise. Strong evidence for this prediction is found in Fig. 6.3 that ρ^* drops to a valley value near the combustion front. Propagations of the temperature peak and the density valley are consistent with that of the combustion front. Additionally, the coke-rich region is observed to be slightly hotter than the coke-depleted area, due to the flow direction and the faster heat transfer than the front movement.

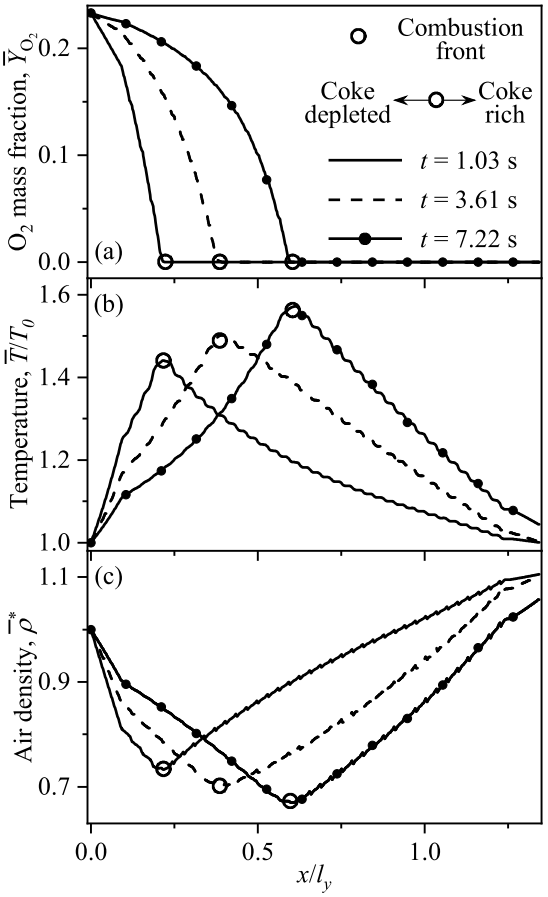

Figure 6.4 Transversely averaged O_2 mass fraction $\overline{Y}_{O_2}$ (a), temperature $\overline{T}/T_0$ (b), and air density $\overline{\rho}^*$ (c), at time instants $t = 1.03$ s, 3.61 s, 7.22 s, for the base case with driving force $F_x^* = 6.557$, inlet air temperature $T_0 = 773$ K, and inlet O_2 mass fraction $Y_{O_2,0} = 0.233$.

To clarify heat transfer details at the pore scale, a partially enlarged view of each temperature contour is provided in Fig. 6.3. Isotherms and porous structures are illustrated by black and dotted lines, respectively. From these enlarged temperature contours, each isotherm is found to be distorted at the solid-fluid interface. This fluctuation in T/T_0 is caused by the different thermophysical properties between the two phases at the pore scale, which cannot be reflected at averaged macroscopic scales. Furthermore, by observing spatial changes in each pair of isotherms, the temperature gradient in the fluid phase ∇T_g is found to be larger than that in the solid phase ∇T_s. This is explained by the fact that heat flux conservation is based on the thermal conductivity k and the larger k results in the smaller temperature gradient ∇T [128]. In this study, k_s is much larger than k_g ($k_s/k_g = 43.79$) and hence $\nabla T_g > \nabla T_s$. Note that, although convection enhances heat transfer in the fluid phase, the fluid velocity is too small to dominate heat transfer in pore-scale porous flows. Thus, compared with macroscopic data, these pore-scale results are more accurate and explicit.

After qualitative observations, Fig. 6.4 plots the transversely averaged O_2 mass fraction $\overline{Y}_{O_2}$, temperature $\overline{T}/T_0$, and density $\overline{\rho}^*$ distributions at three time instants. Curves of $\overline{Y}_{O_2}$ follow a decreasing tendency from the inlet to the combustion front and then remain zero until the outlet, indicating the fully consumed O_2 at the combustion front. Each profile of $\overline{T}/T_0$ is shown to increase from the inlet in the coke-depleted region and decreases from the combustion front in the coke-rich region. In step with temperature variations, $\overline{\rho}^*$ changes non-monotonically along the flow direction. Near the combustion front, $\overline{T}/T_0$ and $\overline{\rho}^*$ are found to reach a maximum and a minimum, respectively. These results quantitatively confirm observations from Figs. 6.2-6.3.

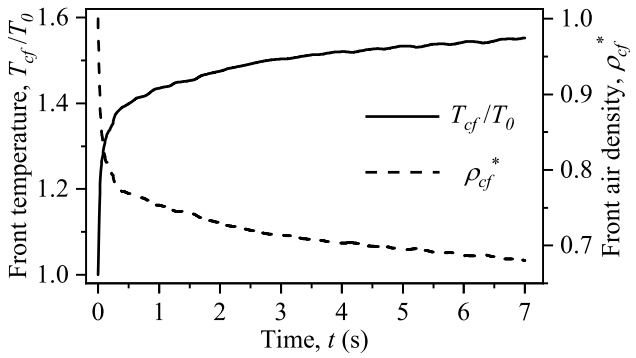

Figure 6.5 Temporal evolutions of front temperature T_{cf}/T_0 and density ρ^*_{cf}, for the base case with driving force $F^*_x = 6.557$, inlet air temperature $T_0 = 773$ K, and inlet O_2 mass fraction $Y_{O_2,0} = 0.233$.

For illustrative purposes, temporal evolutions of front temperature T_{cf}/T_0 and density ρ^*_{cf} are recorded in Fig. 6.5. It shows that there is a dramatic rise in T_{cf}/T_0 at first, implying the start of coke combustion. This increase progressively slows down and T_{cf}/T_0 finally holds an almost constant value at $T_{cf}/T_0 = 1.54$. In the meantime, ρ^*_{cf} drops initially and maintains a nearly stable value at $\rho^*_{cf} = 0.68$ eventually. The significant change in ρ^*_{cf} validates the necessity of the proposed LB model to take thermal expansion effects into account. Besides, the stable burning temperature and density suggest that the system is finally close to a thermal equilibrium state. This is because the heat release and the heat transfer are balanced in the combustion front area. Therefore, with stable burning temperature and fully utilized O_2, the base case is desired in practical applications.

6.3 Effects of thermal expansion and conjugate heat transfer

It is noteworthy that the proposed LB model with temperature-dependent density (or thermal expansion effects) is different from existing investigations [10, 132] with density being fixed as a constant. In addition, the derived source term F_{q2} is included to satisfy conjugate heat transfer conditions, which avoids the iteration procedure in [10]. Note that, for char-pellet combustion in [132], the temperature variation is very small so that the

thermal expansion and the source term F_{q2} for conjugate heat transfer are not necessary. In order to demonstrate the significance of including these two factors in the present study, the base case is simulated again by the developed LB model but without thermal expansion (case LBA) or conjugate heat transfer (case LBB).

Contours of temperature T/T_0, residual coke, O_2 mass fraction Y_{O_2}, and reaction rate F_r^* for cases LBA-LBB at time instant $t = 2.061$ s are shown in Figs. 6.6(a)-(b). By comparison, evident differences are detected between temperature fields in the base case (Fig. 6.3) and these two cases. First, in case LBA (Fig. 6.6(a)), temperature in the coke-rich region is obviously higher than that in the coke-depleted area. Thus, compared with the base case, more reaction heat is transported downstream from the combustion front, leading to the under-predicted T_{cf}/T_0. Second, in case LBB (Fig. 6.6(b)), the coke-rich area is fairly uniform and hot. By comparing isotherms, case LBB demonstrates larger temperature gradient in the solid phase than in the fluid phase ($\nabla T_s > \nabla T_g$), which is opposed to both the base case and case LBA with $\nabla T_g > \nabla T_s$. This is the direct consequence of ignoring F_{q2} and conserving heat flux based on the thermal diffusivity α ($\alpha_s/\alpha_g = 0.119$) instead of the thermal conductivity k ($k_s/k_g = 43.79$) [128]. Therefore, case LBB predicts the faster heat transfer in the fluid phase than in the solid phase, which results in $\nabla T_s > \nabla T_g$. With this inappropriate treatment in case LBB, most of the reaction heat transfers downstream from the combustion front and thus T_{cf}/T_0 increases negligibly. Besides, from the coke and F_r^* distributions in Fig. 6.6, the low burning temperature in LBB causes the inefficient coke consumption and the wide combustion front area, which is unrealistic in practical applications. These observations are quantitatively verified by transversely averaged profiles of O_2 mass fraction $\overline{Y}_{O_2}$ and temperature $\overline{T}/T_0$ in Fig. 6.6(c).

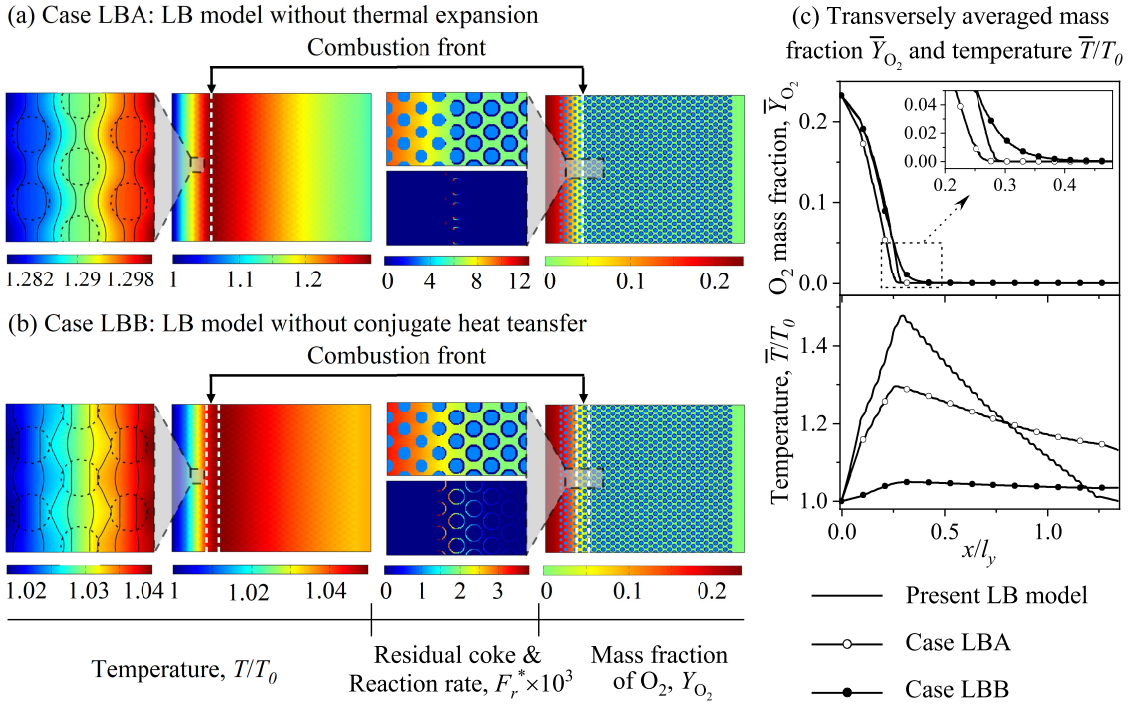

Figure 6.6 Contours of temperature T/T_0, O_2 mass fraction Y_{O_2}, residual coke, and reaction rate F_r^* fields for Case LBA (a) and Case LBB (b), as well as transversely averaged O_2 mass fraction $\overline{Y}_{O_2}$ and temperature $\overline{T}/T_0$ (c) at time instant $t = 2.061$ s, with driving force $F_x^* = 6.557$, inlet air temperature $T_0 = 773$ K, and inlet O_2 mass fraction $Y_{O_2,0} = 0.233$. Isotherms and porous geometries are plotted by black and dotted lines, respectively.

For better comparison, temporal evolutions of combustion dynamics are recorded in Fig. 6.7 along with those for the base case, including the front temperature T_{cf}/T_0, density ρ_{cf}^*, position l_{cf}/l_x, and the residual coke ratio $R_{rc} = \phi_c/\phi_{c,0}$ (ϕ_c is the coke volume fraction at a given time). From curves in Figs. 6.7(a)-(b), variations in T_{cf}/T_0 and ρ_{cf}^* are underestimated in cases LBA and LBB, which quantitatively verify observations from Fig. 6.6. In case LBA, air density is fixed as $\rho_{g,0}$ and the increase in T_{cf}/T_0 is undervalued. As an illustration, the increase rate of T_{cf}/T_0 (calculated as $T_{cf}/T_0 - 1$) drops by 38% from the base case (from 0.5 to 0.31) at $t = 3$ s. Furthermore, in case LBB, the conjugate heat transfer conditions (Eq. (2.36)) are not satisfied, thereby causing an obvious reduction in T_{cf}/T_0. With such an underestimation, the decrease in ρ_{cf}^* is under-predicted as well. Specifically, compared with the base case, the ascent rate of T_{cf}/T_0 and the drop rate of

ρ^*_{cf} (calculated as $1-\rho^*_{cf}$) at $t=3$ s decrease by 88% (from 0.5 to 0.06) and 89.7% (from 0.29 to 0.03), respectively. On the other hand, by comparing results in Figs. 6.7(c)-(d), the undervalued T_{cf}/T_0 in case LBA or case LBB is found to decelerate coke consumption and front propagation. Note that, the combustion intensity in case LBB is less affected than that in case LBA, indicating the importance of including thermal expansion effects.

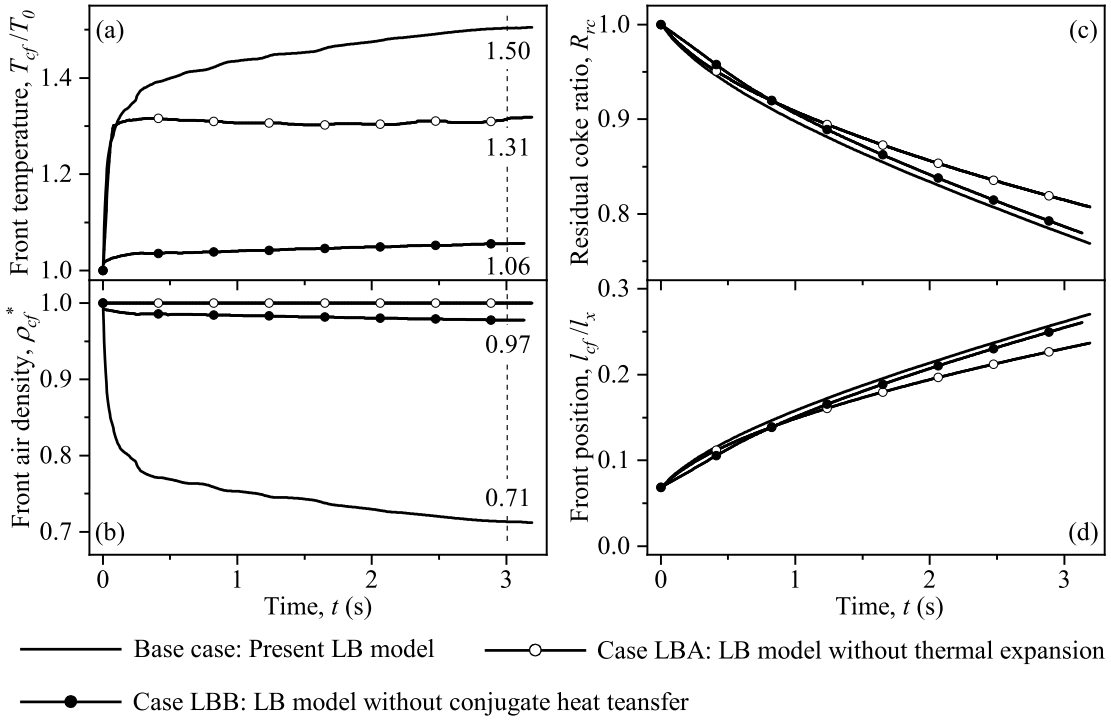

Figure 6.7 Temporal evolutions of front temperature T_{cf}/T_0 (a), front density ρ^*_{cf} (b), residual coke ratio R_{rc} (c), and front position l_{cf}/l_x (d), for cases with driving force $F^*_x=6.557$, inlet air temperature $T_0=773$ K, and inlet O_2 mass fraction $Y_{O_2,0}=0.233$. Results of different models are shown with markers.

These results suggest that, for coke combustion simulations, LB models without considering thermal expansion effects or conjugate heat transfer will under-predict both the increase in burning temperature and the decrease in air density. As a result, combustion intensity or front area may be predicted inaccurately. This underestimation even incorrectly introduces a stable burning temperature under high driving force, which is clarified in

Sec. 6.4.2. The importance of including both thermal expansion effects and conjugate heat transfer in the present LB model for coke combustion is therefore confirmed.

6.4 Parametric study

After the above combustion dynamics study, a series of simulation tests are conducted to elucidate the key factors influencing coke combustion. As mentioned in the introduction section, a stable combustion front, with high propagation velocity, proper front temperature, and full O_2 utilization, is critical to a successful ISC process. Thus, to quantify sensitivities of the combustion front, temporal evolutions of the front temperature T_{cf}/T_0, density ρ^*_{cf}, and location l_{cf}/l_x are recorded. In addition, the volume-averaged reaction rate $\langle F^*_r \rangle$ and the residual coke ratio R_{rc} are measured during combustion.

6.4.1 Inlet air temperature T_0

As temperature plays a major role in the reaction rate (Eq. (6.2)) and the fluid density (Eq. (2.47)), effects of inlet air temperature T_0 on coke combustion are firstly evaluated. Three tests with driving force $F^*_x = 6.557$, inlet O_2 mass fraction $Y_{O_2,0} = 0.233$, and $T_0 = 600$ K, 650 K, 1000 K are carried out. Figure 6.8 compares combustion dynamics with those from the base case ($T_0 = 773$ K) quantitatively. Note that, owing to variations in T_0, temporal evolutions of both the front temperature T_{cf} and the normalized one T_{cf}/T_0 are provided. From Figs. 6.8(a)-(c), curves for each T_0 show a similar pattern: T_{cf} experiences a steep rise and ρ^*_{cf} drops sharply at first, and both of these two parameters reach stable burning values at last. It suggests that all these cases reach thermal equilibrium states finally. In addition, corresponding to the increase in T_0, there is a gradual rise in the

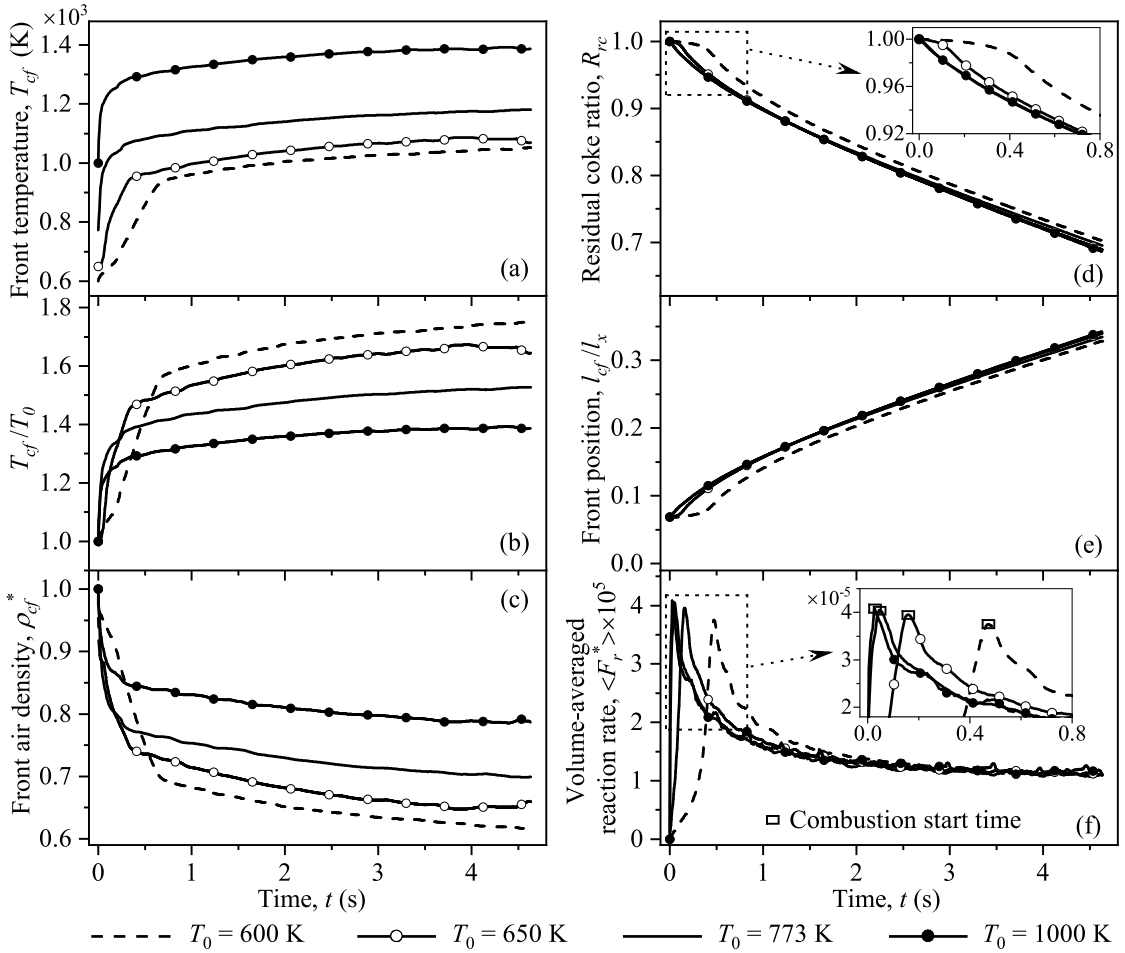

Figure 6.8 Temporal evolutions of front temperature T_{cf} (a) and T_{cf}/T_0 (b), front density ρ^*_{cf} (c), residual coke ratio R_{rc} (d), front position l_{cf}/l_x (e), and volume-averaged reaction rate $\langle F^*_r \rangle$ (f), for cases with driving force $F^*_x = 6.557$, inlet O_2 mass fraction $Y_{O_2,0} = 0.233$, and inlet air temperature $T_0 = 600$ K, 650 K, 773 K, 1000 K.

value of T_{cf} but a decline in the normalized T_{cf}/T_0. Driven by the relationship between temperature and density in Eq. (2.47), the decrease rate of ρ^*_{cf} from $\rho^*_{cf} = 1$ slows down under ascending T_0. Moreover, Figs. 6.8(d)-(e) reveal that, as combustion goes on in each test, the residual coke ratio R_{rc} decreases and the front position l_{cf}/l_x propagates towards the outlet ($l_{cf}/l_x = 1$). Regarding effects of T_0 on R_{rc} and l_{cf}/l_x, two stages are identified.

Firstly, during the initial period of about $0 \leq t \leq 0.7$ s in Figs. 6.8(d)-(e), increasing T_0 brings in smaller R_{rc} and larger l_{cf}/l_x, indicating the positive role of high T_0 in coke combustion. This stems from the fact that increasing T_0 results in the higher front temper-

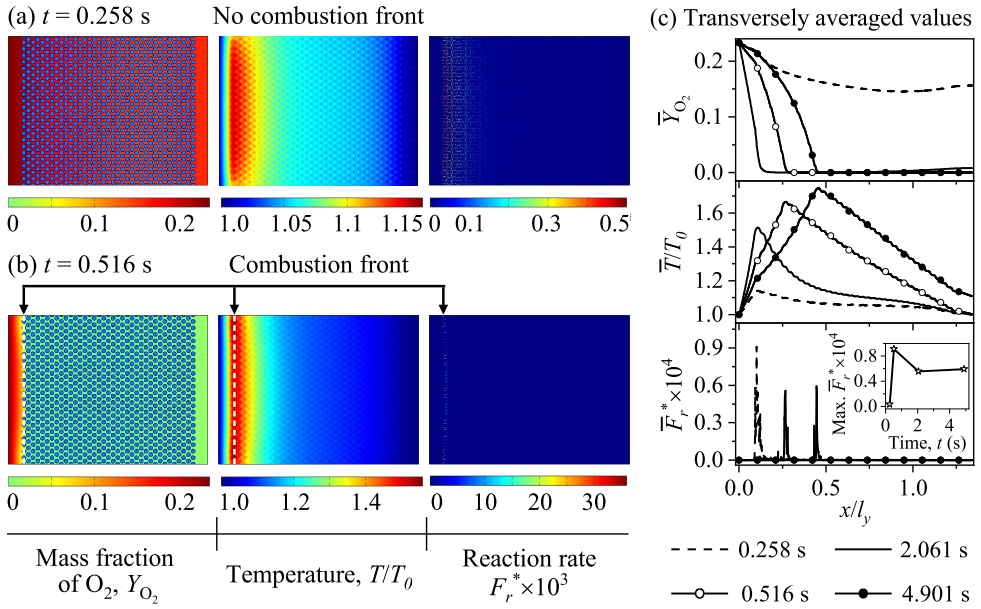

Figure 6.9 Contours of O_2 mass fraction Y_{O_2}, temperature T/T_0, and reaction rate F_r^* fields at time instants $t = 0.258$ s (a) and $t = 0.516$ s (b), for the case with driving force $F_x^* = 6.557$, inlet air temperature $T_0 = 600$ K, and inlet O_2 mass fraction $Y_{O_2,0} = 0.233$. Transversely averaged values of these three parameters are provided at time instants $t = 0.258$ s, 0.516 s, 2.061 s, 4.901 s (b). Inset plot: The maximum $\overline{F_r}^*$ at each time instant.

ature T_{cf} (Fig. 6.8(a)), the quicker reaction rate $\langle F_r^* \rangle$ (Fig. 6.8(f)), and subsequently the more intensive coke combustion. Such promoting influence of increasing T_0 is constrained by a critical value at about $T_0 = 773$K in this study, reasons of which will be explained below. Besides, each profile of $\langle F_r^* \rangle$ accelerates sharply at first until a peak value, implying the start of combustion. In cases with lower T_0, the combustion start period lasts longer because T_{cf} and $\langle F_r^* \rangle$ ascend more slowly. To determine the impact of the delayed ignition, fields of O_2 mass fraction Y_{O_2}, temperature T/T_0, reaction rate F_r^*, and the transversely averaged values for the case with $T_0 = 600$ K are given in Fig. 6.9. Results at $t = 0.259$ s show that no combustion front appears and the reaction zone with a slight temperature rise spans extensively. F_r^* is relatively small and the supply of O_2 exceeds the consumption rate, leading to O_2 leakage. As time goes on, the local temperature (also the local reaction rate) increases to a critical value to trigger coke combustion. Taking contours at $t = 0.516$ s as

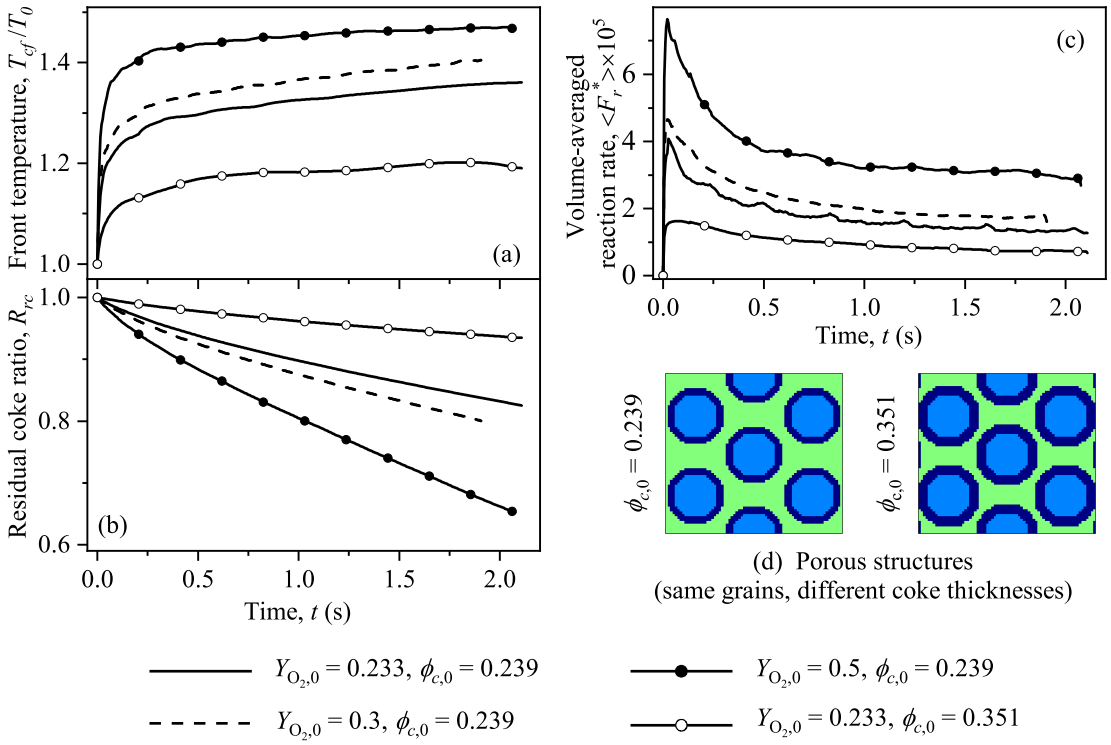

Figure 6.10 Temporal evolutions of front temperature T_{cf}/T_0 (a), residual coke ratio R_{rc} (b), and volume-averaged reaction rate $\langle F_r^* \rangle$ (c), for cases with driving force $F_x^* = 6.557$, inlet air temperature $T_0 = 1000$ K, inlet O_2 mass fraction $Y_{O_2,0} = 0.233$, 0.3, 0.5, and initial coke volume fraction $\phi_{c,0} = 0.239$, 0.351. Porous structures with different $\phi_{c,0}$ are provided (d).

an example, a combustion front arises and both T/T_0 and F_r^* increase significantly at this front. As a result, injected O_2 is fully consumed before the combustion front. Thus, in this case ($T_0 = 600$ K) with delayed ignition, although combustion dynamics become similar to the base case after ignition, the initial O_2 leakage may create safety risks, implying the necessity for an appropriate T_0 in industrial applications.

Secondly, during the late stage of about $t \geq 0.7$ s in Figs. 6.8(d)-(e), profiles of R_{rc} and l_{cf}/l_x for different values of T_0 evolve almost identically. It suggests that, once combustion starts, the promoting effects of ascending T_0 on coke combustion become negligible. This tendency is somewhat counterintuitive, given the fact that T_{cf} remains larger with higher T_0 in Fig. 6.8(a). Possible causes are the insufficient amount of coke or O_2 for combustion. To examine these two factors, three tests are further performed. Based on the case with

$T_0 = 1000$ K in Fig. 6.8, such three tests increase the inlet O_2 mass fraction ($Y_{O_2,0} = 0.3$, 0.5) and the initial coke volume fraction ($\phi_{c,0} = 0.351$), respectively. The case with $T_0 = 1000$ K is selected because the positive influence of this high T_0 is limited even during the initial period. Calculated combustion dynamics for these three tests are provided in Fig. 6.10, along with results of the reference case ($T_0 = 1000$ K in Fig. 6.8). As can be see, with ascending $Y_{O_2,0}$ or descending $\phi_{c,0}$, the front temperature T_{cf}/T_0 in Fig. 6.10(a) and the volume-averaged reaction rate $\langle F_r^* \rangle$ in Fig. 6.10(c) increase, hence the decreased residual coke ratio R_{rc} in Fig. 6.10(b) and the enhanced coke combustion. It is thus the O_2-limited factor that inhibits promoting effects of increasing T_0 on coke combustion.

The above results demonstrate that T_0 should be large enough to ensure efficient ignition and to avoid harmful O_2 leakage. In terms of economic considerations however, there is no need to increase T_0 without limits since O_2 is insufficient and effects of ascending T_0 become insignificant after the start of coke combustion.

6.4.2 Driving force F_x^*

As discussed above, sufficient O_2 should be injected to sustain coke combustion, so the driving force F_x^* that affects the air injection rate is investigated. Three tests with inlet air temperature $T_0 = 773$ K, inlet O_2 mass fraction $Y_{O_2,0} = 0.233$, and $F_x^* = 3.278$, 9.835, 13.114 are performed. Temporal evolutions of front temperature T_{cf}/T_0 and position l_{cf}/l_x, volume-averaged reaction rate $\langle F_r^* \rangle$, and residual coke ratio R_{rc} from these three tests are provided and compared with the base case ($F_x^* = 6.557$) in Fig. 6.11. By comparison, even though combustion dynamics in each of the three tests are similar to those in the base case, increasing F_x^* accelerates coke combustion obviously. This can be explained by the fact that, in cases with higher F_x^*, more O_2 is injected to react with coke and thus

more combustion heat is released to increase T_{cf}. The sufficient O_2 together with the high T_{cf} lead to the fast reaction rate $\langle F_r^* \rangle$ and the intensified coke combustion. As for the thermal state at the combustion front, each case is observed to reach a thermal equilibrium finally, except for the one with $F_x^* = 13.114$. Under such a high injection force, there is a continuous rise in T_{cf} as well as $\langle F_r^* \rangle$. It happens because the amount of reaction heat generated at the combustion front cannot be balanced by that transported away from the front. Additionally, the intense coke combustion driven by $F_x^* = 13.114$ gives rise to a noticeable front temperature rise from $T_{cf} = T_0$ to $T_{cf} = 2T_0$ within $t \approx 4$ s, which is definitely unfavourable in practical applications.

Three tests are added to explore alternative approaches for reducing the negative influence of high F_x^*. Specifically, the case with $F_x^* = 13.114$ in Fig. 6.11 is simulated again, but its inlet O_2 mass fraction and temperature are decreased to $Y_{O_2,0} = 0.167$, 0.1

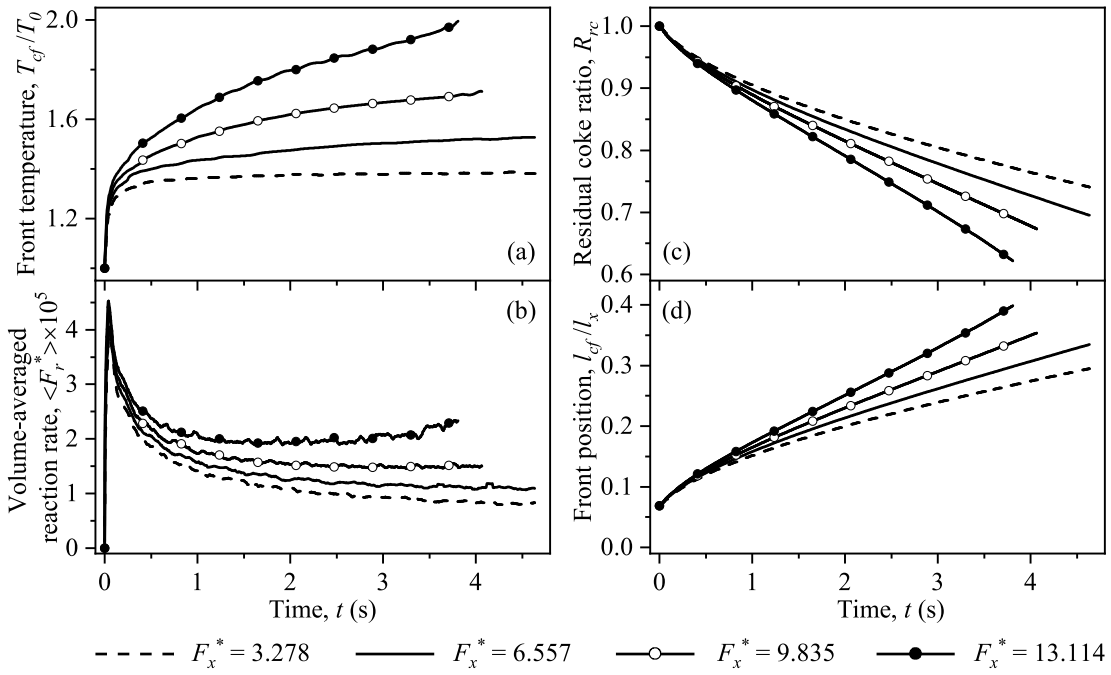

Figure 6.11 Temporal evolutions of front temperature T_{cf}/T_0 (a), volume-averaged reaction rate $\langle F_r^* \rangle$ (b), residual coke ratio R_{rc} (c), and front position l_{cf}/l_x (d), for cases with inlet air temperature $T_0 = 773$ K, inlet O_2 mass fraction $Y_{O_2,0} = 0.233$, and driving force $F_x^* = 3.278$, 6.557, 9.835, 13.114.

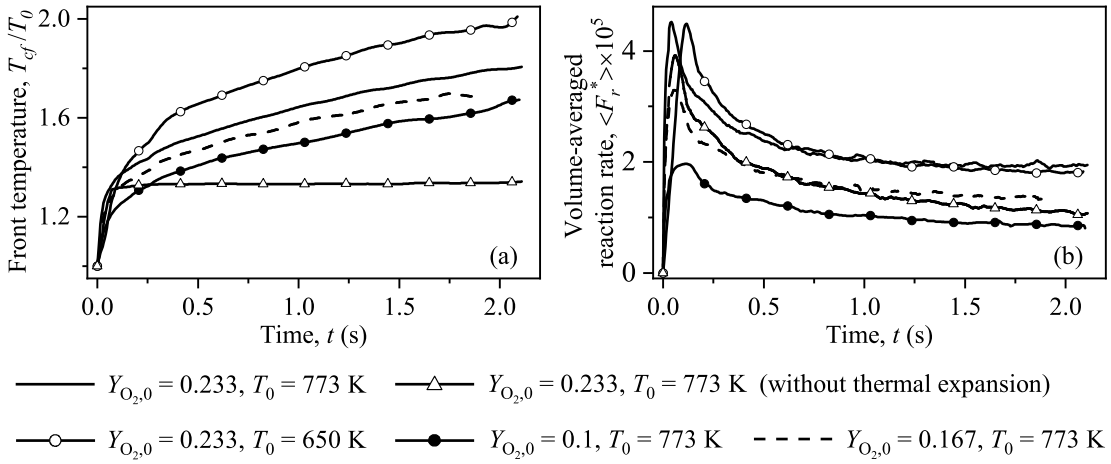

Figure 6.12 Temporal evolutions of front temperature T_{cf}/T_0 (a), and volume-averaged reaction rate $\langle F_r^* \rangle$ (b), for cases with driving force $F_x^* = 13.114$, inlet air temperature $T_0 = 650$ K, 773 K, and inlet O_2 mass fraction $Y_{O_2,0} = 0.1$. 0.167, 0.233.

and $T_0 = 650$ K, respectively. Combustion dynamics of these three tests as well as the reference case ($F_x^* = 13.114$ in Fig. 6.11) are provided in Fig. 6.12. It is shown that curves of both T_{cf}/T_0 and $\langle F_r^* \rangle$ follow similar patterns in the four cases. Despite changes in $Y_{O_2,0}$ and T_0, T_{cf}/T_0 keeps increasing during coke combustion, indicating the thermal non-equilibrium. Furthermore, in the case with $T_0 = 650$ K, T_{cf} increases twice as high as T_0 within $t \approx 2$ s. Thus, under such a high injection force $F_x^* = 13.114$, it is difficult to obtain a stable burning temperature by merely modifying the inlet air components or temperature. In the meantime, for the purpose of model testing, the reference case ($F_x^* = 13.114$ in Fig. 6.11) is simulated by the LB model proposed in Sec. 2.2.1 but without thermal expansion. From profiles in Fig. 6.12, it is clear that such an LB model (black lines with triangles) under-predicts both T_{cf}/T_0 and $\langle F_r^* \rangle$ compared with the proposed LB model (black lines). As discussed in Sec. 6.3, this is because most of the reaction heat will be transported downstream from the combustion front if thermal expansion is not taken into account. Moreover, the underestimation in T_{cf}/T_0 makes the system reach a false thermal equilibrium state, implying that the influence of high driving force $F_x^* = 13.114$

cannot be properly captured. These results confirm the significance of considering thermal expansion effects in the present LB model.

In general, the high driving force F_x^* enhances coke combustion and accelerates combustion front propagation. However, F_x^* should be constrained below a critical value because an unlimited increase in F_x^* introduces a dramatic and harmful rise in front temperature.

6.4.3 Porous structure

In the above simulations, distributions of coke and solid grains remain homogeneous and only one porosity $\phi = 0.443$ is considered. In practical applications however, ϕ varies among different underground sites and coke and solid matrices usually distribute heterogeneously. Attention is therefore turned to the influence of porous structure on coke combustion, including medium porosity, coke distribution, and solid matrix structure. As constructed in Fig. 6.13(e), six media PA-PF are considered. They share the same domain size ($l_x = 850$ μm, $l_y = 633.33$ μm) and initial coke volume fraction $\phi_{c,0} = 0.239$ with the base medium in Fig. 6.1. However, they vary in grain diameter d, coke thickness δ, and grain distribution (r_x, r_y) to generate different porosities ϕ (PA-PB), heterogeneous coke distributions (PC-PD), and random matrix structures (PD-PF), respectively. Specifically, media PA-PE consist of regularly-distributed grains with uniform (PA-PC) or random (PD-PE) diameters; while medium PF is composed of randomly-located grains with random diameters. More details about the construction of random grain diameters or distributions can be found in Sec. 3.4. Geometrical parameters for media PA-PF are provided in Table 6.1. The above base case with driving force $F_x^* = 6.557$, inlet air temperature $T_0 = 773$ K, and inlet O_2 mass fraction $Y_{O_2,0} = 0.233$ is simulated in media PA-PF separately.

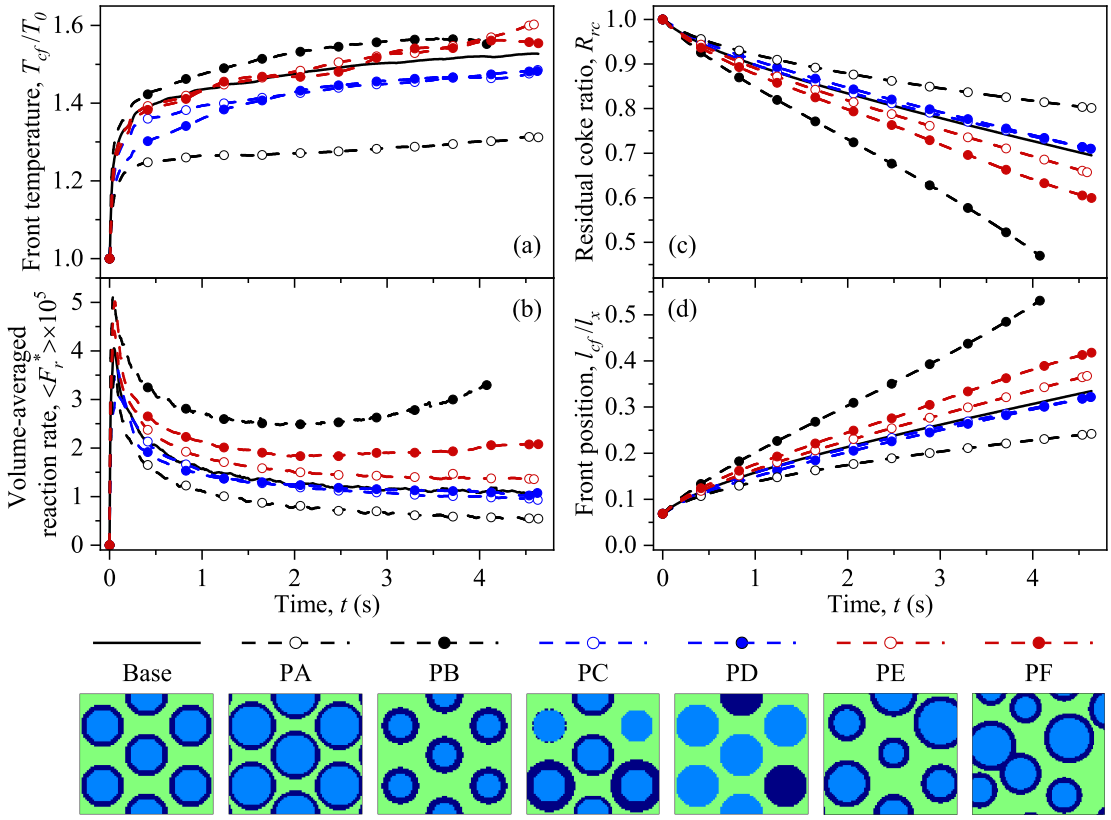

(e) Porous medium structures (same coke volume fraction)

Figure 6.13 Temporal evolutions of front temperature T_{cf}/T_0 (a), volume-averaged reaction rate $\langle F_r^* \rangle$ (b), residual coke ratio R_{rc} (d), and front position l_{cf}/l_x (d) in media PA-PF and the base medium, with driving force $F_x^* = 6.557$, inlet air temperature $T_0 = 773$ K, and inlet O_2 mass fraction $Y_{O_2,0} = 0.233$. Porous medium structures are provided (e).

Figures 6.13(a)-(d) provide temporal evolutions of front temperature T_{cf}/T_0 and position l_{cf}/l_x, volume-averaged reaction rate $\langle F_r^* \rangle$, and residual coke ratio R_{rc}. Results from media PA-PB and the base medium are firstly compared to demonstrate effects of medium porosity. By comparison, ascending porosity ϕ is found to significantly intensify coke combustion (Fig. 6.13(c)) and front propagation (Fig. 6.13(d)). It is supported by the fact that, in a medium with large ϕ, the fluid mobility increases and the flow rate (also the injected air flux) accelerates. Similar to cases with high driving force F_x^* in Fig. 6.11, the enhanced injection flow subsequently leads to an obvious increase in both T_{cf}/T_0 and $\langle F_r^* \rangle$ (Figs. 6.13(a)-(b)), indicating the improved coke combustion. What differs from the high F_x^* condition is that, in medium PB with large ϕ, $\langle F_r^* \rangle$ keeps increasing but T_{cf}/T_0

Table 6.1 Porous media parameters.

Parameters	Porous media ($\phi_{c,0} = 0.239$)						
	Base	PA	PB	PC	PD	PE	PF
ϕ	0.443	0.285	0.586	0.443	0.443	0.443	0.443
d (μm)	15.0	18.3	10.8	15.0	0 or 20.0	[10, 22.5]	[10, 26.3]
$\overline{d}$ (μm)	15.0	18.3	10.8	15.0	15.0	16.5	20.3
δ (μm)	2.5	2.0	3.0	[0, 4.6]	0 or 20.0	2.9	3.4
$\overline{\delta}$ (μm)	2.5	2.0	3.0	2.5	2.5	2.9	3.4
r_x (μm)	40.0	40.0	40.0	40.0	40.0	48.3	56.7
r_y (μm)	27.5	27.5	27.5	27.5	27.5	31.7	35.8
$\langle r_p \rangle$ (μm)	7.5	5.2	10.7	7.5	7.5	9.4	10.0

gradually reaches a stable value during combustion, suggesting the thermal balance. These results help to draw a conclusion that, to obtain a stable combustion front with improved sweeping velocity, it is better to increase the medium porosity than the driving force.

In order to clarify combustion details in media PA and PB, fields of residual coke, O_2 mass fraction Y_{O_2}, and temperature T/T_0 at time instant $t = 2.577$ s are presented in Fig. 6.14. As can be seen, combustion dynamics in media PA-PB are generally consistent with those in the base medium (Figs. 6.2-6.3), except that temperature fields on the coke-rich side expand more uniformly in these two media than in the base one. Moreover, this observation is quantitatively confirmed by the calculated transversely averaged temperature $\overline{T}/T_0$ in Fig. 6.15(a). There are two causes for such an inconsistency in temperature distributions. First, in PA, the combustion front moves slowly and stays for a long time in one place, resulting in the long heat transfer time from the combustion front. Second, in PB, the enhanced flow rate promotes the heat transfer velocity from the combustion front. Compared with the base case, both of these two factors contribute to the result that more

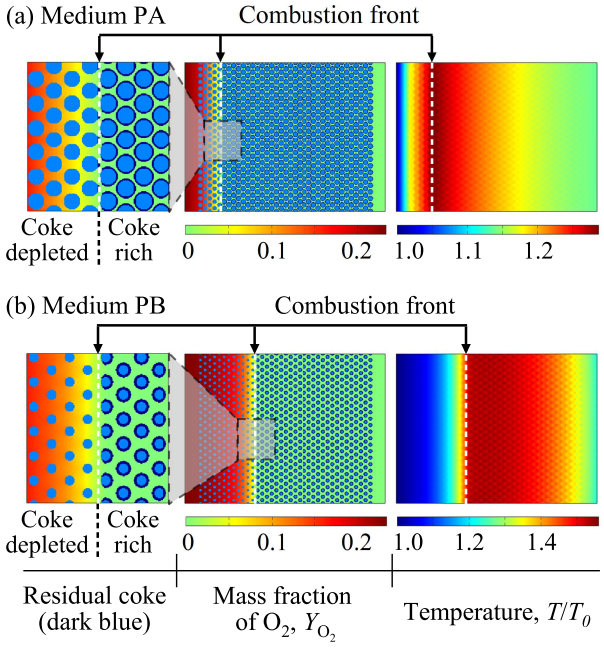

Figure 6.14 Contours of residual coke, O_2 mass fraction Y_{O_2}, and temperature T/T_0 fields at time instant $t = 2.577$ s in media PA (a) and PB (b), for the case with driving force $F_x^* = 6.557$, inlet air temperature $T_0 = 773$ K, and inlet O_2 mass fraction $Y_{O_2,0} = 0.233$.

heat is transferred away from the combustion front, thus the more uniform temperature fields on the coke-rich side in media PA and PB.

Based on results in Figs. 6.13(a)-(d), combustion dynamics from media PC-PD are then compared with those from the base medium to illustrate the impact of random coke distributions. Even though curves of T_{cf}/T_0 for media PC-PD are slightly below the base one, profiles of $\langle F_r^* \rangle$, R_{rc}, and l_{cf}/l_x in these three media overlap each other, suggesting no significant difference in their overall combustion dynamics. The discrepancy in T_{cf}/T_0 is attributed to the variable local temperature along the combustion front, which will be explained below. For better comparison, Fig. 6.16 depicts distributions of residual coke, O_2 mass fraction Y_{O_2}, and temperature T/T_0 in media PC-PD at time instant $t = 2.577$ s. It shows that, as in the base medium (Figs. 6.2-6.3), injected O_2 is fully consumed and the temperature reaches its peak value at the combustion front in each of these two media. As regards combustion details at the pore scale however, results in media PC-PD are different

from those in the base medium from two perspectives. First, the combustion front in both PC and PD proceeds in a curve-like pattern along the x direction, instead of keeping flat as in the base case. Second, local temperature varies along the combustion front in PC-PD, while it remains almost uniform in the base case. These differences are mainly introduced by the heterogeneous coke distributions in media PC-PD at the pore scale.

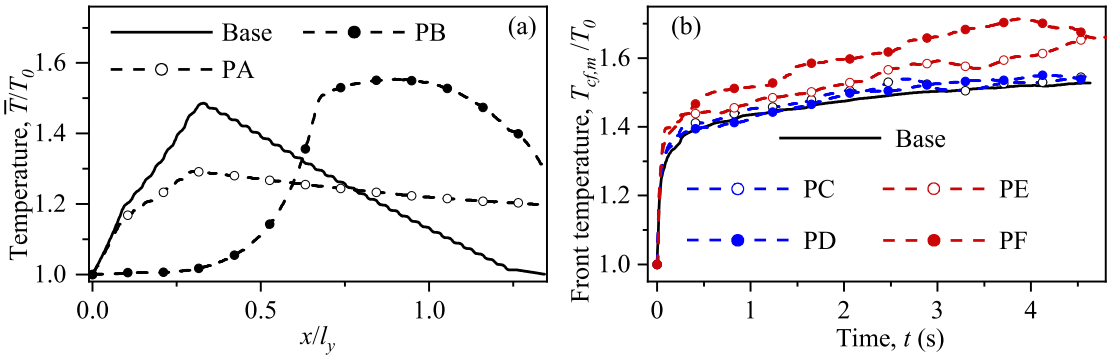

Figure 6.15 Transversely averaged temperature $\overline{T}/T_0$ at time instant $t = 2.577$ s in media PA-PB and the base one (a) and temporal evolutions of maximum front temperature $T_{cf,m}/T_0$ in media PC-PF and the base one (b), for cases with driving force $F_x^* = 6.557$, inlet air temperature $T_0 = 773$ K, and inlet O_2 mass fraction $Y_{O_2,0} = 0.233$.

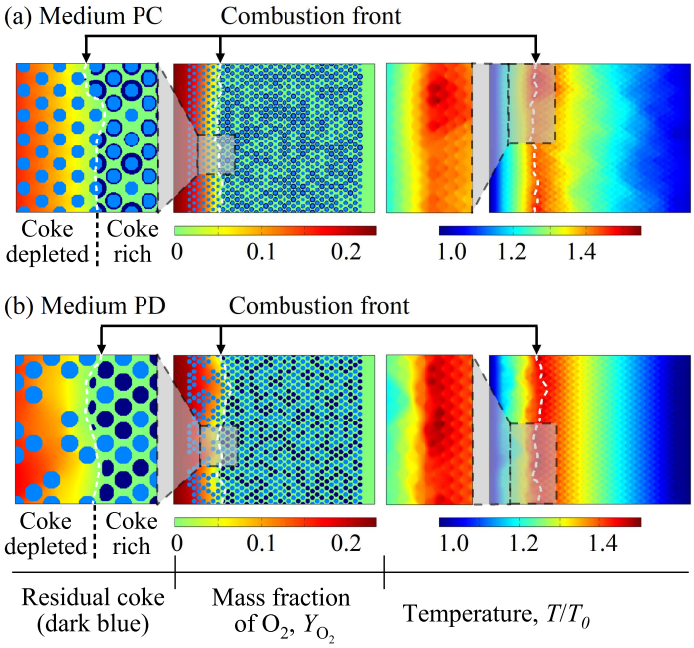

Figure 6.16 Contours of residual coke, O_2 mass fraction Y_{O_2}, and temperature T/T_0 fields at time instant $t = 2.577$ s in media PC (a) and PD (b), for the case with driving force $F_x^* = 6.557$, inlet air temperature $T_0 = 773$ K, and inlet O_2 mass fraction $Y_{O_2,0} = 0.233$.

Besides, by recording temporal evolutions of the maximum front temperature $T_{cf,m}/T_0$ in Fig. 6.15(b), results for media PC-PD and the base medium are observed to be almost identical. Combined with the variations in T/T_0 along the combustion front (Fig. 6.16), this finding explains the above observation that curves of the averaged T_{cf}/T_0 along the combustion front in media PC-PD are slightly less than the base one (Fig. 6.13(a)). Moreover, results in Fig. 6.15(b) explicates the similar combustion intensity between media PC-PD and the base medium (Fig. 6.13(b)-(d)). It is therefore appropriate to reflect the combustion dynamics by the local burning temperature $T_{cf,m}/T_0$ instead of the averaged one T_{cf}/T_0, indicating that the present pore-scale results are more precise than upscalling ones. Results from media PC-PD demonstrate that the irregular coke distribution influences combustion details at the pore scale, but it plays an insignificant role in the overall coke combustion in the present study.

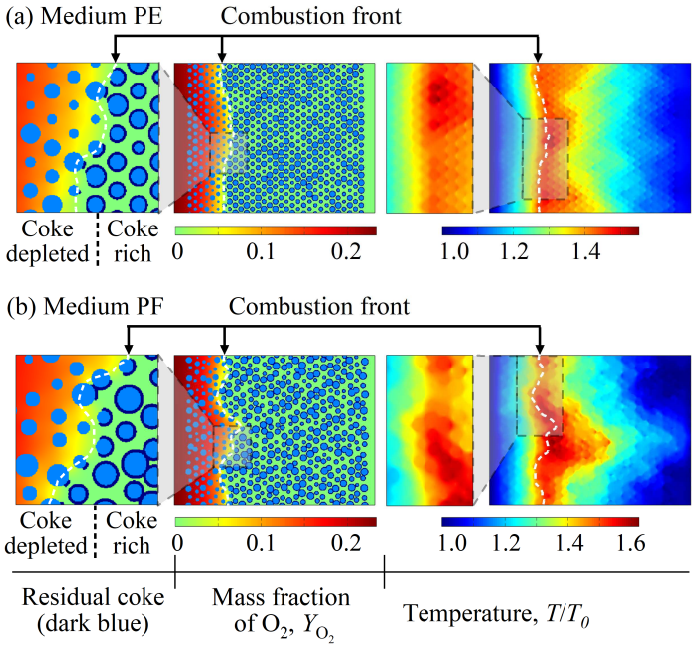

Figure 6.17 Contours of residual coke, O_2 mass fraction Y_{O_2}, and temperature T/T_0 fields at time instant $t = 2.577$ s in media PE (a) and PF (b), for the case with driving force $F_x^* = 6.557$, inlet air temperature $T_0 = 773$ K, and inlet O_2 mass fraction $Y_{O_2,0} = 0.233$.

To further examine the role of matrix structure heterogeneity, combustion properties in media PD-PF are analyzed. Profiles of $\langle F_r^* \rangle$, R_{rc}, and l_{cf}/l_x in Figs. 6.13(b)-(d) suggest that, compared with the base case, coke combustion in medium PD show a similar intensity, while combustion and front propagation are accelerated in media PE and PF, with the most intensive combustion taking place in PF. This can be explained by the measured volume-averaged pore size $\langle r_p \rangle$ in Table 6.1. The data shows that $\langle r_p \rangle$ remains the smallest in medium PD and the base medium, while it increases in medium PE and becomes the largest one in medium PF. As reported in [63], although with fixed porosity, the larger pore size exerts the smaller resistance and then the faster fluid flow. Therefore, heterogeneous matrix structures of media PE-PF introduce large pore size and finally lead to the enhanced flow and the improved coke combustion. Such effects again fail to be reflected by profiles of T_{cf}/T_0 (Figs. 6.13(a)) due to variations in T/T_0 along the combustion front (Fig. 6.17). As conducted above, temporal evolutions of the maximum front temperature $T_{cf,m}/T_0$ in media PD-PF are measured and provided in Fig. 6.15(b). With the increase in $\langle r_p \rangle$ from PD to PF, the value of $T_{cf,m}/T_0$ grows gradually, matching well with the enhanced combustion. Moreover, as in media PC-PD, snapshots of combustion dynamics in Fig. 6.17 indicate that heterogeneous structures of media PE-PF affect pore-scale details of coke combustion.

These assessments show that a medium with large porosity is desired to achieve a combustion front with high movement velocity and proper burning temperature. The heterogeneity in both coke distribution and matrix structure has notable effects on pore-scale combustion details. Moreover, the heterogeneous matrix structure may change the medium pore size and then influence the overall combustion intensity.

6.5 Summary

Coke combustion is simulated in porous media at the pore scale, using the newly developed MRT LB model in Sec. 2.2.1. Advantages of the present new model are highlighted by simulating a base case of pore-scale coke combustion. The results show that previous models without considering thermal expansion or conjugate heat transfer underestimate front temperature and coke combustion. Such models incorrectly predict a stable burning temperature under a high driving force. On the contrary, the proposed LB model is able to overcome these deficiencies and capture coke combustion dynamics in the base case: 1) As combustion goes on, a stable combustion front sweeps downstream fluid efficiently. 2) At this front, temperature reaches a local maximum, density drops to a local minimum, and reactants (coke and O_2) are fully consumed. 3) Temperature fluctuates at the solid-fluid interface because these two phases have different thermophysical properties at the pore scale, indicating that the present pore-scale results are more precise and detailed than upscaling studies.

The developed LB model is also employed to conduct a detailed parametric study, which demonstrates that: 1) The increased inlet air temperature facilitates reliable ignition and avoids O_2 leakage, but a very high temperature is unnecessary owing to the limited O_2. 2) Although the increasing driving force boosts coke combustion, too high a force causes an undesired rise in burning temperature. 3) An underground site with large porosity is favourable since it results in a stable combustion front with proper burning temperature and high movement velocity. 4) The heterogeneous coke distribution or matrix structure significantly affects combustion details at the pore scale, but only the random matrix

structure can lead to changes in the medium pore size and then the overall coke combustion intensity. In conclusion, the proposed LB model provides a reliable methodology for simulating coke combustion in porous media at the pore scale. Moreover, improved physical insights into the pore-scale coke combustion are obtained, which have significant implications for heavy oil recovery based on the in-situ combustion process.

CHAPTER 7

Conclusion and future work

7.1 Conclusion

Porous media flows with chemical reaction are frequently encountered in many scientific areas and engineering applications, like geological CO_2 sequestration, oil recovery, and underground water management. In order to explore the underlying mechanisms, such important flows have been studied from two perspectives: the development of LB models and the pore-scale simulations in 2D porous media. The later aspect includes cases of density fingering with homogeneous reaction, viscous fingering with chemical dissolution, and coke combustion in ISC process. Based on these simulations, physical mechanisms at play are investigated, interactions between flow motions and chemical reactions (both homogeneous and heterogeneous) are analysed, and implications to industrial applications are discussed. The main conclusions are as follows.

(1) The development of new MRT LB models for porous media flows at the pore scale.

- An MRT LB model is proposed for simulating porous media flows with homogeneous reaction $A + B \rightarrow C$ between two miscible fluids. In this model, reactive source terms are built to include chemical reactions. Separate LB equations are developed for the concentration equations of the three chemical solutes, with different diffusion rates and density contributions being considered. Furthermore, a buoyancy force term is introduced to incorporate density fingering phenomena.

- To simulate coke combustion during ISC process, another MRT LB model is developed and makes advances on two fronts. First, thermal expansion effects are taken into account via the temperature-dependent air density, satisfying the low Mach number approximation. Second, conjugate heat transfer and species conservation conditions at the air-coke interface are modelled without iterative calculations, by novel source terms and bounce-back schemes, respectively.

- A third MRT LB model is developed to simulate miscible displacement in porous media. This model applies a concentration-dependent viscosity to include the viscous contrast between the displacing and the displaced fluids. The dissolution reaction is described via no-slip and species conservation boundary conditions, which are resolved by bounce-back schemes.

- For the above three MRT LB models, benchmark tests have been carried out to demonstrate their accuracy and reliability in modelling porous media flows with chemical reaction at the pore scale.

(2) Pore-scale simulations of porous media flows with homogeneous reaction.

- The proposed MRT LB model is employed to simulate dissolution-driven density fingering with reaction $A + B \rightarrow C$ in porous media at the pore scale. Results in homogeneous media demonstrate six types of density fingering. The reaction is found to enhance, suppress, or trigger the development of fingering. In addition, the increasing $\Delta \mathrm{Ra}_{CB} = \mathrm{Ra}_C - \mathrm{Ra}_B$ (the relative contribution to fluid density of B and C) is found to intensify fingering, accelerate reaction, and enhance the storage of A. On the other hand, simulations in heterogeneous media also produce six fingering scenarios. Moreover, results show that the random grain distribution introduces

long and rough fingering, the varying porosity along the flow direction affects the fingering propagation velocity, and the large pore size in the top layer brings in long fingering and high storage efficiency of A.

- Using the present MRT LB model, pore-scale studies on density fingering with reaction $A + B \rightarrow C$ are continuously conducted to include differential diffusion effects. Based on a homogeneous porous medium, simulation results demonstrate eight fingering scenarios and four of them are introduced by two differential diffusion mechanisms, i.e., the double-diffusive (DD) and the diffusive-layer convection (DLC) mechanisms. The DD-induced minimum density layer suppresses the fingering propagation but is ultimately penetrated by fingering. The DLC-induced maximum density layer introduces the second fingering area below the first main one. In addition, these two differential diffusion mechanisms have the potential to trigger the development of density fingering. A parametric study suggests that the larger D_B/D_C causes the longer fingering. As the difference between D_B and D_C increases, however, the storage efficiency of A in the host fluid is shown to decrease. Results and insights obtained from these simulations are important to geological CO_2 sequestration.

(3) Pore-scale simulations of porous media flows with heterogeneous reaction.

- Based on the MRT LB model developed, miscible viscous fingering is simulated in a homogeneous medium at the pore scale. The coexistence of viscosity contrast and dissolution reaction is considered. Results capture different fingering patterns that depend on dissolution (Da), diffusion (Pe), and viscosity contrast (R). Dissolution reaction is found to delay the onset of fingering, slow down fingering propagation, inhibit or reinforce the late-stage fingering intensity, and trigger fingering when

dissolution rate is fast enough. In addition, increasing Da suppresses fingering at first but gradually changes to intensify fingering. For every fixed Da, distributions of stable and unstable simulation tests are determined in a Pe-R phase plane. A boundary line between stable and unstable regimes is thus identified. By comparing boundary lines of reactive ($Da > 0$) and non-reactive ($Da = 0$) tests, four distinct regimes are further classified as stable, unstable, reactive stable, and reactive unstable. These findings help to improve the understanding of geological CO_2 sequestration.

- Simulations of pore-scale coke combustion are conducted using the MRT LB model proposed. In a homogeneous medium, results are shown to correctly produce coke combustion dynamics and capture temperature variations from the solid phase to the air phase at the pore scale. Moreover, a parametric analysis suggests that the inlet air temperature and the driving force should be constrained within certain ranges, otherwise their influences may become negligible or even negative. Six types of heterogeneous media are constructed to explore effects of porous structures on coke combustion. Simulation results demonstrate that the large porosity accelerates coke combustion and leads to a favorable combustion front. In addition, random coke distributions affect pore-scale combustion details instead of the overall combustion intensity, while random porous structures influence combustion both locally and globally. These pore-scale results contribute to advancing the knowledge base for heavy oil recovery using ISC process.

7.2 Future work plan

This thesis aims to address the current research limitations in modelling porous media flows with chemical reaction. For this purpose, MRT LB models are developed for simulating porous media flows with both homogeneous and heterogeneous reactions at the pore scale. By using these models, pore-scale simulations are carried out for understanding the physical and chemical mechanisms at play. Results obtained show that the proposed MRT LB models are stable and accurate approaches for studying reactive flows under various conditions in 2D porous media. Moreover, pore-scale findings can enrich the knowledge base and assist the design and optimisation of industrial applications, like geological CO_2 sequestration and enhanced oil recovery. On the other hand, as a first study in the field, this thesis inevitably makes some simplifications, like 2D configurations and miscible fluids. Therefore, further work should be devoted to the following areas:

- The LB models developed use the D2Q9 discrete velocity scheme and focus on reactive flows in 2D porous media. Although simulation results can qualitatively reproduce experimental observations, the quantitative comparison with experiments and the direct modelling of industrial processes require 3D simulations. Thus, the proposed LB models should be extended to 3D, by replacing the discrete velocities, the weight coefficients, and the transformation matrix in Eqs. (2.1)-(2.2) with the 3D counterparts, respectively. For pore-scale simulations, 3D LB codes should be improved to reduce the extremely high demand on the computational resource and storage. A possible solution is to use the adaptive mesh and the sparse storage techniques. In addition, to construct 3D porous media, realistic images and structure

information can be applied to determine distributions of void pores and solid matrices. After these developments, 3D simulations can be performed to quantify flow motions and reaction properties in experiments and engineering applications.

- The current LB models focus on miscible fluid flows in porous media. However, multi-phase flows are involved in diverse experimental and industrial processes. Moreover, multi-phase reactants and products can change the reactive surface and the fluid properties, further affecting the reaction rate, flow motions, and heat and mass transfer. This subsequently hampers efforts to bring the present LB models in line with experiments or industrial applications. To remove this limitation, the present LB models should be continuously developed to model multi-phase fluid flows in porous media. Previous multi-phase LB models, like the pseudopotential and the phase-field models [55], can be applied, with necessary adjustments made.

- In the current study of viscous fingering with chemical dissolution, the displacing and the displaced fluid pairs are assumed to be miscible and isothermal. However, this assumption is inconsistent with some experiments and engineering applications from two aspects. First, chemical reactions are indeed exothermic or endothermic, which modify the local temperature and then affect the reaction rate and the fluid viscosity. Second, two-phase flows are usually involved and thus the capillary force is induced to affect the viscous fingering properties. Besides, to ensure the numerical stability, the tunable viscosity ratio between the two fluids is currently limited to a certain range. To address these issues, a study on immiscible viscous fingering with dissolution reaction can be carried out, where effects of two-phase flows and temperature variations are discussed. In this follow-on work, the viscosity ratio

range can be extended to cover a wider scope of fluid pairs, by applying the lattice kinetic scheme developed by Inamuro *et al.* [165].

- The boundary scheme proposed for the reactive liquid-solid interface can correctly capture the conjugate heat and mass transfer conditions with continuous temperature, concentration, and heat and mass fluxes. Despite that, in scientific and engineering areas, transport phenomena between different phases may show discontinuities (like concentration and temperature jumps) across the phase interface. For such interface jump conditions, a more generalized boundary scheme, including temperature, concentration, and flux jumps, needs to be further formulated. This is expected to be addressed with reference to the second-order accurate boundary treatment for Dirichlet and Neumann problems [166, 167].

- The current simulations of porous media flows with heterogeneous reaction at the fluid-solid interface considers only the dissolution of solid reactants. In parallel, the precipitation reaction is widely encountered in experiments and industrial applications. With chemical solutes precipitating and accumulating on the reactive surface, the available surface area for reaction decreases, which may slow down or even block the reaction. Moreover, the precipitation reaction can gradually modify the porous structure and change the reactive and transport properties. Accordingly, the modelling of porous media flows needs to consider the precipitation reaction. As a reversed process of the chemical dissolution, the precipitation reaction can be easily realized by formulating and solving the reactive boundary conditions.

- The present study on coke combustion, as a first-step work, applies some simplifications, including the one-step reaction, the first-order reaction rate, the fixed thermal

and physical properties of the reactive fluids, and the negligence of the multi-phase reaction products. Therefore, to accurately interpret ISC process, these simplifications need to be removed one-by-one in the future research. This can be achieved after the above model developments.

APPENDIX A

Derivations of heat and mass transfer equations for coke combustion

In this Appendix, derivations of Eqs. (2.37)-(2.38) from Eqs. (2.32)-(2.33) are introduced. As reported in [150], the standard thermal LB method (like the present Eq. (2.42) without F_{q2}) recovers the advection-diffusion equation as,

$$\partial_t \chi + \nabla \cdot (\chi \boldsymbol{u}) = \nabla \cdot (\zeta \nabla \chi) + S, \tag{A.1}$$

where χ is a macroscopic scalar (e.g., temperature T, mass fraction Y, concentration C, etc.), ζ is the corresponding diffusivity coefficient, and S is the source term. For heat transfer problems, the recovered Eq. (A.1) can satisfy conjugate heater transfer conditions at the interface between two phases only when heat capacitances ρc_p are uniform across phases [37, 128]. However, we account for different heat capacitances ρc_p between the solid and air phases, as well as thermal expansion in the air phase, showing that the standard LB method cannot provide a correct solution to resolving conjugate heat transfer conditions. Thus, our target is to build a new LB model for solving the energy conservation equation (2.33), which guarantees the general conjugate heat transfer conditions (without limitations on ρc_p). Similarly, we aim to solve the species conservation equation (2.32) for species transport.

To solve the species and energy conservation equations (2.32)-(2.33), we firstly recast them to fit the from of Eq. (A.1). The energy conservation equation (2.33) is derived as,

$$\partial_t(\rho c_p T) + \nabla\cdot(\rho c_p T\boldsymbol{u}) = \nabla\cdot(\alpha\rho c_p\nabla T) + Q,$$

$$\Rightarrow \rho c_p\partial_t T + T\partial_t(\rho c_p) + \rho c_p\nabla\cdot(T\boldsymbol{u}) + T\boldsymbol{u}\cdot\nabla(\rho c_p) = \rho c_p\nabla\cdot(\alpha\nabla T) + \alpha\nabla T\cdot\nabla(\rho c_p) + Q,$$

$$\Rightarrow \partial_t T + \nabla\cdot(T\boldsymbol{u}) = \nabla\cdot(\alpha\nabla T) + \frac{Q}{\rho c_p} + \left(\frac{\alpha}{\rho c_p}\nabla T\cdot\nabla(\rho c_p) - \frac{T}{\rho c_p}\boldsymbol{u}\cdot\nabla(\rho c_p)\right) - \frac{T}{\rho c_p}\partial_t(\rho c_p). \tag{A.2}$$

The third term on the right hand of Eq. (A.2) is transformed to,

$$\frac{\alpha}{\rho c_p}\nabla T\cdot\nabla(\rho c_p) - \frac{T}{\rho c_p}\boldsymbol{u}\cdot\nabla(\rho c_p) \;\Rightarrow\; \frac{1}{\rho c_p}\nabla(\rho c_p)\cdot(\alpha\nabla T - T\boldsymbol{u}). \tag{A.3}$$

By submitting Eq. (A.3) into Eq. (A.2), one can finally obtain Eq. (2.38) as,

$$\partial_t T + \nabla\cdot(T\boldsymbol{u}) = \nabla\cdot(\alpha\nabla T) + F_T, \tag{A.4}$$

with,

$$F_T = F_{q1} + F_{q2},\;\; F_{q1} = \frac{Q}{\rho c_p},\;\; F_{q2} = \frac{1}{\rho c_p}\nabla(\rho c_p)\cdot(\alpha\nabla T - T\boldsymbol{u}) - \frac{T}{\rho c_p}\partial_t(\rho c_p). \tag{A.5}$$

Such an derivation can be applied for the species conservation equation (2.32) as,

$$\partial_t(\rho Y_n) + \nabla\cdot(\rho Y_n\boldsymbol{u}) = \nabla\cdot(D_n\rho\nabla Y_n),$$

$$\Rightarrow \rho\partial_t Y_n + Y_n\partial_t\rho + \rho\nabla\cdot(Y_n\boldsymbol{u}) + Y_n\boldsymbol{u}\cdot\nabla\rho = \rho\nabla\cdot(D_n\nabla Y_n) + D_n\nabla Y_n\cdot\nabla\rho, \tag{A.6}$$

$$\Rightarrow \partial_t Y_n + \nabla\cdot(Y_n\boldsymbol{u}) = \nabla\cdot(D_n\nabla T) + \frac{D_n}{\rho}\nabla Y_n\cdot\nabla\rho - \frac{Y_n}{\rho}(\partial_t\rho + \boldsymbol{u}\cdot\nabla\rho).$$

Considering species transportation is only solved in pore spaces, the last term on the right hand of Eq. (A.6) is derived as,

$$\frac{Y_n}{\rho}(\partial_t\rho + \boldsymbol{u}\cdot\nabla\rho) \;\Rightarrow\; \frac{Y_n}{\rho}(\partial_t\rho + \nabla\cdot(\rho\boldsymbol{u})) - Y_n\nabla\cdot\boldsymbol{u}. \tag{A.7}$$

Obviously, the first term on the right hand of Eq. (A.7) can be deleted with the help of Eq. (2.30). Thus the above Eq. (A.6) is eventually transformed into Eq. (2.37) as,

$$\partial_t Y_n + \nabla\cdot(Y_n\boldsymbol{u}) = \nabla\cdot(D_n\nabla Y_n) + F_n, \tag{A.8}$$

with,

$$F_n = \frac{D_n}{\rho}\nabla Y_n \cdot \nabla \rho + Y_n \nabla \cdot \boldsymbol{u}. \tag{A.9}$$

Based on these derivations, solving Eqs. (2.32)-(2.33) becomes equivalent to building an LB model for Eqs. (2.37)-(2.38). Compared with the standard LB model for Eq. (A.1), the developed model introduces source terms F_{q2} and F_n to accurately describe conjugate heat transfer and species conservation conditions at the reactive interface.

APPENDIX B

The MRT LB model for miscible viscous fingering with dissolution reaction

In this Appendix, the D2Q9 MRT LB model for pore-scale simulations of miscible viscous fingering with dissolution reaction in porous media is introduced. LB equations for solving the governing equations (2.64)-(2.66) are formulated as [38, 63, 168],

$$\begin{aligned} f_i\left(\boldsymbol{x}+\boldsymbol{e}_i\delta_t,\, t+\delta_t\right)-f_i\left(\boldsymbol{x},\, t\right) =& -\left(\boldsymbol{M}^{-1}\boldsymbol{S}\boldsymbol{M}\right)_{ij}\left[f_j\left(\boldsymbol{x},\, t\right)-f_j^{eq}\left(\boldsymbol{x},\, t\right)\right] \\ &+\delta_t\left(\boldsymbol{M}^{-1}\left(\boldsymbol{I}-0.5\boldsymbol{S}\right)\boldsymbol{M}\right)_{ij}\overline{F}_j, \end{aligned} \tag{B.1}$$

$$g_i\left(\boldsymbol{x}+\boldsymbol{e}_i\delta_t,\, t+\delta_t\right)-g_i\left(\boldsymbol{x},\, t\right) = -\left(\boldsymbol{M}^{-1}\boldsymbol{S}_c\boldsymbol{M}\right)_{ij}\left[g_j\left(\boldsymbol{x},\, t\right)-g_j^{eq}\left(\boldsymbol{x},\, t\right)\right], \tag{B.2}$$

for $i,\ j=0,\ 1,\ ...,\ 8$, where $f_i(\boldsymbol{x},\, t)$ and $g_i(\boldsymbol{x},t)$ are distribution functions for the hydrodynamics and the concentration, respectively. To recover the incompressible equations correctly, the equilibrium distribution functions f_i^{eq} and g_i^{eq} are given as [38],

$$f_i^{eq} = w_i\left[\rho_p+\rho_0\left(\frac{\boldsymbol{e}_i\cdot\boldsymbol{u}}{c_s^2}+\frac{\left(\boldsymbol{e}_i\cdot\boldsymbol{u}\right)^2}{2c_s^4}-\frac{\boldsymbol{u}^2}{2c_s^2}\right)\right], \tag{B.3}$$

$$g_i^{eq} = w_i C_A\left[1+\frac{\boldsymbol{e}_i\cdot\boldsymbol{u}}{c_s^2}+\frac{\left(\boldsymbol{e}_i\cdot\boldsymbol{u}\right)^2}{2c_s^4}-\frac{\boldsymbol{u}^2}{2c_s^2}\right]. \tag{B.4}$$

Here ρ_p is a variable related to the fluid pressure as $p=c_2^2\rho_p$, with $c_s=e/\sqrt{3}$ being the lattice sound velocity. To avoid discrete lattice effects, distribution functions for the driving force $\boldsymbol{F}$ is [38],

$$\overline{F}_i = w_i\left[\frac{\boldsymbol{e}_i\cdot\boldsymbol{F}}{c_s^2}+\frac{\left(\boldsymbol{e}_i\cdot\boldsymbol{u}\right)\left(\boldsymbol{e}_i\cdot\boldsymbol{F}\right)}{c_s^4}-\frac{\boldsymbol{u}\cdot\boldsymbol{F}}{c_s^2}\right]. \tag{B.5}$$

With the transformation equation (2.3), the evolution equations (B.1)-(B.2) are implemented in the moment space as,

$$\hat{\boldsymbol{f}}\left(\boldsymbol{x}+\boldsymbol{e}_i\delta_t,\, t+\delta_t\right)=\hat{\boldsymbol{f}}\left(\boldsymbol{x},\, t\right)-\boldsymbol{S}\left[\hat{\boldsymbol{f}}\left(\boldsymbol{x},\, t\right)-\hat{\boldsymbol{f}}^{eq}\left(\boldsymbol{x},\, t\right)\right]+\delta_t\left(\boldsymbol{I}-\frac{\boldsymbol{S}}{2}\right)\hat{\boldsymbol{F}}, \tag{B.6}$$

$$\hat{\boldsymbol{g}}\left(\boldsymbol{x}+\boldsymbol{e}_i\delta_t,\, t+\delta_t\right)=\hat{\boldsymbol{g}}\left(\boldsymbol{x},\, t\right)-\boldsymbol{S}_c\left[\hat{\boldsymbol{g}}\left(\boldsymbol{x},\, t\right)-\hat{\boldsymbol{g}}^{eq}\left(\boldsymbol{x},\, t\right)\right], \tag{B.7}$$

where $\boldsymbol{S}$ and $\boldsymbol{S}_c$ are the diagonal relaxation matrices of relaxation rates s_i and $s_{c,i}$ in the moment space, respectively. In the following simulations, the relaxation rates are chosen as used in [63]. The equilibrium and forcing moments are expressed as,

$$\hat{\boldsymbol{f}}^{eq}=\left(\rho_p,-2\rho_p+3\rho_0\boldsymbol{u}^2,\rho_p-3\rho_0\boldsymbol{u}^2,\rho_0 u,-\rho_0 u,\rho_0 v,-\rho_0 v,\rho_0\left(u^2-v^2\right),\rho_0 uv\right), \tag{B.8}$$

$$\hat{\boldsymbol{g}}^{eq}=C_A\left(1,-2+3\boldsymbol{u}^2,1-3\boldsymbol{u}^2,u,-u,v,-v,u^2-v^2,uv\right), \tag{B.9}$$

$$\hat{\boldsymbol{F}}=\left(0,6\boldsymbol{u}\cdot\boldsymbol{F},-6\boldsymbol{u}\cdot\boldsymbol{F},F_x,-F_x,F_y,-F_y,2\left(uF_x-vF_y\right),uF_y+vF_x\right). \tag{B.10}$$

Finally, the macroscopic variables can be obtained from the distribution functions as,

$$\rho_p=\sum_i f_i,\quad \rho_0\boldsymbol{u}=\sum_i \boldsymbol{e}_i f_i+0.5\delta_t\boldsymbol{F},\quad C_A=\sum_i g_i. \tag{B.11}$$

Through the Chapman-Enskog analysis on the proposed LB equations, the governing equations can be recovered with the relaxation times τ and τ_A being,

$$\nu=\left(\tau-0.5\right)\delta_t c_s^2,\qquad D_A=\left(\tau_A-0.5\right)\delta_t c_s^2. \tag{B.12}$$

APPENDIX C

Brief description of the LB codes used in this thesis

This appendix provides computational information of the LB codes developed in this thesis. Generally, the LB algorithm consists of five subroutines: initialization, collision, streaming, boundary conditions, and macro variables. For the MRT LB models proposed in Chapter 2, a basic algorithm flowchart is provided in Table C.1. Following such an algorithm structure, current LB models are programmed in the language of C/C++. In order to execute in parallel, the newly-written LB codes apply the Message Passing Interface library. It is emphasized that, during the code writing, subroutines of the flowchart in Table C.1 can be adjusted based on the corresponding LB model. For example, in the LB code for density fingering with homogeneous reaction, the implementation of the reactive fluid-solid interface in step 4(1) is not included.

Based on these self-developed LB codes, pore-scale simulations of porous media flows with chemical reaction are realized on the UK National Supercomputing Service, namely, the ARCHER. Our statistics show that the parallel LB codes can perform efficiently even when high-resolution meshes are selected for describing porous media. First, in Chapters 3-4 of density fingering with homogeneous reaction, a computational domain of mesh size $N_x \times N_y = 1500 \times 1000$ is used. For a simulation case lasting a dimensionless time period $t^* = 100$, a 1.12-hour parallel computation of 240 compute cores can provide information about the fingering development and the chemical reaction. Then, for a simulation test of viscous fingering with chemical dissolution in Chapter 5, a mesh of

size $N_x \times N_y = 1920 \times 954$ is applied and it takes a 0.29-hour parallel computation of 240 compute cores to record fingering dynamics and reaction properties in a dimensionless time period $t^* = 0.1$. Finally, based on a computational domain of size $N_x \times N_y = 1020 \times 760$, a simulation case of coke combustion in Chapter 6 spends 3.27 hours of computational time using 480 compute cores to capture coke combustion dynamics in 1 s physical time.

Table C.1 A typical flowchart for programming the present LB models.

Input: $\mathscr{I}$; **Output:** $\mathscr{O}$

Start Program

1. Read the porous medium structure:
   - Label each node $\boldsymbol{x}$ of the mesh $\mathscr{M}$ as fluid, reactive solid, or non-reactive solid.
2. Set the initial parameters $\mathscr{I}$:
   - LB parameters: $\boldsymbol{e}_i$, $\boldsymbol{S}$, $\boldsymbol{M}$, ...
   - Properties of both fluid and solid phases: $\boldsymbol{u}$, ρ, C_r, T, ...
3. Initialize the distribution functions as the equilibrium values:
   - $\mathscr{F}_i(\boldsymbol{x},\, 0) = \mathscr{F}_i^{eq}(\boldsymbol{x},\, 0) \quad (\mathscr{F} = f,\, g,\, h,\, ...)$
4. Loop for time steps $\mathscr{N}$:
   (1) Impose boundary conditions at the reactive fluid-solid interface:
   - Update the interface concentration C_r^I.
   - Update the interface reaction rate.

   (2) Update LB parameters.

   (3) Calculate the post-collision distribution functions (Collision):
   - $\mathscr{F}_i'(\boldsymbol{x},\, t) = \mathscr{F}_i(\boldsymbol{x},\, t) - \boldsymbol{M}^{-1}\boldsymbol{S}\boldsymbol{M}\left(\mathscr{F}_i(\boldsymbol{x},\, t) - \mathscr{F}_i^{eq}(\boldsymbol{x},\, t)\right)$.

   (4) Propagate particles (Streaming):
   - $\mathscr{F}_i(\boldsymbol{x} + \boldsymbol{e}_i\delta_t,\, t + \delta_t) = \mathscr{F}_i'(\boldsymbol{x},\, t)$.

   (5) Calculating macro properties of both fluid and solid phases at $\mathscr{M}$.

   (6) Impose boundary conditions:
   - The fluid-solid interface and the computational domain boundaries.

   (7) Update the porous medium structure.

   (8) Go back to step (1) and repeat steps (1)-(6) until the stop criterion is satisfied.
5. Obtain macro variables $\mathscr{O}$.

End Program

References

[1] M. Rabiu Ado. *Numerical simulation of heavy oil and bitumen recovery and upgrading techniques*. PhD thesis, University of Nottingham, Nottingham, UK, 2017.

[2] OPEC. World oil outlook 2019. *Organization of the Petroleum Exporting Countries, Vienna, Austria*, 2019.

[3] IEA. World energy 2020. *International Energy Agency, Paris, France*, 2020.

[4] K. Guo, H.L. Li, and Z.X. Yu. In-situ heavy and extra-heavy oil recovery: A review. *Fuel*, 185:886–902, 2016.

[5] A.Y. Huc. *Heavy crude oils: from geology to upgrading: an overview*. Editions Technip, 2010.

[6] V. Alvarado and E. Manrique. Enhanced oil recovery: an update review. *Energies*, 3(9):1529–1575, 2010.

[7] A. Shah, R. Fishwick, J. Wood, G. Leeke, S. Rigby, and M. Greaves. A review of novel techniques for heavy oil and bitumen extraction and upgrading. *Energy & Environmental Science*, 3(6):700–714, 2010.

[8] A.T. Turta and A.K. Singhal. Overview of short-distance oil displacement processes. *Journal of Canadian Petroleum Technology*, 43(2):29–38, 2004.

[9] N. Mahinpey, A. Ambalae, and K. Asghari. In situ combustion in enhanced oil recovery (EOR): A review. *Chemical Engineering Communications*, 194(8):995–1021, 2007.

[10] Q.H. Xu, W. Long, H. Jiang, C. Zan, J. Huang, X. Chen, and L. Shi. Pore-scale modelling of the coupled thermal and reactive flow at the combustion front during crude oil in-situ combustion. *Chemical Engineering Journal*, 350:776–790, 2018.

[11] P.S. Sarathi. In-situ combustion handbook-principles and practices. Technical report, National Petroleum Technology Office, Oklahoma, U.S., 1999.

[12] M. Cinar. *Kinetics of crude-oil combustion in porous media interpreted using isoconversional methods*. Stanford University, 2011.

[13] T.X. Xia, M. Greaves, and A. Turta. Main mechanism for stability of THAI-Toe-to-Heel Air Injection. *Journal of Canadian Petroleum Technology*, 44:42–48, 2005.

[14] R.G. Moore, C.J. Laureshen, S.A. Mehta, and M.G. Ursenbach. Observations and design considerations for in situ combustion projects. *Journal of Canadian Petroleum Technology*, 38(13):97–100, 1999.

[15] J.Z. Liang, W.L. Guan, Y.W. Jiang, C.F. Xi, B.J. Wang, and X.L. Li. Propagation and control of fire front in the combustion assisted gravity drainage using horizontal wells. *Petroleum Exploration and Development*, 39(6):764–772, 2012.

[16] M. Greaves, T.X. Xia, and A.T. Turta. Stability of THAI process-Theoretical and experimental observations. *Journal of Canadian Petroleum Technology*, 47(9):65–73, 2008.

[17] F.M. Orr Jr. CO_2 capture and storage: are we ready? *Energy & Environmental Science*, 2(5):449–458, 2009.

[18] A. Al-Mamoori, A. Krishnamurthy, A.A. Rownaghi, and F. Rezaei. Carbon capture and utilization update. *Energy Technology*, 5(6):834–849, 2017.

[19] N.A. Azzolina, M.J. Small, D.V. Nakles, K.A. Glazewski, W.D. Peck, C.D. Gorecki, G.S. Bromhal, and R.M. Dilmore. Quantifying the benefit of wellbore leakage potential estimates for prioritizing long-term MVA well sampling at a CO_2 storage site. *Environmental Science & Technology*, 49(2):1215–1224, 2015.

[20] R.K. Pachauri, L. Gomez-Echeverri, and K. Riahi. Synthesis report: summary for policy makers. 2014.

[21] Y. Chen, A.J. Valocchi, Q.J. Kang, and H.S. Viswanathan. Inertial effects during the process of supercritical CO_2 displacing brine in a sandstone: Lattice Boltzmann

simulations based on the continuum-surface-force and geometrical wetting models. *Water Resources Research*, 55(12):11144–11165, 2019.

[22] P. Szymczak and A.J.C. Ladd. Reactive-infiltration instabilities in rocks. Part 2. Dissolution of a porous matrix. *Journal of Fluid Mechanics*, 738:591–630, 2014.

[23] P. Shukla and A. De Wit. Fingering dynamics driven by a precipitation reaction: Nonlinear simulations. *Physical Review E*, 93(2):023103, 2016.

[24] P. Ghoshal and S.S.S. Cardoso. Reactive convective-dissolution in a porous medium: stability and nonlinear dynamics. *Physical Chemistry Chemical Physics*, 20(33):21617–21628, 2018.

[25] H. Emami-Meybodi, H. Hassanzadeh, C.P. Green, and J. Ennis-King. Convective dissolution of CO_2 in saline aquifers: Progress in modeling and experiments. *International Journal of Greenhouse Gas Control*, 40:238–266, 2015.

[26] T.J. Ward, K.A. Cliffe, O.E. Jensen, and H. Power. Dissolution-driven porous-medium convection in the presence of chemical reaction. *Journal of Fluid Mechanics*, 747:316–349, 2014.

[27] C. Thomas, S. Dehaeck, and A. De Wit. Convective dissolution of CO_2 in water and salt solutions. *International Journal of Greenhouse Gas Control*, 72:105–116, 2018.

[28] V. Loodts, B. Knaepen, L. Rongy, and A. De Wit. Enhanced steady-state dissolution flux in reactive convective dissolution. *Physical Chemistry Chemical Physics*, 19(28):18565–18579, 2017.

[29] S.A. Abdul Hamid and A.H. Muggeridge. Fingering regimes in unstable miscible displacements. *Physics of Fluids*, 32(1):016601, 2020.

[30] Y.F. Li, G. Blois, F. Kazemifar, and K.T. Christensen. High-speed quantification of pore-scale multiphase flow of water and supercritical CO_2 in 2D heterogeneous porous micromodels: Flow regimes and interface dynamics. *Water Resources Research*, 55(5):3758–3779, 2019.

[31] R.A. Wooding, S.W. Tyler, and I. White. Convection in groundwater below an evaporating salt lake: 1. Onset of instability. *Water Resources Research*, 33(6):1199–1217, 1997.

[32] R.A. Wooding, S.W. Tyler, I. White, and P.A. Anderson. Convection in groundwater below an evaporating salt lake: 2. Evolution of fingers or plumes. *Water Resources Research*, 33(6):1219–1228, 1997.

[33] J.D. Stevens, J.M. Sharp Jr, C.T. Simmons, and T.R. Fenstemaker. Evidence of free convection in groundwater: Field-based measurements beneath wind-tidal flats. *Journal of Hydrology*, 375(3-4):394–409, 2009.

[34] S.S.S. Cardoso and J.T.H. Andres. Geochemistry of silicate-rich rocks can curtail spreading of carbon dioxide in subsurface aquifers. *Nature Communications*, 5(1):1–6, 2014.

[35] L.T. Ritchie and D. Pritchard. Natural convection and the evolution of a reactive porous medium. *Journal of Fluid Mechanics*, 673:286–317, 2011.

[36] L. Rongy, K.B. Haugen, and A. Firoozabadi. Mixing from Fickian diffusion and natural convection in binary non-equilibrium fluid phases. *AIChE Journal*, 58(5):1336–1345, 2012.

[37] Y.L. He, Q. Liu, Q. Li, and W.Q. Tao. Lattice Boltzmann methods for single-phase and solid-liquid phase-change heat transfer in porous media: A review. *International Journal of Heat and Mass Transfer*, 129:160–197, 2019.

[38] Z.L. Guo and C. Shu. *Lattice Boltzmann method and its applications in engineering*. World Scientific Publisher, Singapore, Singapore, 2013.

[39] A. Faghri, Y.W. Zhang, and J.R. Howell. *Advanced heat and mass transfer*. Global Digital Press, Columbia, USA, 2010.

[40] T.M. Lei, K.H. Luo, and D. Wu. Generalized lattice Boltzmann model for frosting. *Physical Review E*, 99(5):053301, 2019.

[41] Z.L. Guo and T.S. Zhao. A lattice Boltzmann model for convection heat transfer in porous media. *Numerical Heat Transfer, Part B*, 47(2):157–177, 2005.

[42] X.M. Wu, Q. Ma, F.Q. Chu, and S. Hu. Phase change mass transfer model for frost growth and densification. *International Journal of Heat and Mass Transfer*, 96:11–19, 2016.

[43] X.M. Wu, F.Q. Chu, and Q. Ma. Frosting model based on phase change driving force. *International Journal of Heat and Mass Transfer*, 110:760–767, 2017.

[44] G.J. Liu and Z.L. Guo. Effects of Prandtl number on mixing process in miscible Rayleigh-Taylor instability. *International Journal of Numerical Methods for Heat & Fluid Flow*, 23(1):176–188, 2013.

[45] Q.J. Kang, D.X. Zhang, S.Y. Chen, and X.Y. He. Lattice Boltzmann simulation of chemical dissolution in porous media. *Physical Review E*, 65(3):036318, 2002.

[46] Q.J. Kang, P.C. Lichtner, H.S. Viswanathan, and A.I. Abdel-Fattah. Pore scale modeling of reactive transport involved in geologic CO_2 sequestration. *Transport in Porous Media*, 82(1):197–213, 2010.

[47] Q.J. Kang, L. Chen, A.J. Valocchi, and H.S. Viswanathan. Pore-scale study of dissolution-induced changes in permeability and porosity of porous media. *Journal of Hydrology*, 517:1049–1055, 2014.

[48] T.M. Lei, X.H. Meng, and Z.L. Guo. Pore-scale study on reactive mixing of miscible solutions with viscous fingering in porous media. *Computers & Fluids*, 155:146–160, 2017.

[49] A. De Wit and G.M. Homsy. Nonlinear interactions of chemical reactions and viscous fingering in porous media. *Physics of Fluids*, 11(5):949–951, 1999.

[50] S.S. Feng, J.J. Kuang, T. Wen, T.J. Lu, and K. Ichimiya. An experimental and numerical study of finned metal foam heat sinks under impinging air jet cooling. *International Journal of Heat and Mass Transfer*, 77:1063–1074, 2014.

[51] S.S. Feng, M. Shi, Y.F. Li, and T.J. Lu. Pore-scale and volume-averaged numerical simulations of melting phase change heat transfer in finned metal foam. *International Journal of Heat and Mass Transfer*, 90:838–847, 2015.

[52] S.S. Feng, Y. Zhang, M. Shi, T. Wen, and T.J. Lu. Unidirectional freezing of phase change materials saturated in open-cell metal foams. *Applied Thermal Engineering*, 88:315–321, 2015.

[53] M. Sheikholeslami. Finite element method for PCM solidification in existence of CuO nanoparticles. *Journal of Molecular Liquids*, 265:347–355, 2018.

[54] M. Sheikholeslami. Numerical modeling of nano enhanced PCM solidification in an enclosure with metallic fin. *Journal of Molecular Liquids*, 259:424–438, 2018.

[55] Q. Li, K.H. Luo, Q.J. Kang, Y.L. He, Q. Chen, and Q. Liu. Lattice Boltzmann methods for multiphase flow and phase-change heat transfer. *Progress in Energy and Combustion Science*, 52:62–105, 2016.

[56] Z.L. Guo and T.S. Zhao. Lattice Boltzmann model for incompressible flows through porous media. *Physical Review E*, 66(3):036304, 2002.

[57] D.Y. Gao and Z.Q. Chen. Lattice Boltzmann simulation of natural convection dominated melting in a rectangular cavity filled with porous media. *International Journal of Thermal Sciences*, 50(4):493–501, 2011.

[58] D.Y. Gao, Z.Q. Chen, D.L. Zhang, and L.H. Chen. Lattice Boltzmann modeling of melting of phase change materials in porous media with conducting fins. *Applied Thermal Engineering*, 118:315–327, 2017.

[59] Q. Liu, Y.L. He, Q. Li, and W.Q. Tao. A multiple-relaxation-time lattice Boltzmann model for convection heat transfer in porous media. *International Journal of Heat and Mass transfer*, 73:761–775, 2014.

[60] Q. Liu and Y.L. He. Double multiple-relaxation-time lattice Boltzmann model for solid-liquid phase change with natural convection in porous media. *Physica A: Statistical Mechanics and its Applications*, 438:94–106, 2015.

[61] W. Wu, S.L. Zhang, and S.F. Wang. A novel lattice Boltzmann model for the solid-liquid phase change with the convection heat transfer in the porous media. *International Journal of Heat and Mass Transfer*, 104:675–687, 2017.

[62] C.X. Pan, L.S. Luo, and C.T. Miller. An evaluation of lattice Boltzmann schemes for porous medium flow simulation. *Computers & Fluids*, 35(8-9):898–909, 2006.

[63] T.M. Lei and K.H. Luo. Pore-scale study of dissolution-driven density instability with reaction $A + B \rightarrow C$ in porous media. *Physical Review Fluids*, 4(6):063907, 2019.

[64] T.M. Lei and K.H. Luo. Differential diffusion effects on density-driven instability of reactive flows in porous media. *Physical Review Fluids*, 5(3):033903, 2020.

[65] A.G. O'Donnell, I.M. Young, S.P. Rushton, M.D. Shirley, and J.W. Crawford. Visualization, modelling and prediction in soil microbiology. *Nature Reviews Microbiology*, 5(9):689–699, 2007.

[66] G.J. Liu and Z.L. Guo. Pore-scale study of the non-linear mixing of fluids with viscous fingering in anisotropic porous media. *Communications in Computational Physics*, 17(4):1019–1036, 2015.

[67] Q.H. Xu, W. Long, H. Jiang, B. Ma, C. Zan, D.S. Ma, and L. Shi. Quantification of the microstructure, effective hydraulic radius and effective transport properties changed by the coke deposition during the crude oil in-situ combustion. *Chemical Engineering Journal*, 331:856–869, 2018.

[68] H. Emami-Meybodi. Stability analysis of dissolution-driven convection in porous media. *Physics of Fluids*, 29(1):014102, 2017.

[69] K. Ghesmat, H. Hassanzadeh, and J. Abedi. The impact of geochemistry on convective mixing in a gravitationally unstable diffusive boundary layer in porous media: CO_2 storage in saline aquifers. *Journal of Fluid Mechanics*, 673:480–512, 2011.

[70] M.A. Budroni, L.A. Riolfo, L. Lemaigre, F. Rossi, M. Rustici, and A. De Wit. Chemical control of hydrodynamic instabilities in partially miscible two-layer systems. *The Journal of Physical Chemistry Letters*, 5(5):875–881, 2014.

[71] C. Wylock, A. Rednikov, B. Haut, and P. Colinet. Nonmonotonic Rayleigh-Taylor instabilities driven by gas-liquid CO_2 chemisorption. *The Journal of Physical Chemistry B*, 118(38):11323–11329, 2014.

[72] C. Wylock, A. Rednikov, P. Colinet, and B. Haut. Experimental and numerical analysis of buoyancy-induced instability during CO_2 absorption in $NaHCO_3$-Na_2CO_3 aqueous solutions. *Chemical Engineering Science*, 157:232–246, 2017.

[73] C. Thomas, V. Loodts, L. Rongy, and A. De Wit. Convective dissolution of CO_2 in reactive alkaline solutions: Active role of spectator ions. *International Journal of Greenhouse Gas Control*, 53:230–242, 2016.

[74] I. Cherezov and S.S.S. Cardoso. Acceleration of convective dissolution by chemical reaction in a Hele-Shaw cell. *Physical Chemistry Chemical Physics*, 18(34):23727–23736, 2016.

[75] M.A. Budroni, C. Thomas, and A. De Wit. Chemical control of dissolution-driven convection in partially miscible systems: nonlinear simulations and experiments. *Physical Chemistry Chemical Physics*, 19(11):7936–7946, 2017.

[76] C. Thomas, L. Lemaigre, A. Zalts, A. D'Onofrio, and A. De Wit. Experimental study of CO_2 convective dissolution: the effect of color indicators. *International Journal of Greenhouse Gas Control*, 42:525–533, 2015.

[77] M.C. Kim. Effect of the irreversible $A + B \rightarrow C$ reaction on the onset and the growth of the buoyancy-driven instability in a porous medium. *Chemical Engineering Science*, 112:56–71, 2014.

[78] M.C. Kim and C. Wylock. Linear and nonlinear analyses of the effect of chemical reaction on the onset of buoyancy-driven instability in a CO_2 absorption process in a porous medium or Hele-Shaw cell. *The Canadian Journal of Chemical Engineering*, 95(3):589–604, 2017.

[79] M.C. Kim. Effect of the irreversible $A + B \rightarrow C$ reaction on the onset and the growth of the buoyancy-driven instability in a porous medium: Asymptotic, linear, and nonlinear stability analyses. *Physical Review Fluids*, 4(7):073901, 2019.

[80] V. Loodts, C. Thomas, L. Rongy, and A. De Wit. Control of convective dissolution by chemical reactions: General classification and application to CO_2 dissolution in reactive aqueous solutions. *Physical Review Letters*, 113(11):114501, 2014.

[81] V. Loodts, L. Rongy, and A. De Wit. Chemical control of dissolution-driven convection in partially miscible systems: theoretical classification. *Physical Chemistry Chemical Physics*, 17(44):29814–29823, 2015.

[82] V. Loodts, P.M.J. Trevelyan, L. Rongy, and A. De Wit. Density profiles around $A + B \rightarrow C$ reaction-diffusion fronts in partially miscible systems: A general classification. *Physical Review E*, 94(4):043115, 2016.

[83] M. Jotkar, A. De Wit, and L. Rongy. Enhanced convective dissolution due to an $A + B \rightarrow C$ reaction: control of the non-linear dynamics via solutal density contributions. *Physical Chemistry Chemical Physics*, 21(12):6432–6442, 2019.

[84] V. Loodts, H. Saghou, B. Knaepen, L. Rongy, and A. De Wit. Differential diffusivity effects in reactive convective dissolution. *Fluids*, 3(4):83, 2018.

[85] P.M.J. Trevelyan, C. Almarcha, and A. De Wit. Buoyancy-driven instabilities of miscible two-layer stratifications in porous media and Hele-Shaw cells. *Journal of Fluid Mechanics*, 670:38–65, 2011.

[86] J. Carballido-Landeira, P.M.J. Trevelyan, C. Almarcha, and A. De Wit. Mixed-mode instability of a miscible interface due to coupling between Rayleigh-Taylor and double-diffusive convective modes. *Physics of Fluids*, 25(2):024107, 2013.

[87] P.M.J. Trevelyan, C. Almarcha, and A. De Wit. Buoyancy-driven instabilities around miscible $A + B \rightarrow C$ reaction fronts: A general classification. *Physical Review E*, 91(2):023001, 2015.

[88] M. Jotkar, L. Rongy, and A. De Wit. Reactive convective dissolution with differential diffusivities: Nonlinear simulations of onset times and asymptotic fluxes. *Physical Review Fluids*, 5(10):104502, 2020.

[89] M.C. Kim and S.S.S. Cardoso. Diffusivity ratio effect on the onset of the buoyancy-driven instability of an $A + B \rightarrow C$ chemical reaction system in a Hele-Shaw cell: Numerical simulations and comparison with experiments. *Physics of Fluids*, 31(8):084101, 2019.

[90] M.C. Kim and S.S.S. Cardoso. Diffusivity ratio effect on the onset of the buoyancy-driven instability of an $A + B \rightarrow C$ chemical reaction system in a Hele-Shaw cell: Asymptotic and linear stability analyses. *Physics of Fluids*, 30(9):094102, 2018.

[91] P. Cheng, M. Bestehorn, and A. Firoozabadi. Effect of permeability anisotropy on buoyancy-driven flow for CO_2 sequestration in saline aquifers. *Water Resources Research*, 48(9):W09539, 2012.

[92] A. De Wit. Chemo-hydrodynamic patterns and instabilities. *Annual Review of Fluid Mechanics*, 52:531–555, 2020.

[93] G.M. Homsy. Viscous fingering in porous media. *Annual Review of Fluid Mechanics*, 19(1):271–311, 1987.

[94] P.G. Saffman and G.I. Taylor. The penetration of a fluid into a porous medium or Hele-Shaw cell containing a more viscous liquid. *Proceedings of the Royal Society of London. Series A. Mathematical and Physical Sciences*, 245(1242):312–329, 1958.

[95] B. Jha, L. Cueto-Felgueroso, and R. Juanes. Fluid mixing from viscous fingering. *Physical Review Letters*, 106(19):194502, 2011.

[96] S. Sarkar, S. Ganguly, and M. Mishra. Single diffusive magnetohydrodynamic pressure driven miscible displacement flows in a channel. *Physics of Fluids*, 31(8):082102, 2019.

[97] B. Dastvareh and J. Azaiez. Instabilities of nanofluid flow displacements in porous media. *Physics of Fluids*, 29(4):044101, 2017.

[98] A. De Wit and G.M. Homsy. Viscous fingering in periodically heterogeneous porous media. I. Formulation and linear instability. *The Journal of Chemical Physics*, 107(22):9609–9618, 1997.

[99] A. De Wit and G.M. Homsy. Viscous fingering in periodically heterogeneous porous media. II. Numerical simulations. *The Journal of Chemical Physics*, 107(22):9619–9628, 1997.

[100] M.R. Shahnazari, I. Maleka Ashtiani, and A. Saberi. Linear stability analysis and nonlinear simulation of the channeling effect on viscous fingering instability in miscible displacement. *Physics of Fluids*, 30(3):034106, 2018.

[101] Y. Nagatsu and A. De Wit. Viscous fingering of a miscible reactive $A + B \rightarrow C$ interface for an infinitely fast chemical reaction: Nonlinear simulations. *Physics of Fluids*, 23(4):043103, 2011.

[102] C. Rana and M. Mishra. Interaction between shock layer and viscous fingering in a Langmuir adsorbed solute. *Physics of Fluids*, 29(3):032108, 2017.

[103] M. Mishra, M. Martin, and A. De Wit. Influence of miscible viscous fingering of finite slices on an adsorbed solute dynamics. *Physics of Fluids*, 21(8):083101, 2009.

[104] V. Sharma, S. Pramanik, C.Y. Chen, and M. Mishra. A numerical study on reaction-induced radial fingering instability. *Journal of Fluid Mechanics*, 826:624–638, 2019.

[105] V. Sharma, S. Nand, S. Pramanik, C.Y. Chen, and M. Mishra. Control of radial miscible viscous fingering. *Journal of Fluid Mechanics*, 884:A16, 2020.

[106] P. Szymczak and A.J.C. Ladd. Reactive-infiltration instabilities in rocks. Fracture dissolution. *Journal of Fluid Mechanics*, 702:239–264, 2012.

[107] C.N. Fredd and H.S. Fogler. Influence of transport and reaction on wormhole formation in porous media. *AIChE Journal*, 44(9):1933–1949, 1998.

[108] H.P. Menke, B. Bijeljic, and M.J. Blunt. Dynamic reservoir-condition microtomography of reactive transport in complex carbonates: Effect of initial pore structure and initial brine pH. *Geochimica et Cosmochimica Acta*, 204:267–285, 2017.

[109] Y. Hao, M.M. Smith, and S.A. Carroll. Multiscale modeling of CO_2-induced carbonate dissolution: From core to meter scale. *International Journal of Greenhouse Gas Control*, 88:272–289, 2019.

[110] F. Golfier, C. Zarcone, B. Bazin, R. Lenormand, D. Lasseux, and M. Quintard. On the ability of a Darcy-scale model to capture wormhole formation during the dissolution of a porous medium. *Journal of Fluid Mechanics*, 457:213–254, 2002.

[111] M.K.R. Panga, M. Ziauddin, and V. Balakotaiah. Two-scale continuum model for simulation of wormholes in carbonate acidization. *AIChE Journal*, 51(12):3231–3248, 2005.

[112] L. Chen, Q.J. Kang, B. Carey, and W.Q. Tao. Pore-scale study of diffusion-reaction processes involving dissolution and precipitation using the lattice Boltzmann method. *International Journal of Heat and Mass Transfer*, 75:483–496, 2014.

[113] M.L. Hoefner and H.S. Fogler. Pore evolution and channel formation during flow and reaction in porous media. *AIChE Journal*, 34(1):45–54, 1988.

[114] S. Bekri, J.F. Thovert, and P.M. Adler. Dissolution of porous media. *Chemical Engineering Science*, 50(17):2765–2791, 1995.

[115] S. Bekri, J.F. Thovert, and P.M. Adler. Dissolution and deposition in fractures. *Engineering Geology*, 48(3-4):283–308, 1997.

[116] M. Zargartalebi and J. Azaiez. Mesoscopic study of miscible nanoflow instabilities. *Physics of Fluids*, 30(2):024105, 2018.

[117] Q.J. Kang, D.X. Zhang, and S.Y. Chen. Simulation of dissolution and precipitation in porous media. *Journal of Geophysical Research: Solid Earth*, 108(B10):2505, 2003.

[118] Q.J. Kang, P.C. Lichtner, and D.X. Zhang. Lattice Boltzmann pore-scale model for multicomponent reactive transport in porous media. *Journal of Geophysical Research: Solid Earth*, 111(B5):B05203, 2006.

[119] L. Chen, Q.J. Kang, H.S. Viswanathan, and W.Q. Tao. Pore-scale study of dissolution-induced changes in hydrologic properties of rocks with binary minerals. *Water Resources Research*, 50(12):9343–9365, 2014.

[120] Z.Y. Zhu. *Efficient simulation of thermal enhanced oil recovery processes*. PhD thesis, Stanford University, Stanford, California, USA, 2011.

[121] A.A. Mailybaev, J. Bruining, and D. Marchesin. Analysis of in situ combustion of oil with pyrolysis and vaporization. *Combustion and Flame*, 158(6):1097–1108, 2011.

[122] D. Srinivasareddy and G.S. Kumar. A numerical study on phase behavior effects in enhanced oil recovery by in situ combustion. *Petroleum Science and Technology*, 33(3):353–362, 2015.

[123] H. Zheng, W.P. Shi, D.L. Ding, and C.Y. Zhang. Numerical simulation of in situ combustion of oil shale. *Geofluids*, 2017, 2017.

[124] T. Zhang, B.C. Shi, Z.L. Guo, Z.H. Chai, and J.H. Lu. General bounce-back scheme for concentration boundary condition in the lattice-Boltzmann method. *Physical Review E*, 85(1):016701, 2012.

[125] X.H. Meng and Z.L. Guo. Boundary scheme for linear heterogeneous surface reactions in the lattice Boltzmann method. *Physical Review E*, 94(5):053307, 2016.

[126] J.K. Wang, M.R. Wang, and Z.X. Li. A lattice boltzmann algorithm for fluid-solid conjugate heat transfer. *International Journal of Thermal Sciences*, 46(3):228–234, 2007.

[127] M.R. Wang and N. Pan. Modeling and prediction of the effective thermal conductivity of random open-cell porous foams. *International Journal of Heat and Mass Transfer*, 51(5-6):1325–1331, 2008.

[128] H. Karani and C. Huber. Lattice Boltzmann formulation for conjugate heat transfer in heterogeneous media. *Physical Review E*, 91(2):023304, 2015.

[129] L.M. Zhang, C.D. Zhang, K. Zhang, L. Zhang, J. Yao, H. Sun, and Y.F. Yang. Pore-Scale investigation of methane hydrate dissociation using the lattice Boltzmann method. *Water Resources Research*, 55(11):8422–8444, 2019.

[130] K. Yamamoto, X.Y. He, and G.D. Doolen. Simulation of combustion field with lattice Boltzmann method. *Journal of Statistical Physics*, 107(1-2):367–383, 2002.

[131] K. Yamamoto, N. Takada, and M. Misawa. Combustion simulation with Lattice Boltzmann method in a three-dimensional porous structure. *Proceedings of the Combustion Institute*, 30(1):1509–1515, 2005.

[132] Y.Z. Liu, J. Xia, K.D. Wan, L. Vervisch, Z.H. Wang, H. Zhao, and K.F. Cen. Simulation of char-pellet combustion and sodium release inside porous char using lattice Boltzmann method. *Combustion and Flame*, 211:325–336, 2020.

[133] C.D. Lin, K.H. Luo, L.L. Fei, and S. Succi. A multi-component discrete Boltzmann model for nonequilibrium reactive flows. *Scientific Reports*, 7(1):1–12, 2017.

[134] C.D. Lin and K.H. Luo. Mesoscopic simulation of nonequilibrium detonation with discrete Boltzmann method. *Combustion and Flame*, 198:356–362, 2018.

[135] O. Filippova and D. Hänel. Lattice-BGK model for low Mach number combustion. *International Journal of Modern Physics C*, 9(8):1439–1445, 1998.

[136] O. Filippova and D. Hänel. A novel lattice BGK approach for low Mach number combustion. *Journal of Computational Physics*, 158(2):139–160, 2000.

[137] Q. Li, K.H. Luo, Y.L. He, Y.J. Gao, and W.Q. Tao. Coupling lattice boltzmann model for simulation of thermal flows on standard lattices. *Physical Review E*, 85(1):016710, 2012.

[138] Y.L. Feng, P. Sagaut, and W.Q. Tao. A three dimensional lattice model for thermal compressible flow on standard lattices. *Journal of Computational Physics*, 303:514–529, 2015.

[139] S.A. Hosseini, H. Safari, N. Darabiha, D. Thévenin, and M. Krafczyk. Hybrid Lattice Boltzmann-finite difference model for low Mach number combustion simulation. *Combustion and Flame*, 209:394–404, 2019.

[140] Y.L. Feng, M. Tayyab, and P. Boivin. A Lattice-Boltzmann model for low-Mach reactive flows. *Combustion and Flame*, 196:249–254, 2018.

[141] U. Frisch, B. Hasslacher, and Y. Pomeau. Lattice-gas automata for the Navier-Stokes equation. *Physical Review Letters*, 56(14):1505–1508, 1986.

[142] X.Y. He and L.S. Luo. Theory of the lattice Boltzmann method: From the Boltzmann equation to the lattice Boltzmann equation. *Physical Review E*, 56(6):6811–6817, 1997.

[143] X.Y. He and L.S. Luo. A priori derivation of the lattice Boltzmann equation. *Physical Review E*, 55(6):R6333, 1997.

[144] K.N. Premnath and J. Abraham. Three-dimensional multi-relaxation time (MRT) lattice-Boltzmann models for multiphase flow. *Journal of Computational Physics*, 224(2):539–559, 2007.

[145] S.Y. Chen, H.D. Chen, D. Martnez, and W. Matthaeus. Lattice Boltzmann model for simulation of magnetohydrodynamics. *Physical Review Letters*, 67(27):3776–3779, 1991.

[146] N. Rakotomalala, D. Salin, and P. Watzky. Miscible displacement between two parallel plates: BGK lattice gas simulations. *Journal of Fluid Mechanics*, 338:277–297, 1997.

[147] D. d'Humieres. Multiple-relaxation-time lattice Boltzmann models in three dimensions. *Philosophical Transactions of the Royal Society of London. Series A: Mathematical, Physical and Engineering Sciences*, 360(1792):437–451, 2002.

[148] Z.L. Guo and C.G. Zheng. Analysis of lattice Boltzmann equation for microscale gas flows: relaxation times, boundary conditions and the Knudsen layer. *International Journal of Computational Fluid Dynamics*, 22(7):465–473, 2008.

[149] P. Lallemand and L.S. Luo. Theory of the lattice Boltzmann method: Dispersion, dissipation, isotropy, Galilean invariance, and stability. *Physical Review E*, 61(6):6546–6562, 2000.

[150] B.C. Shi and Z.L. Guo. Lattice Boltzmann model for nonlinear convection-diffusion equations. *Physical Review E*, 79(1):016701, 2009.

[151] X.H. Meng and Z.L. Guo. Multiple-relaxation-time lattice Boltzmann model for incompressible miscible flow with large viscosity ratio and high Péclet number. *Physical Review E*, 92(4):043305, 2015.

[152] G. Tryggvason. Numerical simulations of the Rayleigh-Taylor instability. *Journal of Computational Physics*, 75(2):253–282, 1988.

[153] B.C. Shi, B. Deng, R. Du, and X.W. Chen. A new scheme for source term in LBGK model for convection-diffusion equation. *Computers & Mathematics with Applications*, 55(7):1568–1575, 2008.

[154] Z.L. Guo, C.G. Zheng, and B.C. Shi. Non-equilibrium extrapolation method for velocity and pressure boundary conditions in the lattice Boltzmann method. *Chinese Physics*, 11(4):366–374, 2002.

[155] Z.L. Guo, C.G. Zheng, and B.C. Shi. Force imbalance in lattice Boltzmann equation for two-phase flows. *Physical Review E*, 83(3):036707, 2011.

[156] H.H. Liu, Y.H. Zhang, and A.J. Valocchi. Lattice Boltzmann simulation of immiscible fluid displacement in porous media: Homogeneous versus heterogeneous pore network. *Physics of Fluids*, 27(5):052103, 2015.

[157] C. Chen and D.X. Zhang. Pore-scale simulation of density-driven convection in fractured porous media during geological CO_2 sequestration. *Water Resources Research*, 46(11):W11527, 2010.

[158] A.J.C. Ladd. Numerical simulations of particulate suspensions via a discretized Boltzmann equation. Part 1. Theoretical foundation. *Journal of Fluid Mechanics*, 271:285–309, 1994.

[159] A.J.C. Ladd. Numerical simulations of particulate suspensions via a discretized Boltzmann equation. Part 2. Numerical results. *Journal of Fluid Mechanics*, 271:311–339, 1994.

[160] A.M. Tartakovsky and S.P. Neuman. Effects of Peclet number on pore-scale mixing and channeling of a tracer and on directional advective porosity. *Geophysical Research Letters*, 35(21):L21401, 2008.

[161] A.M. Tartakovsky, G.D. Tartakovsky, and T.D. Scheibe. Effects of incomplete mixing on multicomponent reactive transport. *Advances in Water Resources*, 32(11):1674–1679, 2009.

[162] P. Ghoshal, M.C. Kim, and S.S.S. Cardoso. Reactive-convective dissolution in a porous medium: the storage of carbon dioxide in saline aquifers. *Physical Chemistry Chemical Physics*, 19(1):644–655, 2017.

[163] J.J. Hidalgo, J. Fe, L. Cueto-Felgueroso, and R. Juanes. Scaling of convective mixing in porous media. *Physical Review Letters*, 109(26):264503, 2012.

[164] R. Hurt, J.K. Sun, and M. Lunden. A kinetic model of carbon burnout in pulverized coal combustion. *Combustion and Flame*, 113(1-2):181–197, 1998.

[165] T. Inamuro. A lattice kinetic scheme for incompressible viscous flows with heat transfer. *Philosophical Transactions of the Royal Society of London. Series A: Mathematical, Physical and Engineering Sciences*, 360(1792):477–484, 2002.

[166] K. Guo, L. Li, G. Xiao, N. AuYeung, and R. Mei. Lattice Boltzmann method for conjugate heat and mass transfer with interfacial jump conditions. *International Journal of Heat and Mass Transfer*, 88:306–322, 2015.

[167] L. Li, C. Chen, R. Mei, and J.F. Klausner. Conjugate heat and mass transfer in the lattice Boltzmann equation method. *Physical Review E*, 89(4):043308, 2014.

[168] T.M. Lei, Z. Wang, and K.H. Luo. Study of pore-scale coke combustion in porous media using lattice Boltzmann method. *Combustion and Flame*, 225:104–119, 2021.

List of Publications

• Journal papers

1. **T.M. Lei**, Z. Wang, K.H. Luo. Study of pore-scale coke combustion in porous media using lattice Boltzmann method. *Combustion and Flame*, 225:104-119, 2021.

2. **T.M. Lei**, K.H. Luo. Pore-scale simulation of miscible viscous fingering with dissolution reaction in porous media. *Physics of Fluids*, 33(3):034134, 2021.

3. **T.M. Lei**, K.H. Luo. Differential diffusion effects on density-driven instability of reactive flows in porous media. *Physical Review Fluids*, 5(3):033903, 2020.

4. **T.M. Lei**, K.H. Luo. Pore-scale study of dissolution-driven density instability with reaction $A + B \rightarrow C$ in porous media. *Physical Review Fluids*, 4(6):063907, 2019.

5. **T.M. Lei**, K.H. Luo, D. Wu. Generalized lattice Boltzmann model for frosting. *Physical Review E*, 99(5):053301, 2019.

• Conferences

1. **T.M. Lei**, K.H. Luo. Differential diffusion effects on dissolution-driven density instability of reactive flows in porous media. 16th International Conference for Mesoscopic Methods in Engineering and Science, Edinburgh, UK, July 22-26, 2019.